Design of a Hybrid Spherical Manipulator for Lower Limb Exoskeleton Applications

by

Soheil Sadeqi

M.A.Sc., Simon Fraser University, 2013
B.Sc., University of Tehran, 2011

Thesis Submitted in Partial Fulfillment of the
Requirements for the Degree of
Doctor of Philosophy

in the
School of Mechatronic Systems Engineering
Faculty of Applied Sciences

SIMON FRASER UNIVERSITY

Spring 2017

Approval

Name: **Soheil Sadeqi**

Degree: **Doctor of Philosophy**

Title: ***Design of a Hybrid Spherical Manipulator for Lower Limb Exoskeleton Applications***

Examining Committee:

Chair: Mehrdad Moallem
Professor

Siamak Arzanpour
Senior Supervisor
Associate Professor

Edward Jung Wook Park
Senior Supervisor
Professor

Flavio Firmani
Supervisor
Lecturer

Kevin Oldknow
Internal Examiner
Lecturer
School of Mechatronic Systems
Engineering

Clément Gosselin
External Examiner
Professor
Department of Mechanical Engineering
Laval University

Date Defended/Approved: March 6th ,2017

Abstract

An estimated (7.1%) of North American residents suffered from an ambulatory disability and mobility disablements in 2013. These disabilities cost an estimated annual equivalent of $375 billion in family caregiver support. One emergent technology that aims to address this health problem and improve the quality of life for sufferers is a lower-body exoskeleton which is a wearable robotic system that completely or partially supports users weight and provide controlled guidance of legs movements, thereby allowing them to stand and walk.

One major shortcoming of current exoskeleton technologies is their limited range of motion about the hip joint. Such joints are capable of three rotational degrees-of-freedom (DOFs). Current technologies only provide a single DOF hip-centered movements. The other two DOFs are either fully constrained or only available with passive motion. This design scheme generally results in a serial joint structure within the exoskeleton device, which has an inherently lower payload-to-weight ratio than a parallel structure counterpart. Therefore, this characteristic leads to bulkier than necessary devices.

The objective of this thesis is studying the feasibility and later on design compact three DOF robotic joints to replace the single DOF of the hip actuator of the commercially available exoskeletons. In this thesis a three degree-of-freedom (DOF) hip exoskeleton system that is capable of providing decoupled or combined 3-DOF rotational motion to a separate and passive target joint (i.e. the hip joint) is proposed.

Keywords: Lower limb exoskeleton; parallel manipulator; spherical parallel manipulator; hybrid manipulator; human locomotion; mobility assistive device

In dedication to my parents for making me who I am
and my wife, Dordaneh, for supporting me all the way.

Acknowledgements

Firstly, I would like to express my sincere gratitude to my senior supervisor, Dr. Siamak Arzanpour for the continuous support of my Ph.D study and related research, for his patience, motivation, and immense knowledge. His guidance helped me in all the time of research. I could not have imagined having a better advisor and mentor for my Ph.D study.

I would like to thank the rest of my thesis committee: Dr. Edward Park and Dr. Flavio Firmani for their encouragement and for generously giving their time and expertise to better my work. I thank them for their contribution and their good-natured support. I would also like to thank Dr. Kevin Oldknow and Dr. Clément Gosselin for dedicating their precious time reading this thesis and for their insightful comments.

I like to express my gratitude and appreciation to my fellow lab mate and dear friend Shaun Bourgeois for the stimulating discussions, for the sleepless nights we were working together before deadlines, for sharing his wisdom and knowledge and for all the fun we have had during this research. I would also like to thank my dear friends, Mehran Ahmadi, Maryam Yazdanpour, Hossein Dehghani, Arash Tavassoli, Negar Khalesi Kambiz Hajikolahi and Fattaneh Nadimi for their unforgettable memories.

I have received financial support from Natural Sciences and Engineering Research Council (NSERC) of Canada and Simon Fraser University, for which I am grateful.

I send my deepest gratitude to my father and mother; the absolute source of love and support, who have always had the most faith in me, even when I had the least.

And finally to my wife Dordaneh, who has been by my side throughout this Ph.D study, living every single minute of it, and without whom, I would not have had the bravery to embark on this journey in the first place. I express my highest appreciation for her love and support during this challenging journey.

Table of Contents

List of Tables

List of Figures

List of Acronyms

Abd./Add.	Abduction and adduction motion of hip joint
CAD	Computer aided design
CGA	Clinical gait analysis
DH	Denavit-Hartenberg
DOF	Degree-of-freedom
Flex./Extn.	Flexion and extension motion of hip joint
HMI	Human machine interface
IMU	Inertial measurement unit
Int./Ext. Rot.	Internal and external rotation of hip joint
GPI	Global performance index

Symbols

${}^{B}a_x$	x-coordinate of generalized vector **a** with respect to generalized frame B	mm
${}^{B}a_y$	y-coordinate of generalized vector **a** with respect to generalized frame B	mm
${}^{B}a_z$	z-coordinate of generalized vector **a** with respect to generalized frame B	mm
${}^{B}\mathbf{x}_a$	unit vector associated with the x-axis of generalized vector **a** and/or frame A, represented in terms of generalized frame B	mm
${}^{B}\mathbf{y}_a$	unit vector associated with the y-axis of generalized vector **a** and/or frame A, represented in terms of generalized frame B	mm
${}^{B}\mathbf{z}_a$	unit vector associated with the z-axis of generalized vector **a** and/or frame A, represented in terms of generalized frame B	mm
d_1	distance between point **s** and the axis of action of the passive rotary joint associated with $\mathbf{o}_2$	mm
d_2	euclidean distance between points $\mathbf{o}_1$ and $\mathbf{o}_2$	mm
d_3	distance between the projection of point **f** in the x_s-z_s plane and $\mathbf{o}_1$	mm
d_i	scalar measure of the i^{th} limb	mm
f	vector identifying the rotational centre of the target ball-and-socket joint	mm
F_i	cartesian frame number i	
g	gravitational acceleration	m/s^2
h	spherical joint local height	mm
I_i	moment of inertia of the i^{th} limb	$kg.m/s^2$
${}^{i}\mathbf{P}_n^{*}$	position vector of the n^{th} center of mass with respect to the i^{th} frame	mm
J	jacobian matrix	
$^{j}\boldsymbol{a_i}$	vector defining i^{th} limb's rotary joint as represented in the j^{th} frame	mm
$^{j}\boldsymbol{b_i}$	vector defining i^{th} limb's universal joint as represented in the j^{th} frame	mm
$^{j}\boldsymbol{c_i}$	vector defining i^{th} limb's spherical joint as represented in the j^{th} frame	mm
k	condition number	
K	kinetic energy	j
L	lagrange function	j
l_1	distance between the projections of points **f** and $\mathbf{o}_1$ in the x_f-y_f plane	mm
l_{1i}	length of the i^{th} limb's distal link	mm
l_2	distance between the projections of points $\mathbf{o}_1$ and $\mathbf{o}_2$ in the x_f-y_f plane	mm
l_{2i}	length of the i^{th} limb's proximal link	mm

l_3	distance between the projections of points $\mathbf{o}_2$ and $\mathbf{s}$ in the x_f-y_f plane	mm
M	Manipulator inertia matrix	
$\mathbf{o}_1$	3D vector identifying the position of the passive rotary joint attached to the passive prismatic joint	mm
$\mathbf{o}_2$	3D vector identifying the position of the passive rotary joint attached to the Agile Eye's end-effector	mm
$\mathbf{p}$	3D vector identifying the origin of the global reference frame	mm
P	3D Cartesian reference frame with origin at point $\mathbf{p}$	
Q_i	generalized forces acting on the i^{th} limb	N
R_{AB}	transformation matrix converting vector representation to generalized frame A from generalized frame B upon pre-multiplication by this matrix	
r_b	base platform radius	mm
$R_{i,\varepsilon}$	right-hand rotation matrix about axis generalized i through generalized angle ε	
R_{ij}	transformation matrix converting vector representation to frame i from frame j upon pre-multiplication by this matrix	mm
r_m	moving platform radius	mm
$\mathbf{s}$	3D vector identifying the centre-of-rotation of the Agile Eye manipulator	mm
S	3D Cartesian reference frame with origin at point $\mathbf{s}$	
U	potential energy	j
$\mathbf{u}_i$	direction vector specifying the axis of the Agile Eye system's i^{th} active joint	
$\mathbf{v}_i$	direction vector specifying the axis of the Agile Eye system's joint connecting the i^{th} limb to the end-effector	
$\mathbf{w}_i$	direction vector specifying the axis of the Agile Eye system's joint between the linkages of the i^{th} limb	
x_a	x-axis of generalized frame A with origin at generalized vector $\mathbf{a}$	mm
x_i	the x-axis of the i^{th} frame	
x_{ji}	the x-coordinate of the position for joint j on limb i	mm
y_a	y-axis of generalized frame A with origin at generalized vector $\mathbf{a}$	mm
y_i	the y-axis of the i^{th} frame	
y_{ji}	the y-coordinate of the position for joint j on limb i	mm
z_a	z-axis of generalized frame A with origin at generalized vector $\mathbf{a}$	mm
z_i	the z-axis of the i^{th} frame	
z_{ji}	the z-coordinate of the position for joint j on limb i	mm
α_1	scalar constant specifying the angle between each $\mathbf{u}_i$ vector and corresponding $\mathbf{w}_i$ vector	

α_2 scalar constant specifying the angle between each $\mathbf{w_i}$ vector and corresponding $\mathbf{v_i}$ vector

β scalar constant specifying angle between any $\mathbf{v_i}$ vector and the G frame's z_g-axis when the Agile Eye is configured to its 'home' state, degrees

γ scalar constant specifying the angle between any $\mathbf{u_i}$ vector and the G frame's z_g-axis

δ_2 scalar constant specifying the angle between the z_f-axis and line connecting $\mathbf{o}_1$ and $\mathbf{f}$ projected in the x_s-z_s plane, degrees

δ_4 scalar constant specifying the angle between the z_f-axis and line connecting $\mathbf{o}_1$ and $\mathbf{f}$ projected in the y_s-z_s plane, degrees

η_i scalar constant specifying the location of $\mathbf{u_i}$ and $\mathbf{v_i}$ within the x_g-y_g plane

θ rotation of the end-effector about the positive global x-axis

θ_a x-axis rotation of the generalized frame A (associated with generalized vector $\mathbf{a}$) under roll-pitch-yaw fixed-frame parameterization

θ_a^* x-axis rotation of the generalized frame A (associated with generalized vector $\mathbf{a}$) under fixed-frame x-axis, fixed-frame y-axis, and then current-frame z-axis rotation parameterization

θ_i rotation of the i^{th} limb with respect to the negative x-axis

μ manipulability

μ_{iso} isotropic manipulability index

ν local dexterity index

σ_{max} maximum singular value of a Jacobian matrix

σ_{min} minimum singular value of a Jacobian matrix

τ_r sensitivity index

ϕ rotation of the end-effector about the positive global y-axis, degrees

ϕ_a y-axis rotation of the generalized frame A (associated with generalized vector $\mathbf{a}$) under roll-pitch-yaw fixed-frame parameterization

ϕ_a^* y-axis rotation of the generalized frame A (associated with generalized vector $\mathbf{a}$) under fixed-frame x-axis, fixed-frame y-axis, and then current-frame z-axis rotation parameterization

ψ rotation of the end-effector about the positive global z-axis

ψ_a z-axis rotation of the generalized frame A (associated with generalized vector $\mathbf{a}$) under roll-pitch-yaw fixed-frame parameterization

ψ_a^* z-axis rotation of the generalized frame A (associated with generalized vector $\mathbf{a}$) under fixed-frame x-axis, fixed-frame y-axis, and then current-frame z-axis rotation parameterization

Chapter 1.

Introduction

1.1. Research on Existing Lower Limb Exoskeletons

Human locomotion can be influenced by several factors such as neuromuscular and joint disorders. These factors affect the functionality of joints in hip, knee and ankle in many individuals and can cause partial or complete paralysis depending on the level of its development. Many individuals require mobility assistive technologies to keep up with their daily life and the demand for such devices typically increases with age. A wearable exoskeleton robot is an external structural mechanism with joints and links corresponding to those of a human body. The exoskeleton directly interacts and synchronizes with human body to enhance or support its natural movements in order to augment the lack of power in conducting daily activities. The exoskeleton transmits torques from its actuators through rigid exoskeletal links to the human joints, thereby providing mobility and augmenting the strength.

Lower limb exoskeletons are mainly designed and planned for two types of applications. The first application focuses on gait rehabilitation and assistance in human locomotion and the second application is aimed at increasing and enhancing the physical abilities of able-bodied humans (i.e. human strength augmentation). [1]–[3]

1.1.1. Lower Limb Exoskeletons for Gait Rehabilitation and Locomotion Assistance

Elderly people and overall people with disabilities usually have weak and limited strength and may not be able to walk as easy and frequent compared to normal people and may even lose their stability while they are walking. In order to enhance their walking capabilities, intensive exercises should be followed during rehabilitation

therapies. The nature of the majority of those exercises are repetitive and involves continues training which is very subjective and patients progress are difficult to assess [4]. Lower limb exoskeletons developed for rehabilitation can assist therapists in training patients in doing repetitive motions. In addition, therapists can gain more control on planning the therapy steps by analyzing the patient's gait performance. Moreover, by employing robotic rehabilitations, the pace of recovery of the patients can be assessed with the forces or torques measured by the sensors [5].

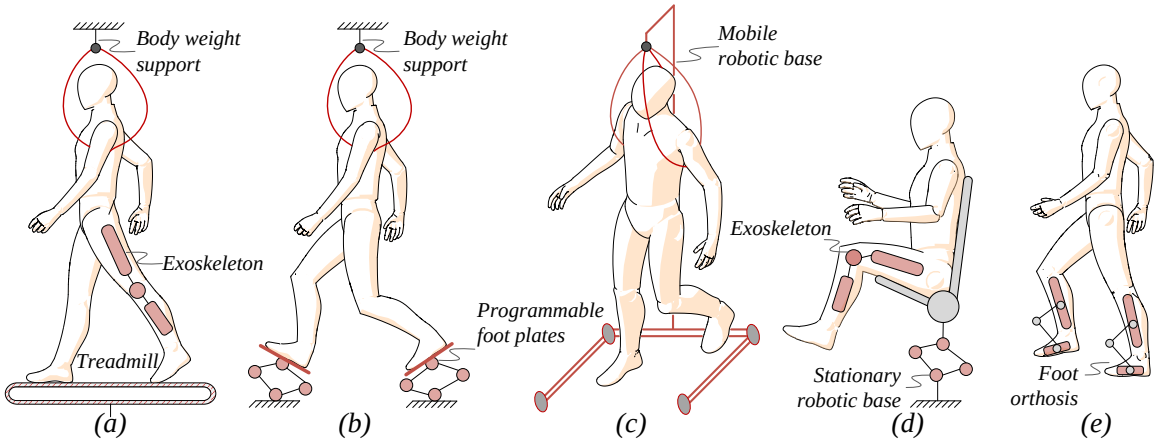

Figure 1.1. Lower limb rehabilitation systems a) treadmill gait trainer, b) foot-plate, c) over ground, d) stationary and e) modular orthosis

In addition to robotic rehabilitation, there are other types of lower limb exoskeletons that are developed for human locomotion assistance and are primarily used to help paralyzed patients who have completely lost mobility in the lower limbs. Exoskeletons can provide external torque to enable human joints to move, and thereby provide the patients with the desired strength to regain the ability to perform daily life activities such as standing up, sitting down, and walking. Over the last decade several lower limb exoskeletons have been developed to address these issues. Overall, these type of systems are shown in Figure 1.1.

In what follows, a brief summary of some well-known lower limb exoskeletons is introduced. A number of exoskeleton devices are designed by the Berkeley Robotics and Human Engineering Laboratory (at the University of California, Berkeley), Ekso Bionics (formerly Berkeley Bionics) and US Bionics for rehabilitation of injured and partially disabled users with some forms of paralysis or hemiparesis. These devices include eLEGS, Austin, ExoLight, and Ekso GT, shown in Figure 1.2 [6]–[8]. Each of

these devices includes powered actuators located at one or more exoskeleton joints. The feature that all these devices have in common is their claimed light weight. The characterized major setback of all these devices, however, is their limited ranges of motion and limited DOF. As it can be seen in Figure 1.2, the hip actuators of these exoskeletons is 1-DOF, which is not sufficient to assist users with all natural 3-DOF capability of the hip joint. Similar to the designs shown in Figure 1.2 are the exoskeleton systems developed at Vanderbilt University (commercialized as Indego), the Russian ExoAtlet project, the Israeli ReWalk exoskeleton produced by ReWalk Robotics as well as the Walk Again Project conducted by a team of Belgian researchers. These systems, shown in Figure 1.2 [9]–[11] are all made for the rehabilitation of paraplegic users. Since these devices are also limited to have 1-DOF active actuation on the hip joint, they would thereby require the users to maintain their balance with crutches to prevent unwanted falls.

Figure 1.2. a) eLEGS, b) Austin, C) Exolight, d) Ekso GT, e) Vanderbilt, f) Indego, g) ExoAtlet, h) ReWalk, i) REX, j) MindWalker, k) HAL and l) Body Weight Support Assist

The exoskeletons developed by REX Bionics and MindWalker, shown in Figure 1.2(i) and 1.2(j), fundamentally differ from those discussed above because it does not require the concurrent use of any crutches or walking assists. It also provides powered guidance to both flexion/extension and abduction/adduction movements at the hip. However, the REX systems are consequently larger and heavier. Nonetheless, these designs still do not provide active 3-DOF movement at the hip joint. As a result, the user has to be externally supported to maintain balance while wearing these devices [12], [13].

While most exoskeleton technologies developed for rehabilitation purposes cater to those with paraplegia or other conditions, some designs are intended for those who have weakened leg muscles or must perform repetitive or prolonged tasks with their legs for rehabilitation. Prominent examples of these types of systems are Cyberdyne's Hybrid Assistive Limb (HAL) and Honda's Walking Assist. HAL is intended for people with weakened leg muscles and, like previously mentioned exoskeleton systems, utilizes powered 1-DOF actuators at the hip joint. HAL has been certified as a medical treatment device in the European Union. Honda's Stride Management Walking Assist uses a motor to help those with weakened leg muscles achieve longer strides while walking. unlike other designs mentioned, the Stride Management Assist only includes hip joints and thigh supports. Contrarily, Honda's Bodyweight Support Assist provides full limb support and is intended to decrease fatigue and physical exertion experienced by the user. The exoskeleton devices produced by Cyberdyne and Honda are shown in Figure 1.2 (k) and 1.2(i) [14], [15].

1.1.2. Lower Limb Exoskeletons for Human Strength Augmentation

Lower limb exoskeletons developed for human augmentation can enhance human strength and endurance during locomotion and enable them to execute tasks that they cannot easily perform by themselves. They provide users, the ability to transport heavy loads. The Berkeley Robotics and Human Engineering Laboratory has developed at least four stages of military exoskeleton design. First, the Berkeley Lower Extremity Exoskeleton (BLEEX) was designed and built to support loads placed in the system's backpack in an effort to enhance human strength and endurance [16]. According to [17], the BLEEX design initially provided power actuation for the flexion/extension motion of the hip joint, as this movement requires the most power while walking; but active

actuation for abduction/adduction motion was also added to better facilitate lateral balance. Since an offset exists between the exoskeleton limb and human limb, at least one axis of rotation of the exoskeleton hip joint cannot coincide with that of the human hip. thus, relative motion occurs between the two limbs for at least one rotation type of the hip, and length adjustment in the exoskeleton limb is subsequently required to maintain alignment of the human and machine hip joints. The BLEEX design facilitated this length adjustment by positioning the system's abduction/adduction axis of rotation coincident to that of the user, while allowing the center of flexion/extension rotations to move in order to maintain proper alignment with the user's hip joint [18]. The BLEEX design also allows for passive internal/external rotation of the hip joint through a single joint posterior to the user [17]. Figure 1.3 shows a user wearing the BLEEX exoskeleton along with a schematic of the system's hip component. The BLEEX system is primarily powered by linear hydraulic actuators.

The team at UC Berkeley also developed a second military exoskeleton named the ExoHiker [19]. The primary improvements to the BLEEX design realized by the ExoHiker were the substantial reduction in system weight, simplification in control, and increased load support capability [23]. Another device designed by the Berekely team, called the ExoClimber, was also developed and aimed to allow for rapid vertical ascent (i.e. on stairs or steep terrain) while maintaining the other features of ExoHiker [20]. The technology developed through the ExoHiker and ExoClimber designs were then combined and extended into a third generation design named the Human Universal Load Carrier (HULC); according to [21], the main characteristics of the HULC system are the ability to support 200lbs without user effort and to decrease the metabolic cost experienced by the user. Figure 1.3 shows the ExoHiker, ExoClimber, and HULC designs [22]. The Russian team responsible for the ExoAtlet rehabilitation system has also developed a system for military and search and rescue applications. Based on the video demonstrations of this system, it is apparent that the exoskeleton is capable of at least flexion/extension and abduction/adduction motion at the hip joints. Furthermore, the advertised design capabilities of this system include: strength and endurance augmentation, escalation of gait speed while carrying loads, improved jumping ability, and mounting capability for combat shields. Figure 1.4 shows a user wearing this exoskeleton.

(a) *(b)* *(c)* *(d)* *(e)* *(f)*

Figure 1.3. a) BLEEX, b) ExoHiker, c) Exoclimber, d) HULC, e) ExoAtlet and f) XOS

The Massachusetts Institute of Technology (MIT) has also developed an exoskeleton for load carrying augmentation during a research project under contract of the Defense Advanced Research Projects Agency (DARPA). This device is designed to provide 3-DOF movement at the hip joint. Flexion/extension motion is facilitated by a rotary joint with axis of rotation coincident to that of the biological limb. Abduction/adduction is permitted by a cam mechanism, and finally internal/external rotation is enabled by a rotary joint above the knee. Actuation of the hip joint was tested in two phases [23]. First, unidirectional springs were used to augment flexion/extension and abduction/adduction. The second phase replaced the spring associated with flexion/extension motion and replaced it with a powered actuator. It follows that active actuation of the hip joint for all DOFs was not accomplished [24]. Other noteworthy exoskeletons designed and built for military applications are the XOS 1 and its second generation successor, XOS 2. Work on the XOS 1 system was initiated by Sarcos Research in Salt Lake City, Utah in 2000 under DARPA funding. In 2007, Sarcos Research was acquired by Raytheon and the first generation XOS 1 system was publically announced for the first time in 2008. In 2010, XOS 2 was unveiled and publically demonstrated. The advertised capabilities and features of the second generation system include: the ability to lift objects at an actual-to-perceived weight ratio of 17:1 (up to about 200 lbs), the use of lighter-weight materials than its predecessor, and energy efficiency 50% increased from XOS 1 [25]. Like the BLEEX system, the XOS systems are primarily powered by hydraulics [25]; however, sufficient energy provision to the system currently requires that the exoskeleton be tethered to a stationary power

source. Based on demonstrations given for the XOS 2 exoskeleton, it is also likely that the system features similar hip joint capabilities as the BLEEX. Figure 1.3 shows the generation of XOS exoskeleton [25], [26].

Chapter 2. Design Objectives and Constraints

2.1. Background and Motivation

An estimated 20,639,200 (7.1%) of non-institutionalized United States residents suffered from an ambulatory disability in 2013, while an approximated 2,512,800 (7.2%) of Canadians reported mobility disablements in 2012. These disabilities cost an estimated annual equivalent of $375 billion in family caregiver support, in addition to significant economic and social burdens to the patient and the healthcare system [27], [28].

One emergent technology that aims to improve the quality of life for sufferers is the lower-body exoskeleton: wearable robotic systems that completely or partially support their user's weight. It provides controlled guidance of leg movements, thereby allowing their user to stand and walk. This solution provides benefits over wheelchair use and other traditional means because it can also help reduce secondary complications of immobility such as pneumonia, blood clots, pressure sores, and lowered self-esteem. Although exoskeletons are an emerging solution to mobility issues and injury rehabilitation, current products have several important limitations. These disadvantages are mainly associated with limited ability to guide the hip joint through its full ranges of motion and user's dependency on sticks and crutches to maintain their balance. Of the various exoskeleton systems currently on the market, a few of the most prominent models are intended for rehabilitation and mobility assistance purposes. First, demonstrations of these systems reveal that they focus on or are limited to one degree-of-freedom (DOF) active rotation at each joint. Therefore, their users are unable to move with the full range of motion. In order to have a better understanding on the characteristics of the lower limb exoskeleton, one should have a clear vision on the anatomy of the human body and the ranges of motion its joints exhibit.

2.2. Hip Exoskeleton Design by Biological Analogy

The exoskeleton is a mechanism that acts in parallel to the limb and ideally move with the limb at any given time without restricting its natural motion. This would imply that the kinematics of the desired exoskeleton would be similar to a human's lower limb. This means that the exoskeleton mechanics would have to comply with that of the limb, and not interfere with its natural motion. In an ideal case, the joint center of rotation of the exoskeleton should be perfectly aligned with that of the limb, have adequate DOF to allow a free and unconstrained motion of the limb, and also be able to provide torques at the joints. In general, the human leg can be represented as a 7-DOF structure, with three rotational DOFs at the hip, one at the knee, and three at the ankle [29]. Figure 2.1 shows an illustration of the human anatomical planes.

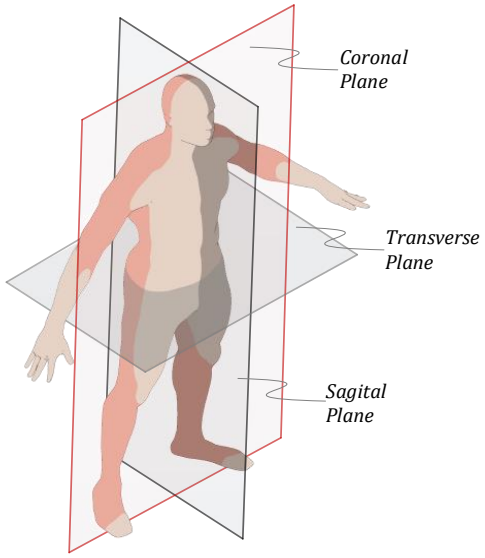

Figure 2.1. Description of anatomical planes related to lower extremity motions

In this thesis, for the hip joint, motion in the sagittal plane is simply referred to as flexion (positive direction) and extension (negative direction). Motions of the hip joint in the coronal plane are respectively referred to as abduction and eversion when they are directed away from the centre of the body; alternatively, the motions are called adduction of the hip when they are directed towards the centre of body. The remaining DOFs of the hip are related to as internal-external rotation that occur in the transverse plane.

2.2.1. Biomechanics of Human Locomotion

Understanding the biomechanics of human walking is crucial in the design of exoskeletons and device orthoses for the lower limbs. Since our intention is to design a light-weight anthropomorphic hip exoskeleton, the required joint torques and power for the exoskeleton to perform a given motion were approximated as that required by an average sized human performing the same motion. Additionally, since the primary goal of a lower-extremity hip exoskeleton is locomotion, the joint power requirements were determined by analyzing the walking gate cycle of an average weight, 75-kg human walking on a flat ground at an approximate speed of 1.3 m/s which is the average speed of a human walking gait. Shown in Figure 2.2, adapted from [30], [31], shows a simplified diagram of human walking gait, with the corresponding terms that will be used throughout this thesis. The human walking gait cycle is typically represented as starting (0%) and ending (100%) at the point of heel strike on the same foot.

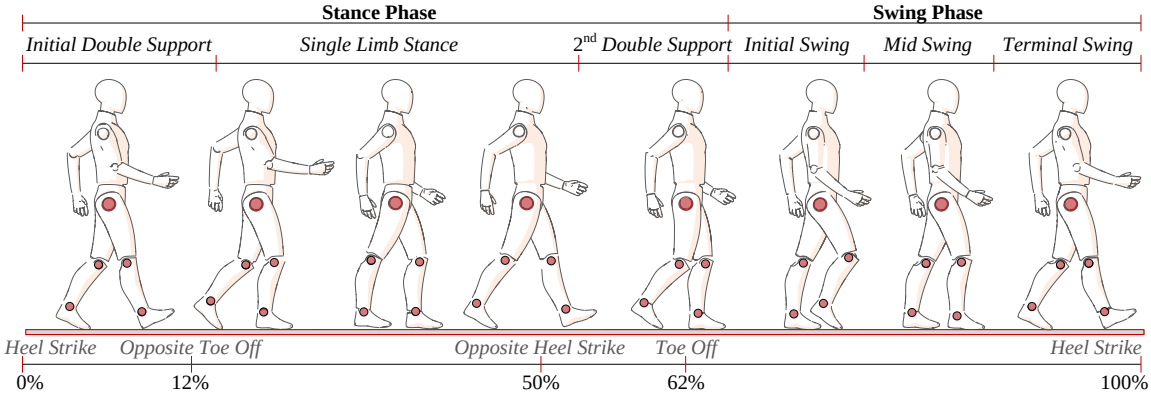

Figure 2.2. Human walking gait through one cycle

Human joint angles and torques for a typical walking cycle were obtained in the form of independently collected CGA (i.e. Clinical Gait Analysis) data [32]–[34]. This data can then be further modified to yield estimates of exoskeleton actuation requirements.

2.3. Functional Specifications

The functional specifications that this research project aims to achieve are as follows: First, the prototype hip must be able to conduct all motions associated with a

normal walking gait pattern. The gait simulation files publically available through Stanford University's OpenSim software will be used to define and evaluate this specification [35]. Second, the exoskeleton kinematics are close to human leg kinematics and, therefore, the exoskeleton ranges of motions are determined by examining human joint ranges of motion. The exoskeleton range of motion should be close to the human range of motion during walking for safety reasons [29]. These ranges of motion have been summarized and shown in Figure 2.3.

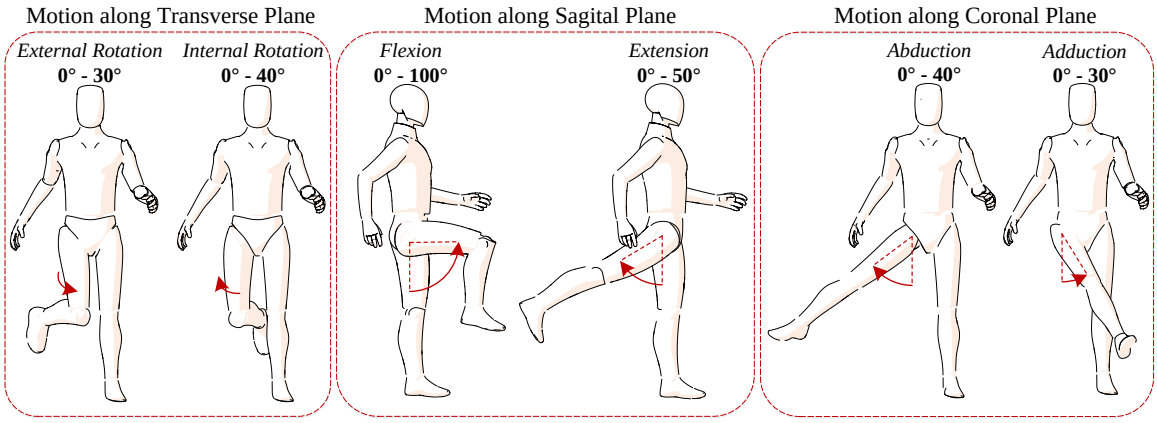

Figure 2.3. Ranges of motion for human hip joint

The range of motion requirements of a joint depend on the application. For instance, if a person is practicing to regain his/her ability to walk, then the range of motion of an assistive exoskeleton could be the range for normal walking, plus some extra degrees as a safety margin. In this study we have aimed to investigate the design of an hip exoskeleton that is capable to assist the user during a walking gait. Based on this objective the functional specifications for the lower limb hip exoskeleton are planned as follows:

- Generic compatibility with disabilities, ranging in severity from muscle weakness to complete paraplegia,
- Simplicity in construction and ease of use and wear
- Exoskeleton hip must have 3-DOF active actuation in orientation workspace
- Exoskeleton hip joint must guide upper leg flexion to the extent of 90°
- Exoskeleton hip joint must guide upper leg extension to the extent of 50°
- Exoskeleton hip joint must guide upper leg abduction to the extent of 40°

- Exoskeleton hip joint must guide upper leg adduction to the extent of 30°
- Exoskeleton hip joint must guide upper leg internal rotation to the extent of 40°
- Exoskeleton hip joint must guide upper leg external rotation to the extent of 30°

2.4. Design Objectives

Although the use of exoskeletons as mobility assistive devices have reduced health concerns, there still exist several major shortcomings with currently available systems. As discussed earlier in Chapter 1, most of the current hip exoskeletons are designed to have 1-DOF active actuation and lack the capability to provide and assist the user with other ranges of motions necessary for the hip joint. This is primarily due to the fact that such devices are designed as serial manipulators which consist of a number of rigid links connected in series with active joints. Incorporating such type of a structure on a hip exoskeleton is considered to be extremely difficult since the active counterparts of such mechanisms must be exactly aligned and fixed with respect to the axis of rotation of the human hip joint. Any misalignment between the active axis of actuation of the hip exoskeleton and the users hip joint would result in malfunction and possible injuries to the user. As presented in Chapter 1, the hip exoskeleton devices that have more than 1-DOF, utilize a maximum of three serially connected and chained manipulators. This type of a design forces each actuator to support the weight of its successor links and therefore have poor payload-to-weight characteristics. The accuracy in positioning the payload and speed of manipulation is another traditional shortcoming of serial manipulators. In general, current technologies actively guide one degree-of-freedom hip-centered movements with absent or only passive guidance for one or both of the other DOFs. This would restrict the natural range of motion on human joints capable of multiple DOFs rotations. Current exoskeletons are commonly bulky and heavy since they use serial counterparts within their structure [36]. This project plans to address this issue by designing and developing a lower-limb hip exoskeleton system with parallel manipulators incorporated as robotic hip joints. Parallel manipulators provide greater payload-to-weight ratio, positioning accuracy, and speed capabilities than are possible with their serial manipulator counterparts. This dissertation focuses on the exoskeleton hip joint because it is the center of the largest range of motion and

torque production on the human leg. Schematics of serial and parallel manipulators are illustrated in Figure 2.4.

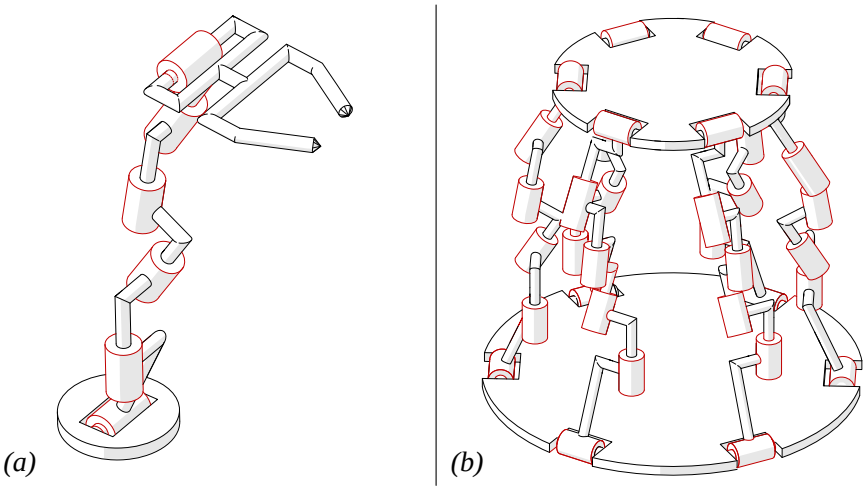

Figure 2.4. Different architectures of robotic manipulators, a) serial and b) parallel

Given the anatomical features of the human hip joint and surrounding bodily structures, the design of a compatible exoskeleton hip joint is the most complex problem in a wearable anthropomorphic lower limb exoskeleton project. Consequently, the hip joint structure alone has been the subject of several design concept generations, which led to the various design alternatives presented in this study.

This project aims to develop a hip exoskeleton system intended for people suffering lower-body disabilities and to improve upon existing mobility assistive technologies.

2.5. Thesis Objective and Outline

The main objective of this research and development project is to develop a new generation of wearable lower limb hip exoskeleton that can provide a versatile solution for people with mobility disability. To begin with, The application of parallel manipulator to recuperate the expected functionality and motion in the hip joint is investigated by incorporating the well-known Stewart-Gough. Stewart platforms are 6-DOF parallel robots that have many advantages over conventional serial robots including high

payload to volume density, high speed and accuracy. The utilization of Stewart-Gough platforms as the hip exoskeleton will also bring the versatility and maneuverability in the exoskeleton and thereby make it a more synchronized structure with human hip motion. It has been shown that the Stewart-Gough platform is fully capable of being utilized to actively guide the hip joint, however, it is preferred to find simpler solutions that have less number of actuators. In fact, a more compact robotic joint that can also satisfy the size limitations of the final exoskeleton is preferred.

As an alternative to Stewart-Gough platform, Chapters 4 and 5 of this thesis focus on exploring mechanisms capable of active 3-DOF rotational motions. Potentially, these mechanisms are able to fully define the position of the hip joint if the transmitting mechanism is designed properly.

In summary, Chapter 4 details the proposed design, kinematical analysis, performance indices, and recommended implementation of one possible solution: a 3-RUS/S parallel manipulator. Experimental results obtained from a prototype device during a gait motion tracking study are presented. It follows from this structure that the 3-RUS/S manipulator provides decoupled and active 3- DOF rotational motions to its end-effector, thus characterizing the device as an orientation parallel manipulator. The advantages of using 3RUS/S mechanism as the actuating part of the hip exoskeleton can be attributed to its easy control algorithm and simple inverse kinematics. The mechanism however has some shortcomings which are mainly related to its mechanical characteristics. The main issue is that the system incorporates a universal and a spherical joint on each link and the moving platform is also constrained by a spherical joint. In real applications, these joints by nature would decrease the overall allowable workspace of the mechanism.

To find a more optimized and reliable manipulator, Chapter 5 investigates the performance of the 3-RRR spherical parallel manipulator. Specifically, manipulability, dexterity, and rotational sensitivity performance indices are evaluated for two different body-interfacing schemes of the manipulator. Our findings suggest a 3-RRR spherical parallel manipulator can be employed as the hip actuator in an exoskeleton system; this represents an original contribution to the field of exoskeleton research.

Chapter 6 and 7 entails a 3-DOF motion-generation system that is mechanically capable of providing decoupled or combined 3-DOF rotational motion or inaction to a separate and passive target system (i.e. hip joint). The motion-generation system which is the 3-RRR spherical manipulator (i.e. Agile Eye), conveys mechanical action to the target system via a motion transfer and target interfacing system, which physically supports the target system in some extent and converts action from the motion-generation system to desired movements of the target system about its true or quasi 3-DOF rotational joint. The motion-generation system is additionally capable of causing the target system to hold a constant angular position about its true or quasi 3-DOF rotational joint.

In summary Chapter 6 and 7 present a novel hybrid mechanism, incorporating the well-established Agile Eye, that enables decoupled and orientation guidance of a ball-and-socket or spherical joint. The kinematic architecture associated with the design is described and both inverse and forward kinematic analyses for the complete mechanism are detailed. With focus on hip exoskeleton application, simulation results are presented as verification of the inverse kinematics algorithm. Furthermore, the results obtained from a prototype device during a gait motion experiment are documented as an indication of the device's ability to convey and guide 3-DOF rotational motion to a ball-and-socket joint.

2.6. Contributions

The present study entails 3-DOF motion-generation system that is mechanically capable of providing decoupled or combined 3-DOF rotational motion or inaction to a separate and passive target system by way of a transfer and interfacing system. The target system may be any structure containing a 3-DOF rotational joint (e.g. ball-and-socket joint) or a quasi-3-DOF rotational joint. The motion-generation system conveys mechanical action to the target system via a motion transfer and target interfacing system, which physically supports the target system in some extent and converts action from the motion-generation system to desired movements of the target system about its true or quasi 3-DOF rotational joint. Furthermore, with regard to any interfaced protrusion from the target joint, the motion transfer and target interfacing system

prevents or minimizes forces along the protrusion’s axis passing through the target joint, thereby reducing the risk of damage to the target system. The motion-generation system is additionally capable of causing the target system to pause and hold a constant angular position about its true or quasi 3-DOF rotational joint.

Chapter 3. Performance Analysis of 6-UPS Parallel Manipulators for Lower Limb Exoskeleton Applications

An exoskeleton is a wearable robotic device intended to augment the abilities of the human body segment to which is attached. Common motivations for exoskeleton use are energy conservation for limbs that are otherwise functional or strength augmentation for limbs that have weakened or complete loss of functionality. One significant challenge associated with either of these goals arises when the targeted limb contains a joint with multiple active degrees-of-freedom (DOFs) that must be supported by an external robotic structure.

One candidate robot that may be used to overcome this challenge is the 6-UPS parallel manipulator, which is also commonly referred to as the Stewart-Gough platform. This manipulator has been extensively analyzed and proposed for use in a number of different technology applications. First, Stewart introduced the mechanism and suggested application as a flight simulator for pilot training in [37]. Later, Merlet and Tsai among others revisit the device and discuss its kinematical and Jacobian matrix analyses [38], [39]. Additionally, Gosselin presents a method of inverse kinematics development and workspace analysis for the Stewart-Gough platform in [40]. Abedinnasab and Vossoughi also present a performance analysis of the mechanism when the device is limited to planar translational motions in [41]. More recently, Takaiwa *et al.* discuss the use of a pneumatically-actuated Stewart-Gough platform for use in wrist rehabilitation [42], while Onodera *et al.* propose an assistive device incorporating a Stewart-Gough platform for ankle-foot rehabilitation [43]. This chapter explores the use of the 6-UPS manipulator within a hip exoskeleton system. Specifically, this study revisits the inverse kinematics and Jacobian development processes for the Stewart-Gough platform and then analyzes its performance for two different body attachment schemes and three different intra-device limb arrangements.

3.1. Kinematic Analysis & Geometry Consideration

3.1.1. Structure Description

Figure 3.1 shows a geometrical schematic of a 6-UPS parallel manipulator. As shown in the schematic, six identical limbs connect a moving platform to a fixed base via spherical joint connections to the fixed base at points A_i and universal joint connections to the moving platform at points B_i , for $i = 1,2,\ldots, 6$. Each limb consists of an upper member and a lower member connected by an active prismatic joint. Actuated ball screws, hydraulic jacks, or other linear actuators can be used to vary the lengths of the prismatic joints and thereby control the position and orientation of the moving platform.

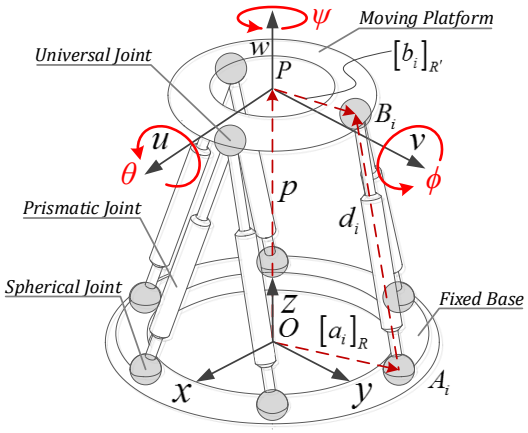

Figure 3.1. Schematic model of a 6-UPS parallel manipulator

Stewart-Gough platforms can have various different manifestations depending on how the joints on the moving platform and fixed base are configured. This study considers three common design schemes of the Stewart-Gough platform (see Figure 3.2) as possible candidates for utilization in a lower extremity exoskeleton hip joint.

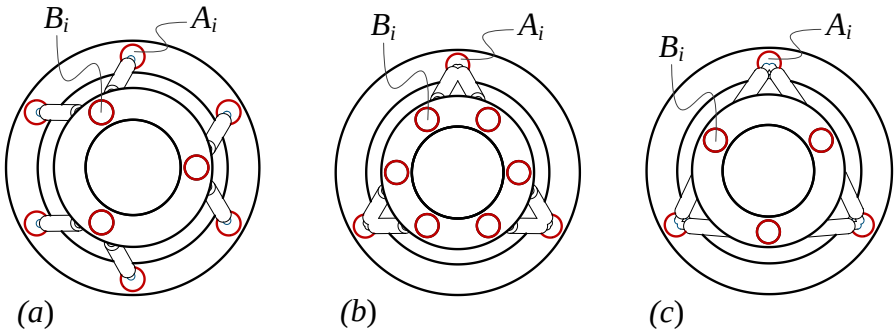

Figure 3.2. Top view of a) 6-3, b) 3-6, and c) 3-3 Stewart-Gough platforms

3.1.2. Inverse Kinematics

The inverse kinematics analysis for the 6-UPS manipulator has been extensively studied previously by a number of academics [38–40]. However, the procedure is briefly outlined here again for the sake of completeness and to familiarize the reader with the notations and naming conventions used in subsequent sections of this study. First, consider two Cartesian coordinate systems: frame R attached to the base with axes x,y, and z, and frame R' attached to the moving platform with axes u, v and w, as shown in Figure 3.1. Note that the origin of frame R', denoted P, is located on the central axis of the moving platform and lies in the plane defined by the universal joint attachment points.

Vectors $\mathbf{a}_i$ and $\mathbf{b}_i$ respectively designate the positions of each spherical and universal joint, where the subscript i differentiates the six limbs (i.e. $i = 1,2,\ldots, 6$). Because the spherical joints and frame R are both attached to the fixed base structure, vectors $\mathbf{a}_i$ are constant when expressed in frame R. Similarly, vectors $\mathbf{b}_i$ are constant with respect to frame R'.

Furthermore, Q is the transformation matrix describing the orientation of R' with respect to fixed frame R. This transformation is uniquely defined by roll, pitch, and yaw rotation angles. Specifically, Q is produced by a rotation of θ about the fixed x-axis, followed by a rotation of ϕ about the fixed y-axis, and then a final rotation of ψ about the fixed z-axis. Mathematically, it follows that the orientation of the moving platform frame with respect to the base platform frame is obtained as shown in Eq. (3.1):

$$\boldsymbol{Q} = \boldsymbol{Q}_z \boldsymbol{Q}_y \boldsymbol{Q}_x = \begin{bmatrix} C\psi C\phi & C\psi S\phi S\theta - S\psi C\theta & C\psi S\phi C\theta + S\psi S\theta \\ S\psi C\phi & S\psi S\phi S\theta + C\psi C\theta & S\psi S\phi C\theta - C\psi S\theta \\ -S\psi & C\phi S\theta & C\phi C\theta \end{bmatrix} \tag{3.1}$$

If the position of point P with respect to the origin of the fixed coordinate frame R is denoted by vector $[\boldsymbol{r}]_R = [x_r, y_r, z_r]^T$, each vector $\mathbf{b}_i$ can be expressed in frame R as follows:

$$\left[\boldsymbol{b}_i\right]_R = \left[\boldsymbol{r}\right]_R + \boldsymbol{Q}\left[\boldsymbol{b}_i\right]_{R'} \qquad i = 1,\ldots,6 \tag{3.2}$$

where the subscript outside of the brackets indicates the coordinate frame in which the associated vector is expressed. Now, subtracting $\boldsymbol{a}_i$ from both sides of Eq. (3.2) provides a vector directed along the i^{th} limb, connecting point A_i to B_i:

$$\left[\boldsymbol{b}_i - \boldsymbol{a}_i\right]_R = \left[\boldsymbol{r}\right]_R + \boldsymbol{Q}\left[\boldsymbol{b}_i\right]_{R'} - \left[\boldsymbol{a}_i\right]_R \qquad i = 1,\ldots,6 \tag{3.3}$$

Thus, the Euclidean norm of each side of Eq. (3.3) produces

$$d_i = \left\|\boldsymbol{b}_i - \boldsymbol{a}_i\right\| = \left\|\left[\boldsymbol{r}\right]_R + \boldsymbol{Q}\left[\boldsymbol{b}_i\right]_{R'} - \left[\boldsymbol{a}_i\right]_R\right\| \qquad i = 1,\ldots,6 \tag{3.4}$$

where d_i is a scalar measure of the i^{th} limb's length. Note that an alternative form of Eq. (3.4) is as follows:

$$d_i = \sqrt{\left(x_r - u_i\right)^2 + \left(y_r - v_i\right)^2 + \left(z_r - w_i\right)^2} \qquad i = 1,\ldots,6 \tag{3.5}$$

for which the scalar quantities u_i, v_i, and w_i are given as:

$$\begin{aligned} u_i &= x_{ai} - q_{11}x_{bi} - q_{12}y_{bi} - q_{13}z_{bi} \\ v_i &= y_{ai} - q_{21}x_{bi} - q_{22}y_{bi} - q_{23}z_{bi} \\ w_i &= z_{ai} - q_{31}x_{bi} - q_{32}y_{bi} - q_{33}z_{bi} \end{aligned} \qquad i = 1,\ldots,6 \tag{3.6}$$

In Eq. (3.6), q_{ij} is the i^{th} row – j^{th} column element of the transformation matrix Q. Eqs. (3.4–3.6) represent the solution to the inverse kinematics problem for the 6-UPS manipulator because they provide the required active joint states, d_i, necessary to achieve a desired position and orientation of the moving platform end-effector. That is, once each element of Q and $\boldsymbol{r}$ are established as inputs, associated lengths for the prismatic actuators can be identified.

3.1.3. Body Interfacing and Geometric Considerations

Depending on how the 6-UPS is interfaced with the human body for application as a hip joint exoskeleton, a number of geometric considerations are introduced that may influence the manipulator's preferred method of operation. Figure 3.3 illustrates two proposed schemes for interfacing the 6-UPS to the body.

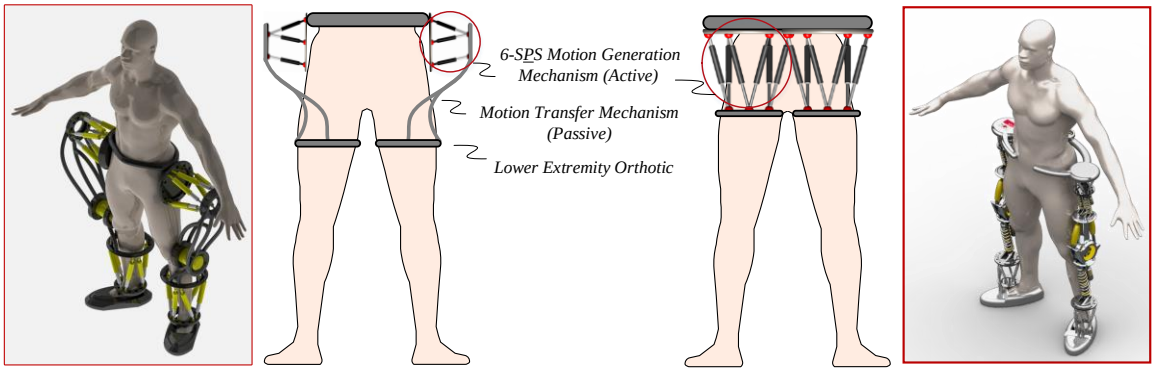

(a) Interfacing Scheme 1 *(b) Interfacing Scheme 2*

Figure 3.3. The two body interfacing schemes considered for the 6-UPS

For scheme *a*), it is assumed that the position of point P remains constant with respect to frame R. That is, the 6-UPS acts as a 3-DOF rotational joint with center-of-rotation located at point P. Mathematically, $\boldsymbol{r}$ then becomes a vector of constant values as follows:

$$[\boldsymbol{r}]_R = \begin{bmatrix} x_r \\ y_r \\ z_r \end{bmatrix} = \begin{bmatrix} 0 \\ 0 \\ P_z \end{bmatrix} \tag{3.7}$$

where P_z is the z-axis coordinate of point P's position. Figure 3.4 *a*) shows examples of moving platform orientations and positions attainable given this motion restriction. Note that for this example scenario, additional mechanisms would be required to prevent forces acting to dislocate the hip joint when transferring the 6-UPS manipulator's motions to the upper leg. These mechanisms are not discussed here.

Meanwhile, for interfacing scheme *b*) in Figure 3.4, it is assumed that the hip joint's center-of-rotation coincides with the origin O of frame R. A further assumption that no additional mechanisms are used to guide hip motions (i.e. the moving platform is

fixed directly to the upper leg) requires that point P only move along a spherical surface centered at O and that the w-axis always pass through point O. Figure 3.4 *b*) provides an illustration of this geometrical constraint on the 6-UPS motions. Furthermore, the position of P in terms of frame R is expressed as follows for this interfacing case:

$$[\boldsymbol{r}]_R = \begin{bmatrix} x_r \\ y_r \\ z_r \end{bmatrix} = \begin{bmatrix} q_{11}P_x + q_{12}P_y + q_{13}P_z \\ q_{21}P_x + q_{22}P_y + q_{23}P_z \\ q_{31}P_x + q_{32}P_y + q_{33}P_z \end{bmatrix} \tag{3.8}$$

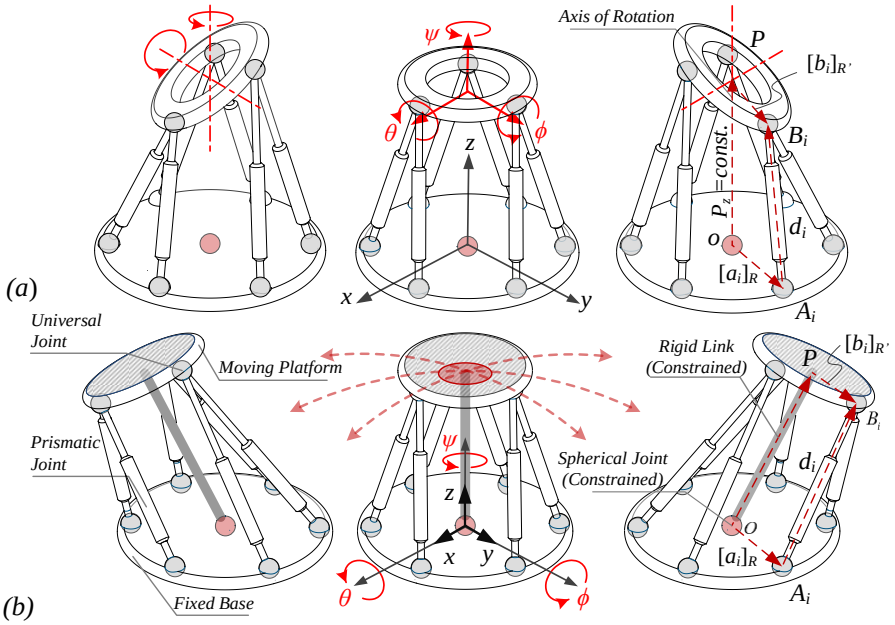

Figure 3.4. Example of 6-UPS motions for two considered methods of operation

where q_{ij} is the i^{th} row – j^{th} column term in the Q matrix of Eq. (3.1). Additionally, P_k is the k-coordinate of P expressed in the R frame when the manipulator is fitted on the upper leg and it is in its starting position. Note that Figure 3.4 *b*) shows the case for which $P_x = 0$ and $P_y = 0$ in Eq. (3.8).

3.2. Jacobian Analysis of the 6-UPS Manipulator

A number of indices are commonly used to compare the performance of different parallel manipulator mechanisms [36]. These indices are generally acquired from a manipulator's Jacobian matrix and often have physical significance that lends itself for use as an objective function for design optimization [44]. Therefore, the 6-UPS manipulator's Jacobian is discussed before performance indices are analyzed in Sections 3.3. The definition of the performance indices used in this study is briefly summarized in Appendix A. Note that Merlet and Tsai also present Jacobian studies for the 6-UPS manipulator in [38],[39] among others.

To start, a vector $\mathbf{q}$ is assigned to describe the active articular variables, and vector $\mathbf{x}$ is set to denote the moving platform position. It follows that Eq. (3.9) represents the kinematic constraints asserted by the manipulator's limbs in general form:

$$f\left(\mathbf{x},\mathbf{q}\right) = \mathbf{0} \tag{3.9}$$

where f is an n-dimensional implicit function of $\mathbf{q}$ and $\mathbf{x}$, and n is the device's active joint count (i.e. $n = 6$ for the 6-UPS). Time-differentiation of Eq. (3.9) yields the following relationship between the input joint rates and the end-effector output velocity:

$$\frac{\partial \mathbf{f}}{\partial \mathbf{x}}\dot{\mathbf{X}} + \frac{\partial \mathbf{f}}{\partial \mathbf{q}}\dot{\mathbf{q}} = 0 \rightarrow \mathrm{J}_x\dot{\mathbf{X}} = \mathrm{J}_q\dot{\mathbf{q}} \tag{3.10}$$

The J_x and J_q components in the above equation are then combined into the complete Jacobian matrix:

$$\dot{\mathbf{q}} = \mathrm{J}_q^{-1}\mathrm{J}_x\dot{\mathbf{X}} = \mathrm{J}\dot{\mathbf{X}} \tag{3.11}$$

Note that the Jacobian of a parallel manipulator is inverted compared to that of a serial manipulator [39].

Next, the velocity vector-loop closure method is used to analyze the Jacobian matrix. Each loop includes points on the fixed base, moving platform, and all links of a limb, as follows:

$$\overline{OP} + \overline{PB_i} = \overline{OA_i} + \overline{A_iB_i} \tag{3.12}$$

The velocities associated with passive joints are eliminated by taking a dot product of the velocity vector-loop equation above with an appropriate vector normal to all vectors representing passive joint rates. Lastly, the resulting equations are combined to create a Jacobian matrix.

The input vector for the 6-UPS is given by $\dot{q}=[\dot{d}_1,\dot{d}_2,...,\dot{d}_6]$, whereas the output vector is described by the velocity of centroid P and angular velocity of the moving platform. These terms are obtained by differentiating Eq. (3.12) with respect to time:

$$\mathrm{v}_p + \omega_B \times b_i = d_i \omega_i \times s_i + \dot{d}_i s_i, \qquad i = 1,\ldots,6 \tag{3.13}$$

where b_i and s_i denote the vector $\overline{PB}_i$ and a unit vector along $\overline{A_iB_i}$ respectively. Furthermore, ω_i denotes the angular velocity of the i^{th} limb with respect to the fixed frame R. Both sides of Eq. (3.13) are dot-multiplied by s_i in order to eliminate ω_i as follows:

$$s_i \cdot \mathbf{v}_p + (b_i \times s_i) \cdot \boldsymbol{\omega}_B = \dot{d}_i \qquad i = 1,\ldots,6 \tag{3.14}$$

when written six times (i.e. once for each limb), Eq. (3.14) yields six scalar equations, which can be assembled into matrix form as shown below:

$$\begin{bmatrix} s_1^T & (b_1 \times s_1)^T \\ s_2^T & (b_2 \times s_2)^T \\ \vdots & \vdots \\ s_6^T & (b_6 \times s_6)^T \end{bmatrix} \dot{\mathbf{X}} = I_{6\times 6}\dot{\mathbf{q}} \qquad i = 1,\ldots,6 \tag{3.15}$$

3.3. Comparison of the Performance Indices

Upon evaluating the three performance indices introduced above for the 6-UPS manipulator, the two body interfacing arrangements shown in Figure 3.3 are considered. Furthermore, each of the three joint configurations depicted in Figure 3.2 are addressed for both interfacing schemes. Further still, two major motions of the hip joint are taken into account: flexion/extension and abduction/adduction, while the third DOF of the hip joint (i.e. rotation) is assumed to be relaxed and unchanging. As can be deduced from

Figure 3.1 and Figure 3.3, the manipulator's ψ angle corresponds to flexion/extension motions for interfacing scheme *a*), while ϕ is associated with these motions in interfacing scheme *b*); for both cases, θ corresponds to abduction/adduction motions. Moreover, the workspace considered for the manipulator during these performance studies is the range of $[-0.2\ 0.2]$ radians in both flexion/extension and abduction/adduction.

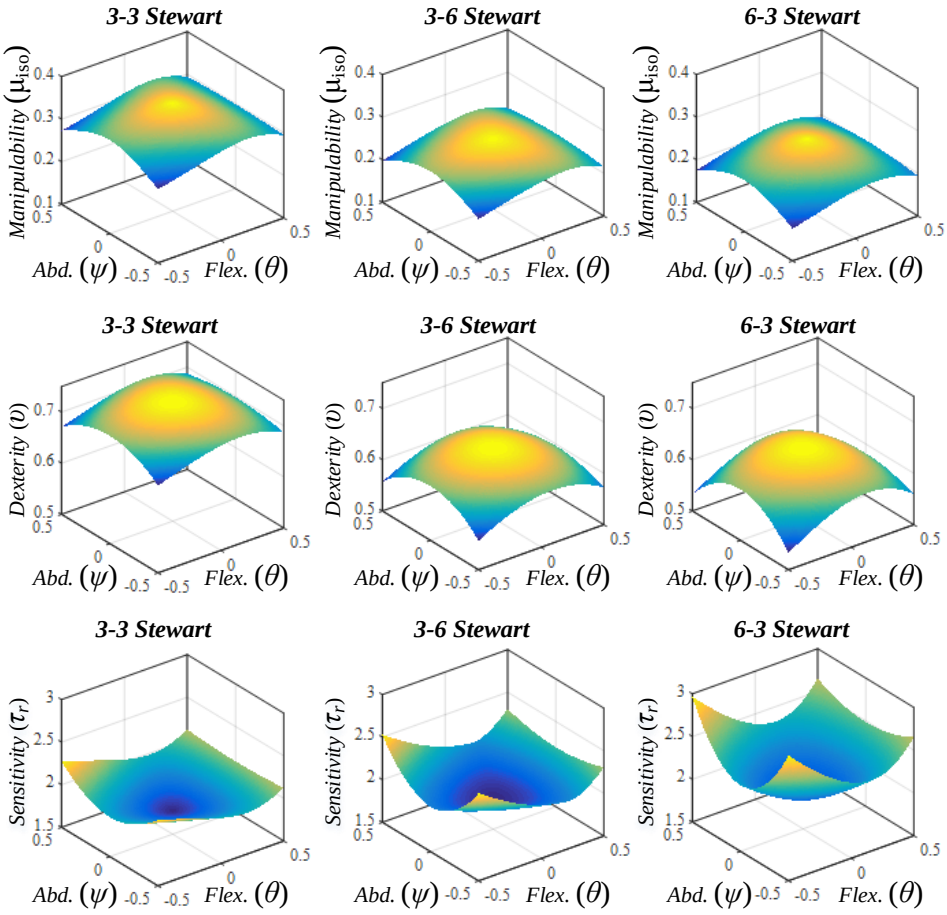

Figure 3.5. Performance analysis results for interfacing scheme 1

In addition to the study conditions described above, a number of device parameter values or ratios are assumed before specific performance results can be obtained. To start, a 6-UPS manipulator with a base radius of $r_b = 1$ and a moving platform radius of $r_m = 0.5r_b$ is considered. It is also assumed that the moving platform is initially oriented parallel to the base platform and positioned at a distance of $P_z = 0.75r_b$ from it for each study; this is considered the 'zeroed' state for the manipulator hereafter.

Given the above parameter specifications, Figure 3.5 and Figure 3.6 show the performance analysis results for both body-manipulator interfacing schemes shown in Figure 3.3. These surface plots demonstrate a general trend that greatest manipulability, greatest dexterity, and least sensitivity can be achieved at the 'zeroed' state, with each of these performance index values degrading as the manipulator moves towards the edges of its considered workspace.

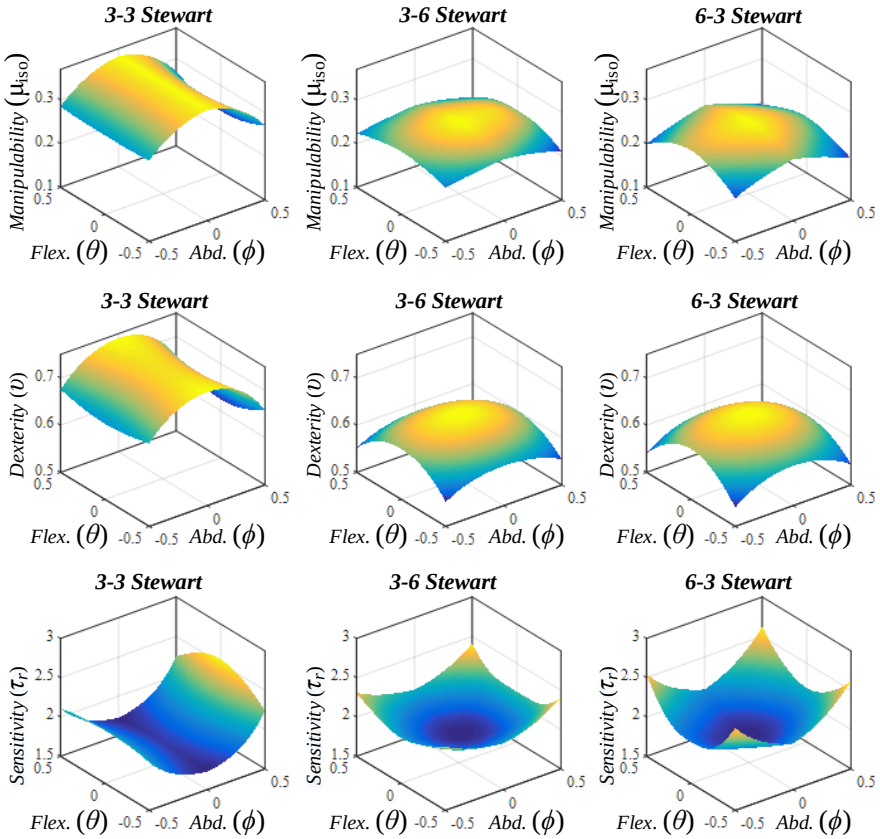

Figure 3.6. Performance analysis results for interfacing scheme 2

Comparatively, the 3-3 limb configuration for the 6-UPS device has an observably greater isotropy index for manipulability and local dexterity than the 3-6 and 6-3 configurations for both interfacing schemes; meanwhile, the 3-6 and 6-3 arrangements display relatively similar average values for both manipulability and dexterity indices. In terms of rotational sensitivity, Figure 3.5 and Figure 3.6 suggest that the 3-3 limb configuration has the smallest magnitude average, whereas 3-6 and 6-3 arrangements have similar greater magnitude averages. For interfacing scheme *a*) the 3-3 limb

configuration has the least performance deviation across the device's workspace for all indices, followed by 3-6 and then 6-3. Contrarily, when the 6-UPS is attached to the body via interfacing scheme *b*), the 3-6 limb arrangement has the least associated deviation across its workspace for each index, while the 3-3 and 6-3 structures have similar greater deviations.

3.4. Design Optimization of the 6-UPS Manipulator

The above performance index results are considered local evaluations for the 6-UPS device because they only apply when the aforementioned device parameter values and ratios are selected. To evaluate the performance of a parallel manipulator over a given workspace for a varying set of design parameters, Gosselin proposes a global performance index (GPI) in [45] as follows:

$$GPI = \frac{\int (PI)\, dW}{\int dW} \tag{3.22}$$

where PI represents any performance index of interest and W indicates the manipulator's considered workspace. Thus, the above equation provides the average value of a given performance index for all considered workspace orientations; these average values may then be evaluated for a set of device parameters as a means of comparing performance for various designs. This concept lends itself to design optimization for parallel manipulators because the average value of any performance index is an important design factor.

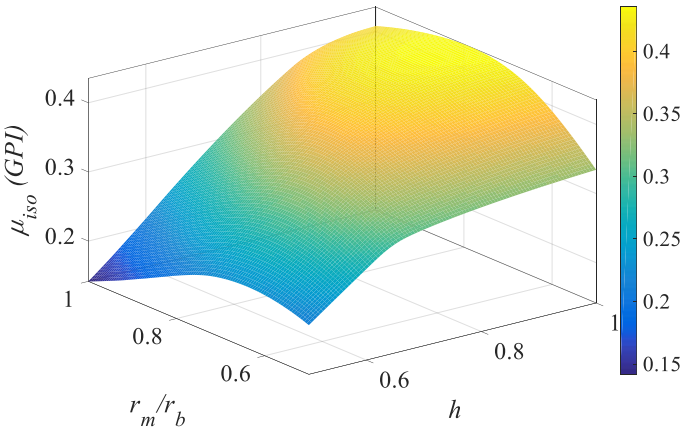

Figure 3.7. Global manipulability analysis of the 6-UPS manipulator

The design variables chosen for the optimization process are the ratio of moving platform radius to base platform radius, r_m/r_b, and the distance between the moving and base platform, h. The optimization procedure is accomplished by finding the GPI value for different combinations of height and platform radii ratio. For this study, manipulability was selected as the performance index under evaluation, and the corresponding graphical results are shown in Figure 3.7. From this surface plot, it is apparent that there is an optimal combination of r_m/r_b and h that produces maximum manipulability for the 6-UPS device; Table 3.1 summarizes the optimal selections for these parameters.

Table 3.1. Optimal Parameter Selection for 6-UPS Manipulability

Interfacing Scheme	*Equation for Optimal Value*	
a)	$r_m = 0.8r_b$	$h = r_b$
b)	$r_m = 0.8r_b$	$h = r_b$

3.5. Conclusion

This chapter proposed application of the well-established 6-UPS Stewart-Gough platform as a robotic hip within an exoskeleton system. Inverse kinematics and Jacobian development for the manipulator were revisited, which in turn enabled the analysis of three commonly-studied performance indices: manipulability, dexterity, and rotational sensitivity. These indices were explored for two possible interfacing schemes with the human hip and three different robotic limb connection arrangements.

In general, the 3-3 limb structure provided the most preferable average index values for either body interfacing scheme. However, the 3-6 arrangement generally provided the most uniform index values across the device's considered workspace. Therefore, the ideal selection of 6-UPS limb arrangement is application dependent. That is, if the application does not require an extensive workspace and is centered on the 'zeroed' state, the 3-3 configuration offers superior performance indices and would therefore likely be the preferred selection. Alternatively, if a significant workspace must be covered, the 3-6 limb arrangement may be preferable because consistency in performance across the workspace could result in ease of control.

In terms of the method for connecting the robot to the user's body, interfacing scheme *a*) is preferable in terms of performance. This is because the exoskeleton application requires a sufficiently large workspace and the performance indices associated with scheme *a*) tend to have greater uniformity across the studied workspace. After studying the 6-UPS performance for the specific parameter values and ratios considered, a global performance evaluation was conducted for manipulability. This GPI provides an indication of optimal parameter selections to achieve the greatest possible manipulability in the device. Overall, it was proposed that a 3-3 Stewart-Gough platform attached to its user via interfacing scheme *a*) and having $r_m = 0.8r_b$ and $h = r_b$ would provide the best performance for a 6-UPS-based hip exoskeleton.

Overall, the hip joints of these concepts are composed of standard Stewart-Gough platforms with alternate orientations of interface at the hip. Advantages of these hip joint designs include ease of production and expected access to knowledge in control (i.e. the control scheme for standard Stewart platforms is a well-established problem with known solutions). However, their shortcomings include lack of compactness, which in turn affects aesthetic quality, and expected limitations in range-of-motion. Ergonomic quality may also be poor if hip abduction (i.e. laterally outward rotation) results in the user's upper leg pressing against the fixed plate of the Stewart platform. Other shortcomings of utilizing this system as a hip exoskeleton is the redundant use of a manipulator which can provide 6-DOF motion in an application that only requires 3-DOF rotational motion. This would result in a bulky exoskeleton which would unnecessarily use 6 motors that would result in a greater power consumption.

Chapter 4.

Design and Kinematic Analysis of a 3-RUS/S Orientation Parallel Manipulator for Lower Extremity Exoskeleton Applications

The contribution that we convey through this chapter is centered on the design and analysis of a novel orientation parallel manipulator, named as the 3-RUS/S mechanism. The device name reflects its mechanical architecture; three robotic limbs, each containing an active rotational joint along with a passive universal joint and passive spherical joint, connect in-parallel between a base and end-effector, which is subject to a spherical joint constraint. It follows from this structure that the 3-RUS/S manipulator provides decoupled and active 3-degree-of-freedom (DOF) rotational motions to its end-effector, thus characterizing the device as an orientation parallel manipulator.

In terms of analysis, this chapter first presents a thorough discussion of a geometrically-based inverse and forward kinematics solution approach, including simulation and numerical examples for verification. Thereafter, based on the derived Jacobian matrix, the manipulability, dexterity, and rotational sensitivity performance indices for the device are evaluated for roll-pitch and roll-yaw motion combinations. A global conditioning index is then developed as a means of optimizing the design in terms of manipulability. Next, an orientation workspace analysis is conducted and torque, speed, and power requirements are predicted via simulation for one target application of the mechanism. Finally, experimental results are obtained from a prototype device to validate its motion-tracking capabilities within the context of the primary target application.

A particularly challenging aspect of exoskeleton design arises when the human joint targeted for guidance is capable of three rotational degrees-of-freedom (DOFs).

Considering the hip joint, a majority of relevant exoskeleton designs explored in academia do not offer active guidance for all three major joint rotations, instead providing passive freedom to one or two DOFs or restricting them altogether [19–24].

In order to provide complete, decoupled kinematic relation with the three major DOFs of the human hip, a mechanism capable of independent and active 3-DOF rotational motions should be employed. A number of such mechanisms have previously been designed and extensively analyzed. In what follows, ‘R’ indicates a rotary joint, ‘U’ a universal joint, ‘S’ a spherical joint, and ‘P’ a prismatic joint; any underlined letter indicating that the corresponding joint is active, and ‘/S’ indicates that a spherical joint constraint exists on the end-effector.

In [48], Gosselin and Lavoie discuss the kinematic design of several spherical parallel manipulators, including a generalized 3-U<u>P</u>S/S design and three different embodiments for 3-<u>R</u>RR mechanisms. Gosselin and St-Pierre then detailed the mechanical design and dynamic performance of one such 3-<u>R</u>RR spherical 3-DOF parallel manipulator, which they named the agile eye, in [49]. In more recent times, [50] has discussed robust forward-displacement analysis applicable to two 3-<u>R</u>RR and 3-U<u>P</u>U/S mechanisms, [51] revisits the kinematics and discusses motion control of 3-<u>R</u>RR and 3-U<u>P</u>S/S devices, and [52] provides a method for obtaining unique kinematic solutions of a 3-<u>R</u>RR spherical parallel manipulator. In addition to these well-established devices, a number of other parallel mechanisms that achieve 3-DOF spherical motion at their end-effectors have been explored. Reference [53] discusses various kinematic properties of a 3-<u>R</u>RRS+S spherical parallel manipulator primarily through application of screw theory. In [54], Cui et al. present the design, kinematic analysis, performance analysis, and optimization for a redundantly-actuated 4-U<u>P</u>S/S spherical parallel manipulator with solar panel positioning applications. Reference [55] provides a kinematic analysis, performance analysis, and simulation for a redundantly-actuated 3-<u>R</u>US/<u>R</u>RR spherical parallel manipulator. Most recently, Enferadi and Shahi have presented a design, kinematic analysis, and workspace optimization for a novel 3-<u>R</u>SS/S spherical parallel manipulator [56].

Although the ultimate goal is to develop a hip exoskeleton, this study explores a novel mechanism capable of active 3-DOF rotational motions in isolation from any components that would transmit these motions to the human upper leg. Specifically, this chapter details the proposed design, kinematic analysis, performance indices, and

recommended implementation of one possible solution: a 3-RUS/S parallel manipulator. Additionally, experimental results obtained from a prototype device during a gait motion tracking study are presented.

4.1. Mechanical Design of the 3-RUS/S Device

Manipulators allowing three rotations about one point represent an interesting alternative to the wrist with three revolute joints having convergent axes classically used for serial robots [36]. One possible method for generating rotary motion about one point is constituted of a central mast, linked to the base and possessing at its top a spherical ball joint on which the moving plate is articulated. Figure 4.1 shows three wrist mechanisms using the central mast principle.

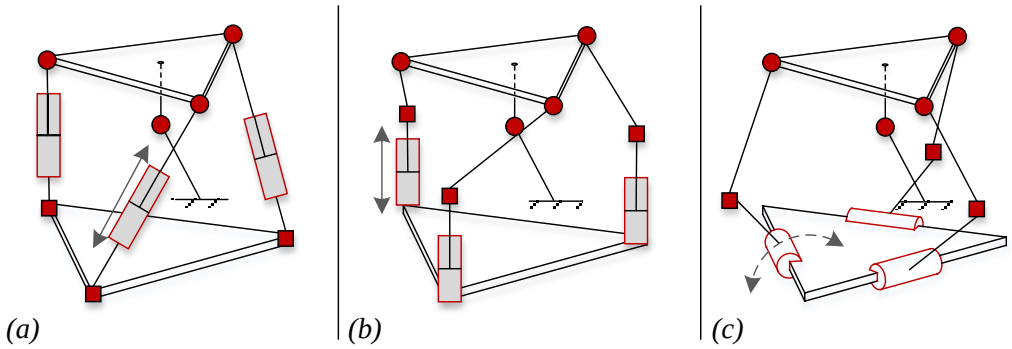

Figure 4.1. Three different embodiments of central mast mechanism a) 3-UPS/S b) 3-PUS/S and c) 3-RUS/S mechanism

In the first case (UPS), the actuator allows the modification of the chain length. For manipulator with (PUS), a prismatic actuator moves the center of a universal joint on which a fixed length link is articulated. For the RUS chain, a motor (i.e. revolute joint) rotates a lever, at the end of which is a universal joint connected to a fixed length link which is connected to the moving platform using a spherical ball joint.

Although other embodiments are possible, the 3-RUS/S device considered in this study consists of four part categories as shown in Figure 4.2. A ring structure acts as a base platform, providing the device with a rigid connection to the ground reference frame. Three limb structures connect the outer base platform to a central end-effector, or moving platform, which takes the form of a hemispherical shell. Each limb is composed of two links connected to each other through a universal joint. Furthermore, each distal

link connects to the outer base platform via a 1-DOF rotational joint, and each proximal link connects to the central moving platform via a 3-DOF spherical joint. Finally, the central moving platform is constrained to 3-DOF rotational motion through its interface with a ground-connected spherical joint. One important design feature of this device is that the rotational axes for each of the three 1-DOF joints attached to the base platform and the center of rotation for the spherical joint constraining the moving platform's motions all exist within a common plane.

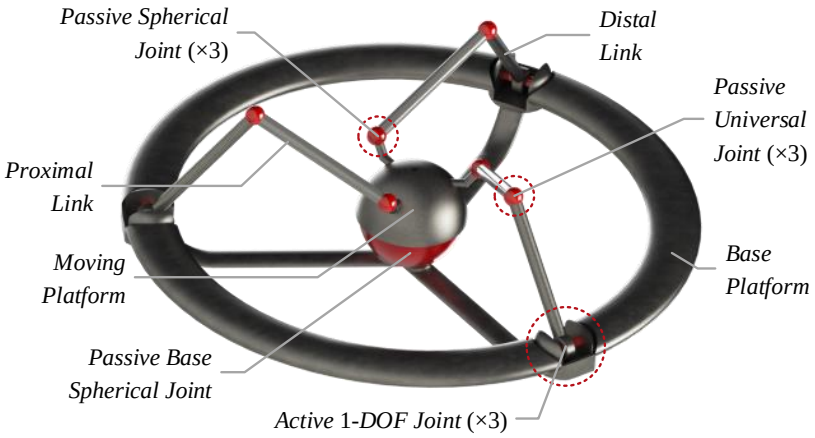

Figure 4.2. Simplified mechanical design of the 3-RUS/S device

The name of the device reflects its structural design: the outer base platform, distal link, proximal link, and central moving platform are respectively connected by way of rotational (R), universal (U), and spherical (S) joints. The leading '3' indicates the parallel connection of base platform and moving platform by three limbs, and the lattermost 'S' signifies the spherical constraint on the moving platform. The underline identifies the 1-DOF rotational joint as the only active joint, while the forward slash distinguishes the final spherical joint as a constraint on the moving platform as opposed to a second spherical joint on each limb.

4.2. Kinematic Analysis of the 3-RUS/S Device

The kinematic analysis presented below outlines forward and inverse kinematics procedures for the 3-RUS/S parallel manipulator, along with the system of reference frames used to facilitate their derivations.

4.2.1. Notation for Reference Frames, Joints and Motions

As shown in the geometrical schematic of Figure 4.3, the global frame origin (O) for the device is coincident with the moving platform's center of rotation. Moreover, the global z-axis is coaxial with the ring-shaped base platform's central axis, and the global x-axis intersects with the rotational axis of one active rotary joint. The limb associated with this joint is denoted with the number 1, while the adjacent limb attached counter clockwise with respect to the positive global z-axis is denoted with 2, and the final limb with 3. The positions of the 1-DOF, universal, and spherical joints for each limb are respectively designated by $\mathbf{a}_i$, $\mathbf{b}_i$, and $\mathbf{c}_i$ vectors, where the subscript i differentiates the three limbs (i.e. $i = 1, 2, 3$).

The device's 'home' configuration is achieved when all universal joint positions $\mathbf{b}_i$ share a common positive z-coordinate value in terms of the global frame; similarly, all three spherical joints at $\mathbf{c}_i$ share a common positive global z-coordinate value in this state. As a consequence of the 'home' configuration, the device displays rotational symmetry in the global x–y plane, and the moving platform is positioned within the subspace defined by the positive global z-axis. Hereafter, a '0' subscript will be used to identify the global frame or any of its individual axes, while a '0' superscript associated with a vector indicates representation in the global reference frame.

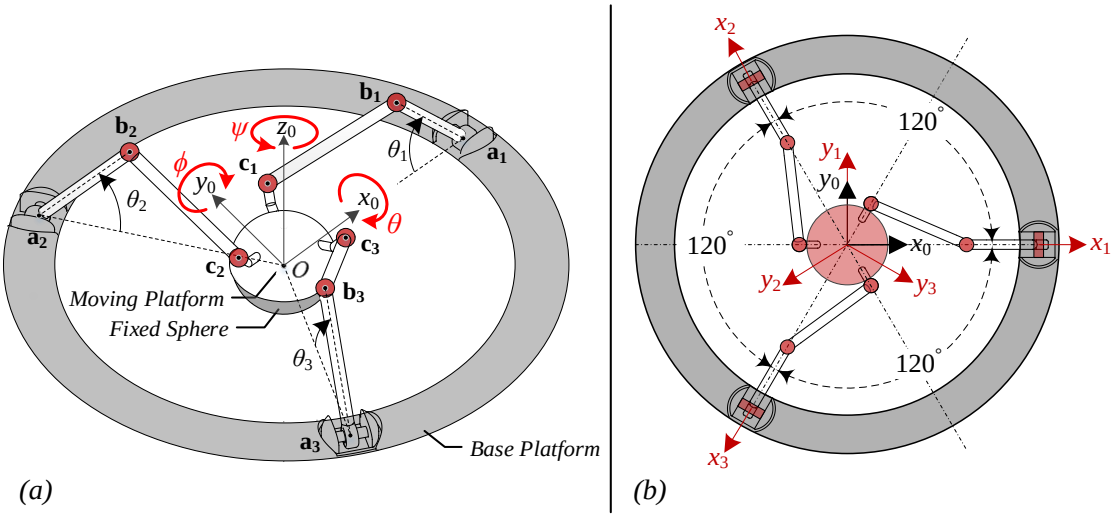

Figure 4.3. a) Isometric view and b) top view of the proposed 3-RUS/S

In addition to the global frame defined above, a set of four local frames will be used in the kinematic analysis to follow. The first three of these four frames specify the directions within the x_0–y_0 plane that the active 1-DOF joints are located, as shown in Figure 3.3. For the sake of consistency, these three local frames, F_1, F_2, and F_3, are denoted with subscripts that match the joint that they identify. Specifically, $\mathbf{a}_i$ lies on the x_i-axis, while the z_i-axis is coaxial with the z_0-axis. Frames F_1, F_2, and F_3 must be respectively defined by fixed rotations of $0°$, $120°$, and $240°$ about the positive z_0-axis because it has been previously established that positions $\mathbf{a}_i$ have rotationally symmetric spacing in the x_0–y_0 plane and that $\mathbf{a}_1$ lies on the x_0-axis. Therefore, pre-multiplication by one of the following matrices, R_{0i} will transform a vector's representation from F_i local-frame representation to global-frame representation. Alternatively, pre-multiplication by R_{i0} will allow globally-defined positions to be expressed in the corresponding local frame. In the equations below, C and S are abbreviations for the cosine and sine functions respectively.

$$R_{01}=\begin{bmatrix}1&0&0\\0&1&0\\0&0&1\end{bmatrix},R_{02}=\begin{bmatrix}C(2\pi/3)&-S(2\pi/3)&0\\S(2\pi/3)&C(2\pi/3)&0\\0&0&1\end{bmatrix},R_{03}=\begin{bmatrix}C(4\pi/3)&-S(4\pi/3)&0\\S(4\pi/3)&C(4\pi/3)&0\\0&0&1\end{bmatrix} \quad (4.1)$$

$$R_{01}=\begin{bmatrix}1&0&0\\0&1&0\\0&0&1\end{bmatrix},R_{02}=\begin{bmatrix}C(2\pi/3)&-S(2\pi/3)&0\\S(2\pi/3)&C(2\pi/3)&0\\0&0&1\end{bmatrix},R_{03}=\begin{bmatrix}C(4\pi/3)&-S(4\pi/3)&0\\S(4\pi/3)&C(4\pi/3)&0\\0&0&1\end{bmatrix} \quad (4.2)$$

Not shown in Figure 3.3, the fourth local frame, F_4, is used to specify rotations of the moving platform with respect to the global frame. The moving platform's spatial orientation is uniquely defined by a series of fixed-frame rotations about the global x, y, and z axes, quantified by θ, ϕ, and ψ respectively as illustrated in Figure 4.3. It follows that the transformation matrix shown in Eq. (4.3) converts a vector's representation from within frame F_4 to that within F_0 when pre-multiplied by it.

$$R_{04} = \begin{bmatrix} C\psi C\phi & C\psi S\phi S\theta - S\psi C\theta & C\psi S\phi C\theta + S\psi S\theta \\ S\psi C\phi & S\psi S\phi S\theta + C\psi C\theta & S\psi S\phi C\theta - C\psi S\theta \\ -S\phi & C\phi S\theta & C\phi C\theta \end{bmatrix} \tag{4.3}$$

Finally, note that the active joints' angular states are given by θ_i for $i = 1, 2, 3$, where the subscript identifies the limb to which the active joint belongs.

4.2.2. Inverse Kinematics

In the context of this study and in general, the inverse kinematics procedure provides the solutions to the problem of determining the active joint states required to achieve a desired end-effector state [57]. As implied by the schematic diagram shown in Figure 4.3 and mentioned above, the 3-RUS/S parallel manipulator's end-effector state is fully defined by three orthogonal, fixed-frame rotations: θ, ϕ, and ψ. All possible combinations of these rotations within the moving platform's practical workspace are enabled by a corresponding set of angular input states at the device's active 1-DOF joints attached to the base platform. The following subsections detail one method for deriving the relationship between desired end-effector orientation and active joint angular states.

- *Equations for Spherical Joint Positions* $\mathbf{c}_i$. The inverse kinematics approach used in this study is to first find expressions for the positions of each joint that correspond to a desired end-effector orientation, and then use that joint position information to deduce the required active joint states. Therefore, the inverse kinematics process first requires expression of the joint positions for each limb: $\mathbf{a}_i$, $\mathbf{b}_i$, and $\mathbf{c}_i$.

Beginning with the lattermost, we can observe from Figures 4.1–4.3 that all joints located at $\mathbf{c}_i$ have fixed positions with respect to the local frame attached to the end-effector: F_4. It follows that the first step in this analysis is to express the positions of points $\mathbf{c}_i$ in the

global frame after any arbitrary rotations of the end-effector. This is achieved through pre-multiplication of the known local position vector $\mathbf{c}_i$ by the R_{04} rotation matrix defined in Eq. (4.3) as follows:

$$\vec{c}_i^{\,0} = R_{04}\vec{c}_i^{\,4} \tag{4.4}$$

where superscript '4' designates vector representation with respect to end-effector frame F_4. In general, an 'i' superscript attached to a vector indicates that the vector's coordinates are given with respect to the i^{th} frame. Note that the desired end-effector orientation is specified within the rotation matrix R_{04}.

- Equations for Rotary Joint Positions $\mathbf{a}_i$**.** In addition to the newly defined $\mathbf{c}_i$ positions with respect to the global frame, the global positions of points $\mathbf{a}_i$ are also known because they are fixed along the ring-shaped base platform as shown in Figure 4.3. However, for the sake of generality across each limb, the remainder of derivations for the inverse kinematics process will occur with respect to the three local frames with x-axes respectively pointing to each active joint on the base platform. Therefore, points $\mathbf{a}_i$ and $\mathbf{c}_i$ will be redefined in their corresponding generalized local frame as follows:

$$\vec{c}_i^{\,i} = R_{i0}\vec{c}_i^{\,0} \qquad \textit{and} \qquad \vec{a}_i^{\,i} = R_{i0}\vec{a}_i^{\,0} \tag{4.5}$$

where superscript i denotes representation in the i^{th} local frame, and rotation matrices R_{i0} are defined for $i = 1$, 2, and 3 in Eq. (4.2).

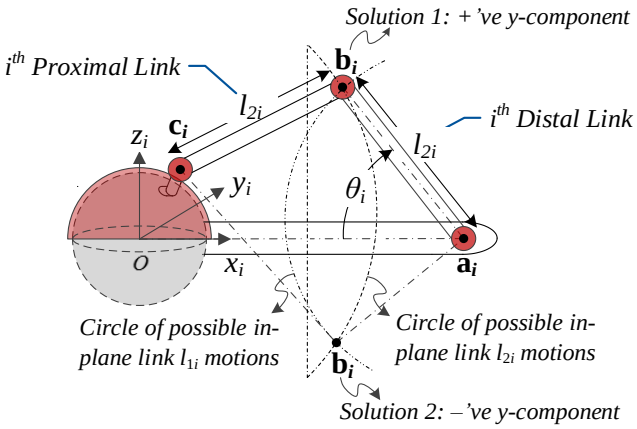

Figure 4.4. Simplified view of the 3-RUS/S device in the x_i–z_i plane

- Equations for Universal Joint Positions $\mathbf{b}_i$. In order to complete the inverse kinematics process, the positions $\mathbf{b}_i$ of each universal joint on the limbs must be determined. To begin, equations for the known lengths of the serial chain links must be

developed. Letting l_{1i} and l_{2i} respectively represent the lengths of the distal and proximal links of each serial chain, as shown Figure 4.4, the following equations can be used to relate these lengths to joint position coordinates. Note that x_{ji} corresponds to the x-coordinate of the position for joint j on limb i, and likewise for the y and z coordinates. These coordinates may be expressed in any frame as long as one frame is used consistently.

$$L_{1i} = \sqrt{\left(x_{bi} - x_{ai}\right)^2 + \left(y_{bi} - y_{ai}\right)^2 + \left(z_{bi} - z_{ai}\right)^2} \tag{4.6}$$

$$L_{2i} = \sqrt{\left(x_{bi} - x_{ci}\right)^2 + \left(y_{bi} - y_{ci}\right)^2 + \left(z_{bi} - z_{ci}\right)^2} \tag{4.7}$$

Recall from the discussion above that frames F_1, F_2, and F_3 are defined such that the y-components of vectors $\mathbf{a}_i$ and $\mathbf{b}_i$ are both equal to zero. That is, vectors $\mathbf{a}_i$ and $\mathbf{b}_i$ lie within the x_i–z_i plane when represented in the i^{th} frame. It follows that Eqs. (4.6) and (4.7) can be simplified as shown in the next two equations.

$$L_{1i}^2 = x_{bi}^2 - 2x_{bi}x_{ai} + x_{ai}^2 + z_{bi}^2 - 2z_{bi}z_{ai} + z_{ai}^2 \tag{4.8}$$

$$L_{2i}^2 = x_{bi}^2 - 2x_{bi}x_{ci} + x_{ci}^2 + z_{bi}^2 - 2z_{bi}z_{ci} + z_{ci}^2 + y_{ci}^2 \tag{4.9}$$

Conceptually, the next steps towards defining $\mathbf{b}_i$ in terms of the known coordinates of $\mathbf{a}_i$ and $\mathbf{c}_i$ begins with the projection of the spherical shell tracing possible rotations for inner link l_{2i} about the 3-DOF joint at $\mathbf{c}_i$ onto the x_i-z_i plane of frame F_i. This process creates a circle centered on the projection of point $\mathbf{c}_i$ in this x_i-z_i plane. Furthermore, the circle within this plane defined by the possible rotations of outer link l_{1i} about the 1-DOF joint at $\mathbf{a}_i$ must be considered. Figure 4.4 shows segments of these circles in the x_i-z_i plane. Assuming that the inner and outer links are not collinearly oriented, the two circles will intersect at two points. These two points provide the possible locations of $\mathbf{b}_i$ when the end-effector's rotations place the inner 3-DOF joint at location $\mathbf{c}_i$. However, the practical workspace for the mechanism will ensure that only the $\mathbf{b}_i$ position with greater z_i coordinate value is feasible.

The mathematical process that achieves the conceptual process above begins by isolating for the term $\left(x_{bi}^2 + z_{bi}^2\right)$ in Eq. (4.8) and then substituting the result into Eq. (4.9). This yields Eq. (4.10).

$$L_{2i}^2 = L_{1i}^2 + 2x_{bi}x_{ai} - x_{ai}^2 + 2z_{bi}z_{ai} - z_{ai}^2 - 2x_{bi}x_{ci} + x_{ci}^2 - 2z_{bi}z_{ci} + z_{ci}^2 + y_{ci}^2 \tag{4.10}$$

Eq. (4.10) is representative of the line through the two intersection points of the aforementioned circles. Now, isolating for x_{bi} in Eq. (4.10) and substituting the result back into Eq. (4.9) provides an expression for the two theoretically possible z_{bi} values. Applying the quadratic equation and ignoring the infeasible negative result, the required z_{bi} coordinate is found:

$$z_{bi} = \frac{-E \pm \sqrt{E^2 - 4DF}}{2D} \tag{4.11}$$

where the variables introduced in the equation above are given by the following expressions:

$$D = \frac{C^2}{B^2} + 1, \qquad \mathrm{E} = \frac{2CA}{B^2} - \frac{2Cx_{ai}}{B} - 2z_{ai}, \qquad F = \frac{A^2}{B^2} - \frac{2Ax_{ai}}{B} + x_{ai}^2 + z_{ai}^2 - L_{1i}^2 \tag{4.12}$$

Furthermore, the variables A, B, and C appearing in Eqs. (4.12) are defined below, where all other variables represent known dimensional parameters of the mechanism.

$$A = y_{ci}^2 + L_{1i}^2 - x_{ai}^2 - z_{ai}^2 + x_{ci}^2 + z_{ci}^2 - L_{2i}^2 \quad , B = 2\left(x_{ci} - x_{ai}\right) \quad , C = 2\left(z_{ci} - z_{ai}\right) \tag{4.13}$$

***- Inverse Kinematics Equation*.** Having determined the z_i-coordinate of point $\mathbf{b}_i$, the remaining coordinates can readily be determined through substitution into either Eq. (4.6) or (4.7); recall that when defined with respect to frame F_i, the y_i-coordinate of $\mathbf{b}_i$ is known to be zero. However, the angle θ_{1i} to be actuated by the active 1-DOF joint on each limb only requires specification of coordinate z_{bi}, as given below.

$$\theta_{1i} = \sin^{-1}\left(\frac{Z_{bi} - Z_{ai}}{L_{1i}}\right) \tag{4.14}$$

The limited range of -90° to +90° associated with the arcsine function is not of concern here because the device would be physically broken before either of these limits could be attained; also recall that the limitation on z_{bi} from being any negative value prevents motion in the range [-90°, 0). Thus, within its practical workspace, Eq. (4.14) provides the inverse kinematic solution for the 3-RUS/S parallel manipulator device where z_{ai} and L_{1i} are constants defined by the device geometry and Eqs. (4.11–4.13) provide a means for determining the value of z_{bi}.

4.2.3. Forward Kinematics

Forward kinematics analysis develops a mathematical relationship between the active joint and moving platform configurations when the former is known and the latter is to be determined [36]. Considering the 3-RUS/S forward kinematics problem, distal link angles θ_1, θ_2, and θ_3 are assumed to be known inputs, while moving platform orientation angles θ, ϕ, and ψ are unknown and must be resolved. Although several approaches may be used to complete the forward kinematics analysis of this device, the method conducted in this study is geometrically-based as outlined in the following subsections.

- Determination of $^i\mathbf{b}_i$**.** When considered locally, each universal joint position vector $\mathbf{b}_i$ can be expressed in terms of its associated active joint using one general equation:

$$^i\mathbf{b}_i = \left[\left[\|a_i\| - L_{1i}\cos(\theta_i)\right] \quad 0 \quad L_{1i}\sin(\theta_i)\right], \qquad i = 1,2,3 \tag{4.15}$$

where the three local frames in question are defined in Figure 4.3. In order to represent these vectors in the global frame, each must be pre-multiplied by the appropriate rotation matrix of Eq. (4.1) as follows.

$$^0\mathbf{b}_i = R_{0i}\,{}^i\mathbf{b}_i \tag{4.16}$$

- Determination of $^0\mathbf{c}_i$**.** The next task is to determine the global positions of the spherical joint connecting the moving platform to the proximal link of each limb. When the geometrical constraint imposed by each proximal link's fixed length is considered in isolation, the set of possible $\mathbf{c}_i$ positions is defined by a spherical surface of radius l_{2i} centered at $\mathbf{b}_i$ for each $i = 1, 2, 3$. Alternatively, when the geometrical constraints arising from the spherical joints' fixed positions on the moving platform and the moving platform's spherical joint connection to the ground frame are considered in the absence of other constraints, the set of possible $\mathbf{c}_i$ positions is defined by a spherical surface of radius $\|\mathbf{c}_i\|$ centered at the global origin for each $i = 1, 2, 3$.

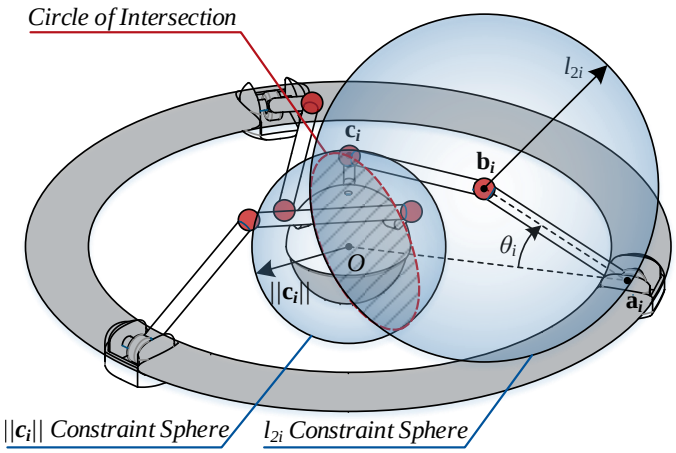

Figure 4.5. Circle defining the possible spherical joint positions for one limb after imposing l_{2i} and $||c_i||$ geometrical constraints

Upon asserting each of these constraints simultaneously, the set of possible $\mathbf{c}_i$ positions reduces to a circle for each i, assuming that each of the three spheres centered at the $\mathbf{b}_i$ points have a nonzero volume of intersection with the sphere centered at the global origin. An illustrative example of the possible solution space for $\mathbf{c}_i$ after imposing the geometrical constraints discussed thus far is shown in Figure 4.5 for one limb of the 3-RUS/S device.

The final geometrical constraint imposed by the mechanical design of the 3-RUS/S on its spherical joints located at $\mathbf{c}_i$ is the known distance between each other. Upon asserting that each point $\mathbf{c}_i$ is located at a fixed distance from each adjacent $\mathbf{c}_j$ point, where i and $j = 1, 2, 3$ but $i \neq j$, the set of possible solutions for each $\mathbf{c}_i$ position reduces to one or more points, assuming input angles θ_1, θ_2, and θ_3 correspond to a configuration within the device's reachable workspace. Depending on the active joints' angular states and the relative geometrical dimensions chosen for the device's components, some input angles may result in several mathematically feasible solutions for the $\mathbf{c}_i$ positions while others may result in one feasible solution as illustrated in Figure 4.6.

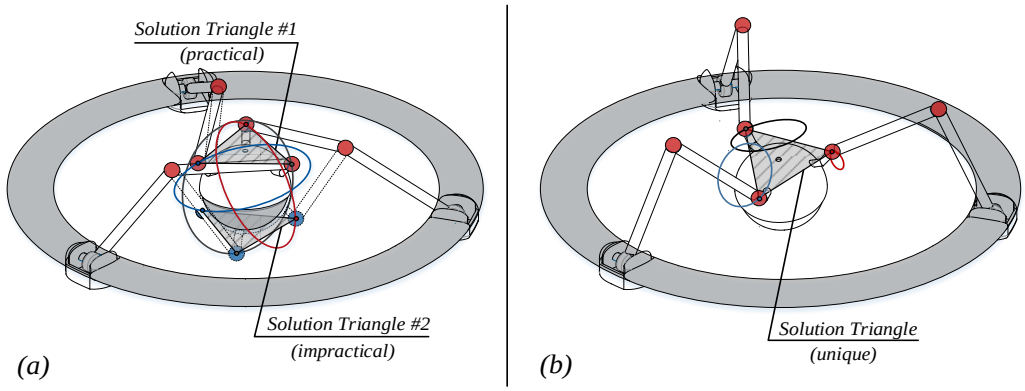

Figure 4.6. Example solutions for c_i points after l_{1i}, l_{2i}, $\|c_i\|$, and $\|c_i - c_j\|$ geometrical constraints asserted

In the case of multiple solutions, only one will exist within the device's physical allowable workspace where the linkages do not interfere one another. In case (a) of the two manipulator orientations shown in Figure 4.6, a number of mathematically feasible solutions exist: the two that are shown (i.e. both configurations that result in z_0 and z_4 axes being coaxial) along with four that would result in the z_4-axis lying in the x_0–y_0 plane, which are not shown for the sake of visual clarity. This multiplicity of mathematically-possible solutions is the result of the three constraint circles having a highly symmetric organization in space. However, there is only one feasible solution, as labeled in Figure 4.6, because all other solutions would result in mechanical interference on the physical mechanism. Meanwhile, it is readily apparent that only one solution exists for case (b) in Figure 4.6 such that each geometrical constraint is satisfied. Ultimately, upon asserting the known distance between each $\mathbf{c}_i$ point in addition to the previously discussed constraints, a unique solution set for those $\mathbf{c}_i$ points within the global frame is achieved as long as the input angles correspond to a reachable configuration within the device's workspace.

- Determination of Moving Platform Orientation. The final task in the forward kinematics process is to determine the three rotations associated with the moving platform's orientation. As discussed in Section 4.2.1, the $\mathbf{c}_i$ points are vectors of constant value in terms of the F_4 reference frame, which tracks motions of the moving platform. Furthermore, coordinate values of the $\mathbf{c}_i$ points with respect to the global frame have been found as per the process in Section 4.2.1. Therefore, Eq. (4.4) provides nine nonlinear equations in which θ, ϕ, and ψ are the only unknowns. A numerical method may then be used to determine the values of these three unknowns and thereby

complete the forward kinematics procedure. Further details on how this task may be implemented are presented in the next section.

4.3. Simulation-Based Verification of Kinematic Analysis

In order to confirm that the inverse and forward kinematic analyses completed above are correct, algorithms based on the developments of Sections 4.2.2 and 4.2.3 were produced, numerical examples were evaluated, and the results were compared to simulations in which a CAD model of the 3-RUS/S device underwent the same treatments as was assumed for the examples. The simulations required to complete this task were conducted using a synthesis of SolidWorks, Simulink, and SimMechanics software. A listing of device parameters used in this study is provided in Table 4.1 below. With this parameter set, each θ_i has a value of $51.1137°$ when the device is in its 'home' configuration.

Table 4.1. Device parameters used for simulations and numeric examples

Parameter (i.e. for $i, j = 1, 2, 3$)	**Value**
Distal Link Length, L_{1i}	120 mm
Proximal Link Length, L_{2i}	120 mm
Base Platform Radius, $r_b = \|\|\mathbf{a}_i\|\|$	200 mm
Moving Platform Radius, r_m	50 mm
3-DOF Joint Local Height, h	42.5 mm
3-DOF Joint Connection Radius, $\|\|\mathbf{c}_i\|\|$	65.6220 mm
3-DOF Joint Separation Distance, $\|\|\mathbf{c}_i - \mathbf{c}_j\|\|$ $(i \neq j)$	86.6025 mm

4.3.1. Inverse Kinematics Algorithm Validation

Developing an inverse kinematics algorithm producing θ_i joint angles as functions of θ, ϕ, and ψ for the 3-RUS/S device is straightforward, because the equations provided in Section 4.2 fully describe the required computational process. In order to complete the algorithm validation, a SolidWorks CAD model of the device was prepared, as shown in Figure 4.2, and then converted the files for use in the Simulink environment via the SimMechanics software package. Next, the simulated moving platform orientation was directly commanded by providing angular position signals to each DOF of the virtual spherical joint. Meanwhile, virtual scope sensors monitored the simulated angular states of the 1-DOF joints attached to the device's base platform. Upon providing the inverse kinematics algorithm with the same time-varying signals for θ, ϕ, and ψ as was used in

the simulation, given in Eqs. (4.17), the results shown in Figure 4.7 were obtained. The high level of observable agreement between the algorithm and simulation output signals suggests that the results are equal within the limits of computational errors, thus confirming the correctness of the inverse kinematics procedure documented in this study.

$$\theta = 0.2\sin(5t), \phi = 0.25\sin(4t + \pi/6), \psi = 0.3\sin(3t + \pi/3) \tag{4.17}$$

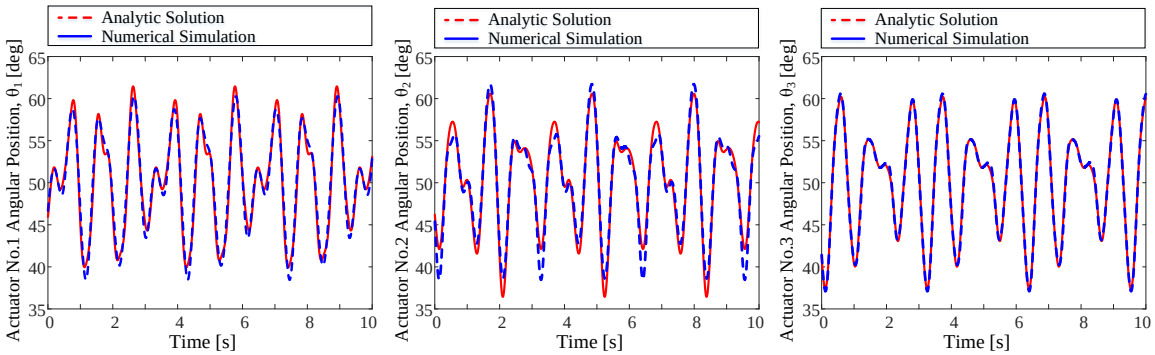

Figure 4.7. plots of θ_i angles vs. time produced by analytical inverse kinematics algorithm and CAD model simulation

4.3.2. Forward Kinematics Algorithm Validation

Being more complex and computationally expensive than the inverse kinematics algorithm, the forward kinematics algorithm was verified using a series of single-orientation examples instead of signals. Considering a first example set of θ_i angles as follows, the forward kinematics process begins with the computation of local $\mathbf{b_i}$ points.

$$\theta_1 = 30^\circ, \theta_2 = 30^\circ, \theta_3 = 30^\circ \tag{4.18}$$

Substituting the appropriate device parameters and example input angles into Eq. (4.15), the three ${}^i\mathbf{b_i}$ points are calculated as given below:

$$\begin{aligned} {}^1\mathbf{b}_1 &= \begin{bmatrix} 96.077 & 0 & 60 \end{bmatrix} \text{mm}, \\ {}^2\mathbf{b}_2 &= \begin{bmatrix} 96.077 & 0 & 60 \end{bmatrix} \text{mm}, \\ {}^3\mathbf{b}_3 &= \begin{bmatrix} 96.077 & 0 & 60 \end{bmatrix} \text{mm}. \end{aligned} \tag{4.19}$$

As expected from the generalized local frame definitions, each ${}^i\mathbf{b_i}$ point has the same coordinate set because each input angle θ_i is equal. Next, the local $\mathbf{b_i}$ points are converted to their global representations as per Eq. (4.16):

$$
\begin{aligned}
{}^0\mathbf{b}_1 &= \begin{bmatrix} 96.077 & 0 & 60 \end{bmatrix} \text{mm}, \\
{}^0\mathbf{b}_2 &= \begin{bmatrix} -48.0385 & 83.2051 & 60 \end{bmatrix} \text{mm}, \\
{}^0\mathbf{b}_3 &= \begin{bmatrix} -48.0385 & -83.2051 & 60 \end{bmatrix} \text{mm}.
\end{aligned} \tag{4.20}
$$

A numerical method was then used to determine the circles of intersection between l_{2i} and $\|\mathbf{c}_i\|$ constraint spheres for $i = 1, 2, 3$. Similarly, the set of points satisfying the $\|\mathbf{c}_i - \mathbf{c}_j\|$ constraint were found by a numerical approximation method. To eliminate solutions that would result in impractical device configurations, ${}^0\mathbf{c}_i$ points with negative z-coordinates were rejected. This provided that following proximal joint position solution set.

$$
\begin{aligned}
{}^0\mathbf{c}_1 &= \begin{bmatrix} -12.2973 & 48.4642 & 42.5 \end{bmatrix} \text{mm}, \\
{}^0\mathbf{c}_2 &= \begin{bmatrix} -35.8226 & -34.8818 & 42.5 \end{bmatrix} \text{mm}, \\
{}^0\mathbf{c}_3 &= \begin{bmatrix} 48.1199 & -83.2051 & 42.5 \end{bmatrix} \text{mm}.
\end{aligned} \tag{4.21}
$$

With the above values determined, it is now possible to apply the relationship given in Eq. (4.4). First, treating the elements of the R_{04} matrix as simple variables to be solved, the nine equations described by Eq. (4.4) become a linear set with nine unknowns. Completing this procedure for the example in question populates the R_{04} matrix as follows.

$$
R_{04} = \begin{bmatrix} r_{11} & r_{12} & r_{13} \\ r_{21} & r_{22} & r_{23} \\ r_{31} & r_{32} & r_{33} \end{bmatrix} = \begin{bmatrix} 0.9264 & 0.2640 & -0.2685 \\ -0.2140 & 0.9588 & 0.2015 \\ 0.3098 & -0.1292 & 0.9420 \end{bmatrix} \tag{4.22}
$$

Finally, a unique solution set for the θ, ϕ, and ψ angles defining the moving platform's orientation can be obtained from the values above by considering the definition of R_{04} as per Eq. (4.3). There are a number of possible methods that may be used to complete this procedure, but methods that incorporate at least two values from each column of R_{04} or all three values from two columns of the matrix are superior to methods that use less orientation information. Given that the columns of the R_{04} must be a right-handed orthonormal set of vectors, the former methods ensure that enough data to fully define the moving platform's spatial orientation is utilized in the computation of its θ, ϕ, and ψ angles. Contrarily, methods that use less information than is necessary to fully define a three dimensional orientation, although mathematically feasible, may produce errors for certain configurations; one common issue arising for these methods is the 0/0

indeterminate form. For these reasons, θ, ϕ, and ψ as follows were chosen to be computed as follows.

$$\theta = \text{atan2}\left(r_{13}r_{21} - r_{11}r_{23}, r_{11}r_{22} - r_{12}r_{21}\right) = 0^{\circ} \tag{4.23}$$

$$\phi = \text{atan2}\left(r_{22}r_{13} - r_{12}r_{23}, (r_{11}r_{22} - r_{12}r_{21}) / \cos(\theta)\right) = 0^{\circ} \tag{4.24}$$

$$\psi = \text{atan2}\left(r_{13}r_{32} - r_{12}r_{33}, r_{23}r_{33} - r_{23}r_{32}\right) = 44.237^{\circ} \tag{4.25}$$

Intuitively, it can be expected that any equal θ_i input values will produce pure rotations about the z_0-axis for the moving platform. Employing the same approach as was undertaken for the example detailed above, two more numerical examples for the forward kinematics algorithm were completed, as summarized in Table 4.2. The results of each example, including those of the first, were verified using the inverse kinematics algorithm discussed earlier.

Table 4.2. Numeric example summary for the forward kinematics algorithm

Example No.2: θ_1 = 60°, θ_2 = 65°, θ_3 = 58°		**Example No.3:** θ_1 = 50°, θ_2 = 55°, θ_3 = 60°	
$^{1}\mathbf{b}_1$ = [140, 0, 103.92]	$^{0}\mathbf{b}_1$ = [140, 0, 103.9]	$^{1}\mathbf{b}_1$ = [122.8, 0, 91.9]	$^{0}\mathbf{b}_1$ = [122.8, 0, 91.9]
$^{2}\mathbf{b}_2$ = [149.2, 0, 108.7]	$^{0}\mathbf{b}_2$ = [-74.6, 129.2, 108.7]	$^{2}\mathbf{b}_2$ = [131.1, 0, 98.2]	$^{0}\mathbf{b}_2$ = [-65.5, 113.5, 98.2]
$^{3}\mathbf{b}_3$ = [136.4, 0, 101.7]	$^{0}\mathbf{b}_3$ =[-68.2, -118.1, 101.7]	$^{3}\mathbf{b}_3$ = [140, 0, 103.9]	$^{0}\mathbf{b}_3$ = [-70, -12.2, 103.9]
$^{0}\mathbf{c}_1$ = [55.6, 26.3, 22.7]	θ = -19.71°	$^{0}\mathbf{c}_1$ = [27.3, 47.1, 36.6]	θ = -7.81°
$^{0}\mathbf{c}_2$ = [-27.1, 39.5, 44.7]	ϕ = 5.69°	$^{0}\mathbf{c}_2$ = [-53.1, 38.0, 5.8]	ϕ = -18.04°
$^{0}\mathbf{c}_3$ = [7.4, -39.4, 51.8]	ψ = -38.19°	$^{0}\mathbf{c}_3$ = [-19.8, -22.1, 58.4]	ψ = -13.00°

4.4. Jacobian Analysis

The conventional velocity vector-loop method is used for analysis of the Jacobian matrix. Generally, the velocity vector of a point is formulated from two different directions of a loop closure. Each loop closure consists of a fixed base, a moving platform and all the links of a limb. The unactuated joint rates in each limb are then eliminated by performing a dot product of the velocity vector-loop equation with an appropriate vector that is normal to all vectors of the unactuated joint rates. Finally, the resulting equations are assembled into a Jacobian matrix.

Since the manipulator only possess 3 rotational degrees of freedom, the input vector can be written as $\dot{\boldsymbol{q}}=[\dot{\theta}_{11} \quad \dot{\theta}_{12} \quad \dot{\theta}_{13}]^T$, and the output vector can be described by the

angular velocity of the moving platform: $\dot{\boldsymbol{x}}=\boldsymbol{\omega_b}=[\dot{\omega}_x \quad \dot{\omega}_y \quad \dot{\omega}_z]^T$. Referring to Figure 4.3, a loop-closure equation for the i^{th} limb can be written as:

$$\overline{A_iB_i}+\overline{B_iC_i}=\overline{A_iO}+\overline{OC_i}, \qquad i=1,2,3 \tag{4.26}$$

Here $\overline{A_iB_i}$ corresponds to a vector along the distal link and $\overline{B_iC_i}$ to one along the proximal link. Taking the derivative of Eq. (4.26) with respect to time yields a velocity vector-loop equation as follows:

$$d_{AB}\boldsymbol{\omega}_{1i}\times s_{AB}+d_{BC}\boldsymbol{\omega}_{2i}\times s_{BC}=d_{OC}\boldsymbol{\omega}_b\times s_{OC}, \qquad i=1,2,3 \tag{4.27}$$

where $\boldsymbol{\omega}_b$ is the rotational velocity of the moving platform and ω_{ji} for j = 1, 2 is the angular velocity of the j^{th} link of the i^{th} limb. Parameters d_{AB} and d_{OC} denote the length of vectors $\overline{A_iB_i}$ and $\overline{OC_i}$; s_{AB}, s_{BC} and s_{OC} are unit vectors expressed in the global frame pointing along $\overline{A_iB_i}$, $\overline{B_iC_i}$, and $\overline{OC_i}$ respectively. Vector $\boldsymbol{\omega}_{1i}$ represents the angular velocity of the active joint of limb i with respect to the global frame, while all the other joint rates are passive variables. To eliminate the passive joint rate variable $\boldsymbol{\omega}_{2i}$, both sides of Eq. (4.27) are dot-multiplied by s_{BC}:

$$d_{AB}\boldsymbol{\omega}_{1i}.(s_{AB}\times s_{BC})=d_{OC}\boldsymbol{\omega}_b.(s_{OC}\times s_{BC}), \qquad i=1,2,3 \tag{4.28}$$

when written once for each i = 1, 2, and 3, Eq. (4.28) yields three scalar equations which can be arranged in matrix form:

$$\mathrm{J}_x\boldsymbol{\omega}_b=\mathrm{J}_q\dot{\mathbf{q}} \tag{4.29}$$

where the J_x and J_q matrices are given respectively as follows.

$$\mathrm{J}_x=\begin{bmatrix} d_{AB}(s_{AB}\times s_{BC})_1^T \\ d_{AB}(s_{AB}\times s_{BC})_2^T \\ d_{AB}(s_{AB}\times s_{BC})_3^T \end{bmatrix}$$

$$\mathrm{J}_q=\begin{bmatrix} d_{OC}(s_{OC}\times s_{BC})_1 & 0 & 0 \\ 0 & d_{OC}(s_{OC}\times s_{BC})_2 & 0 \\ 0 & 0 & d_{OC}(s_{OC}\times s_{BC})_3 \end{bmatrix} \tag{4.30}$$

Thus, the Jacobian matrix of the 3-RUS/S mechanism is given as follows:

$$\mathrm{J} = \mathrm{J}_q^{-1}\mathrm{J}_x$$

$$= \begin{bmatrix} d_{OC}(s_{OC} \times s_{BC})_1 & 0 & 0 \\ 0 & d_{OC}(s_{OC} \times s_{BC})_2 & 0 \\ 0 & 0 & d_{OC}(s_{OC} \times s_{BC})_3 \end{bmatrix}^{-1} \begin{bmatrix} (s_{AB} \times s_{BC})_1^T \\ (s_{AB} \times s_{BC})_2^T \\ (s_{AB} \times s_{BC})_3^T \end{bmatrix} \tag{4.31}$$

4.5. Performance Indices

Several well-established performance indices for parallel manipulators are commonly presented as a means of comparison between various mechanisms [36]. Having physical interpretations and useful applications for optimization purposes [44], these indices are usually derived from the Jacobian matrix.

With the development of the Jacobian matrix complete, the ability to derive performance indices for the 3-RUS/S is enabled. Upon calculating and analyzing these performance indices, two schemes for interfacing the mechanism with the human body were considered, as shown in Figure 4.8. Furthermore, the main focus was on the two major motions of the hip joint [58]: flexion/extension and abduction/adduction, while the third DOF of the hip joint (i.e. rotation) was assumed to be in its nominal position at all times. As can be deduced from Figure 4.8, the device's ψ angle corresponds to flexion/extension motions for Interfacing Scheme 1, while ϕ is associated with those motions in Interfacing Scheme 2; for both cases, θ corresponds to abduction/adduction motions. Additionally, the device parameters given in Table 4.1 are applied and the considered workspace of the manipulator was set to a range of $[-0.2\ 0.2]$ radians in both flexion/extension and abduction/adduction for all local performance studies.

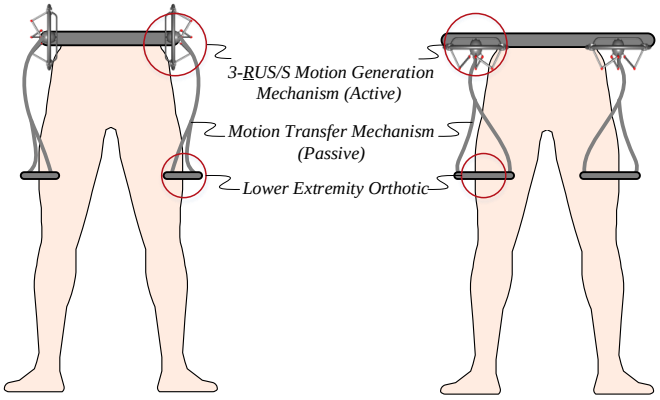

(a) Interfacing Scheme 1 *(b) Interfacing Scheme 2*

Figure 4.8. Considered 3-RUS/S attachment methods a hip exoskeleton

4.5.1. Manipulability

The isotropic manipulability of the 3-RUS/S manipulator has been investigated for the two different hip joint interfacing schemes shown in Figure 4.8. The manipulability deviation and its statistical distribution within the aforementioned desired workspace of the hip joint are depicted in Figure 4.9.

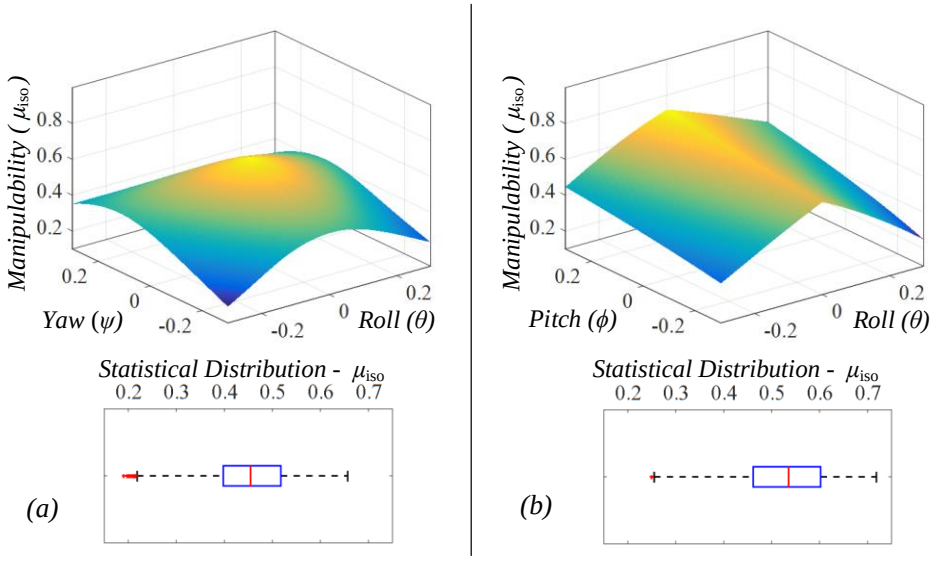

Figure 4.9. Manipulability for a) interfacing scheme 1 and b) interfacing scheme 2

According to these plots, the manipulability of the 3-RUS/S mechanism is greatest when operating at or near its 'home' position and significantly reduced near the

boundaries of the desired workspace for both interfacing schemes. Upon comparing the results, Interfacing Scheme 2 has a higher average manipulability than Interfacing Scheme 1. Meanwhile, the deviation of manipulability for both schemes is approximately equal within the desired workspace.

4.5.2. Dexterity (Condition Number)

Figure 2.10 shows the dexterity deviations and statistical distributions for both interfacing schemes of the 3-RUS/S manipulator considered in Figure 4.8. These plots indicate that the manipulator's dexterity is again at its highest level when the device is configured in the vicinity of its initial 'home' orientation and decreases as the mechanism approaches the boundaries of its desired workspace. Furthermore, when it is attached to the human body using Interfacing Scheme 2, the 3-RUS/S manipulator has a higher dexterity than when Interfacing Scheme 1 is utilized. Finally, the extent of dexterity deviation associated with Interfacing Scheme 2 is less than that of Interfacing Scheme 1, which provides further support of scheme (b) as the quantitatively favorable interfacing method.

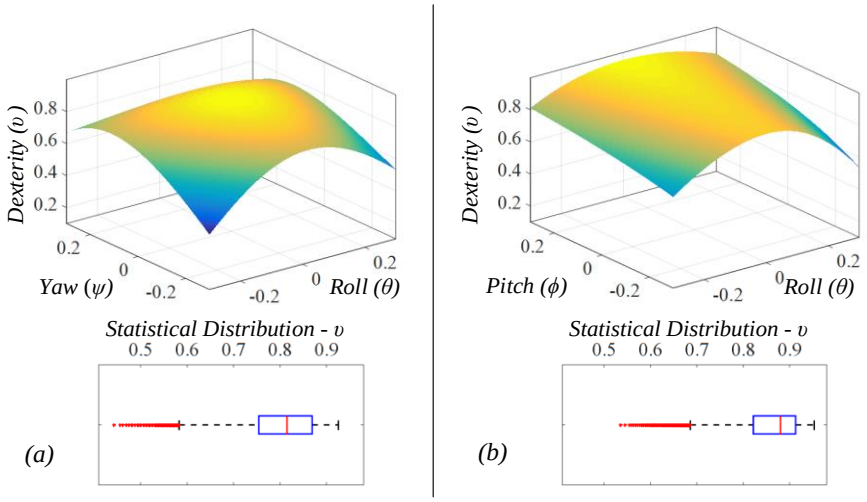

Figure 4.10. Dexterity for a) interfacing scheme 1 and b) interfacing scheme 2

4.5.3. Rotational Sensitivity

Figure 4.11 shows the sensitivity deviation and statistical distribution for the 3-RUS/S manipulator in the same two different interfacing schemes. From these results,

one can conclude that the sensitivity of the device in both schemes is at its lowest when functioning near the vicinity of its 'home' configuration and becomes increasingly sensitive when moving to the boundaries of its assumed workspace. Moreover, the average sensitivity and overall deviation of the 3-RUS/S manipulator for Interfacing Scheme 2 proves to be less than what the 3-RUS/S manipulator experiences for Interfacing Scheme 1. Thus, the former scheme is again the more robust option in terms of sensitivity performance.

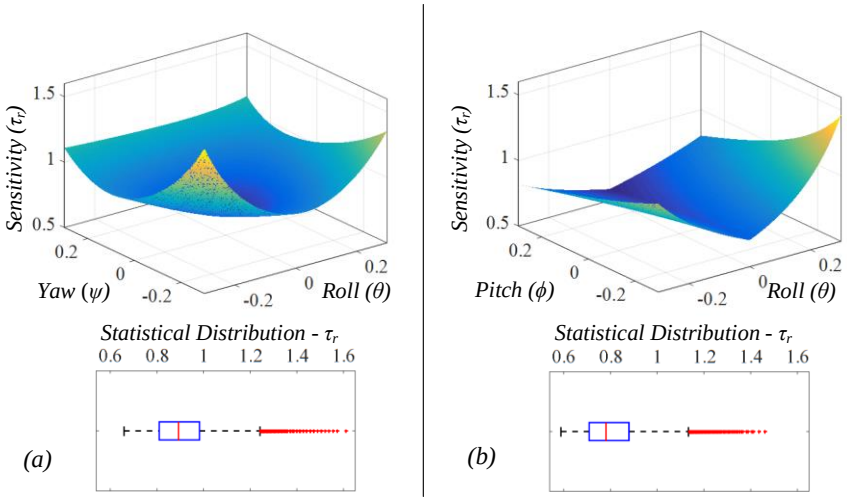

Figure 4.11. Sensitivity for a) interfacing scheme 1 and b) interfacing scheme 2

4.5.4. Global Manipulability Index for Optimizing the 3-RUS/S

Based on the results obtained from the local performance indices of the 3-RUS/S manipulator in Sections 4.5.1 – 4.5.3, Interfacing Scheme 2 has been chosen for the optimization process because it consistently provides preferable performance to that of Interfacing Scheme 1. Furthermore, the design variables chosen for the optimization process are the ratio of moving platform radius to base platform radius and the local-frame height of points $\mathbf{c}_i$ for $i = 1, 2,$ and 3. The optimization procedure takes place by finding the average performance index values for different combinations of spherical joint height and device radii ratio.

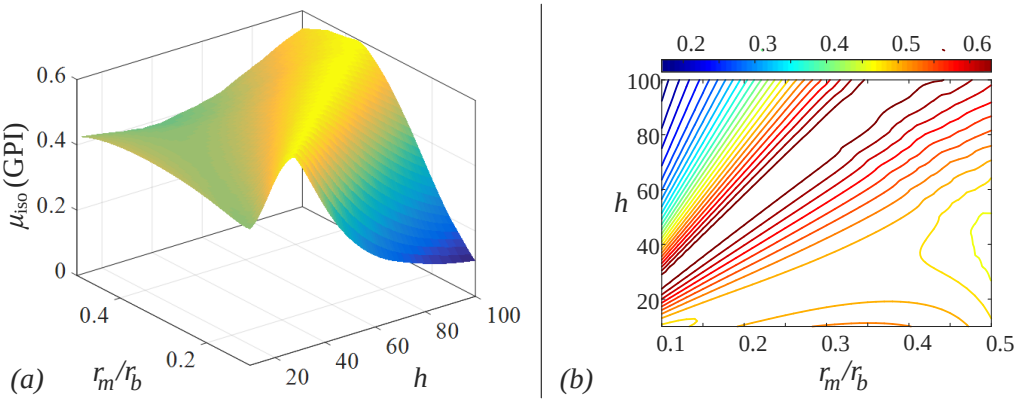

Figure 4.12. Global manipulability analysis of the 3-RUS/S manipulator

Figure 4.12 a) shows the optimization results obtained for the manipulability index. Note that the trend is essentially the same for both dexterity and sensitivity. From the contour plot of Figure 4.12 b), one can conclude that a linear function of parameters provides a set of highest performing design options. The geometric relation between components that provides optimal performance can be described by the following:

$$h = 10^{-3}\left(3.4\frac{r_m}{r_b} - 0.2\right) \tag{4.32}$$

Thus, the optimized design for the 3-RUS/S is scalable according to Eq. (4.32).

4.6. Dynamic Simulation Results

Figure 4.13 shows simulated torque, velocity, and power curves for the 3-RUS/S mechanism actuators during normal gait cycle motions [59]. These plots were obtained by subjecting a Matlab/SimMechanics simulation model's end-effector to the 3-DOF torques and motions experienced by a 75.16 kg person's hip during normal gait cycle motions, as provided by the OpenSim software [60], and monitoring motor torques and velocities using virtual sensors. Note that in the uppermost figure, only the torque in the axis of flexion/extension motions is shown. As can be observed in the uppermost plot, the parallel connection of actuators in the 3-RUS/S design causes the torque requirements of each individual actuator to be significantly less than the torque requirement at the end-effector. The maximum magnitude torque, velocity, and power associated with Scheme 1 are 23.8 N.m, 1.8 rad/s, and 16.7 W, while for Interfacing

Scheme 2 are 26.3 N.m, 1.4 rad/s, and 15.4 W. Thus, in terms of torque, Scheme 1 is superior, but in terms of speed and power, scheme 2 is superior to Scheme 1.

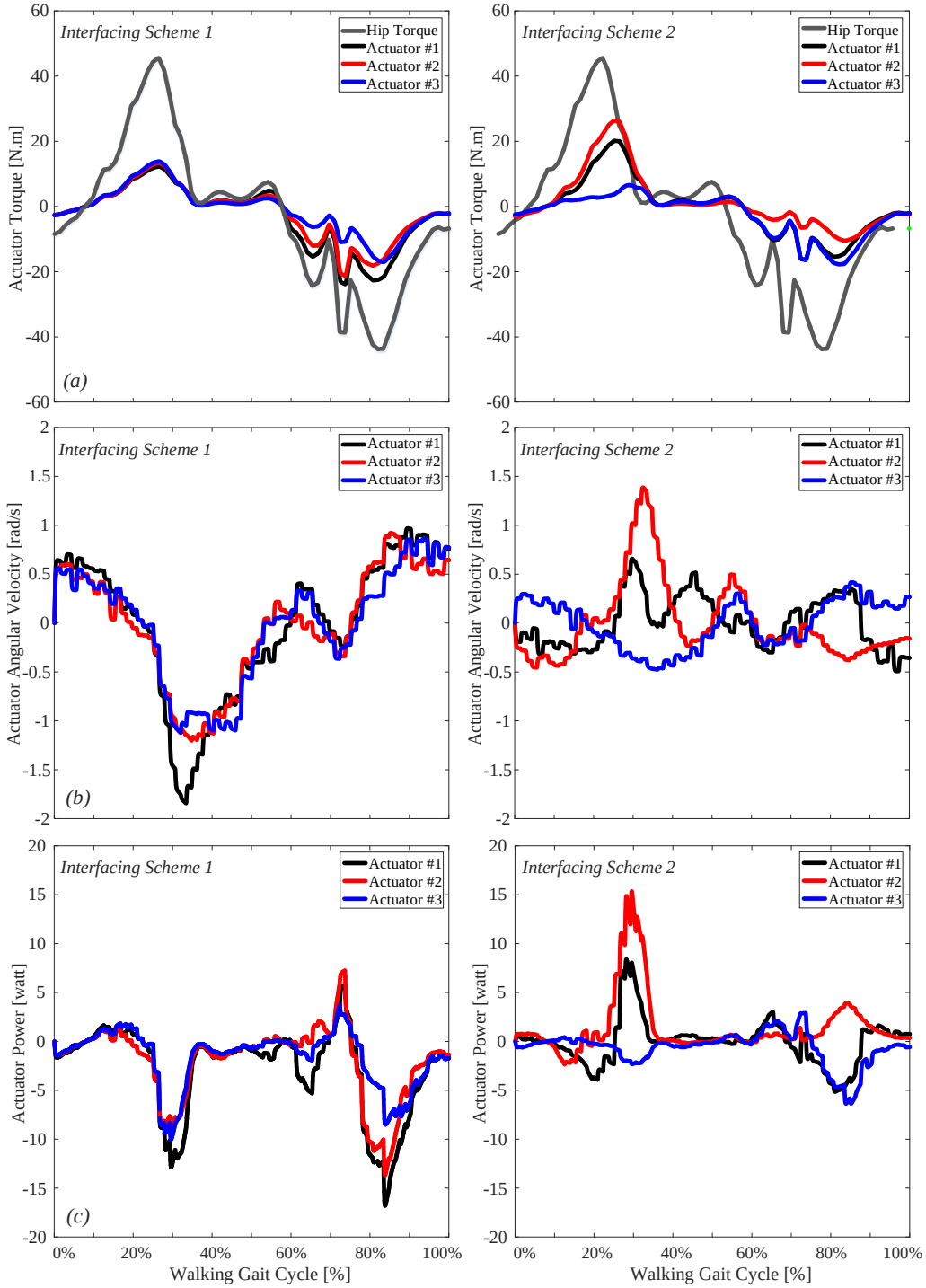

Figure 4.13. Torque, speed, and power required for the 3-RUS/S mechanism to emulate hip joint motion during normal gait

4.7. Experimental Study on the 3-RUS/S Manipulator

Although the simulation results and numerical examples of Section 4.4 provide useful insight on the correctness and implementation of the kinematic equations derived in this study, they do not account for practical issues such as the mechanical interferences. In order to explore the nuances associated with physical reality, a prototype 3-RUS/S mechanism was fabricated and tested for performance evaluations. The following subsections discuss the fabrication and experimental results obtained.

4.7.1. Mechanism Fabrication Details

All structural components of the device, including proximal and distal links, were produced from a 3D printer such that the parameter values reported in Table 4.1 would apply to the prototype. As shown in Figure 4.16, the device's universal and spherical joints are off-the-shelf components. Meanwhile, the active 1-DOF rotary joints are realized as Maxon RE-max 29 brushed DC motors. Finally, a VectorNAV VN-100 Rugged inertial measurement unit (IMU) was fixed to the device's moving platform as a means of measuring its spatial orientation during operation. Note that the size of the prototype device reflects the design parameter selection decision (i.e. the values provided in Table 4.1); if a more compact embodiment is required, the manipulability optimized design can be scaled according to Eq. (4.32).

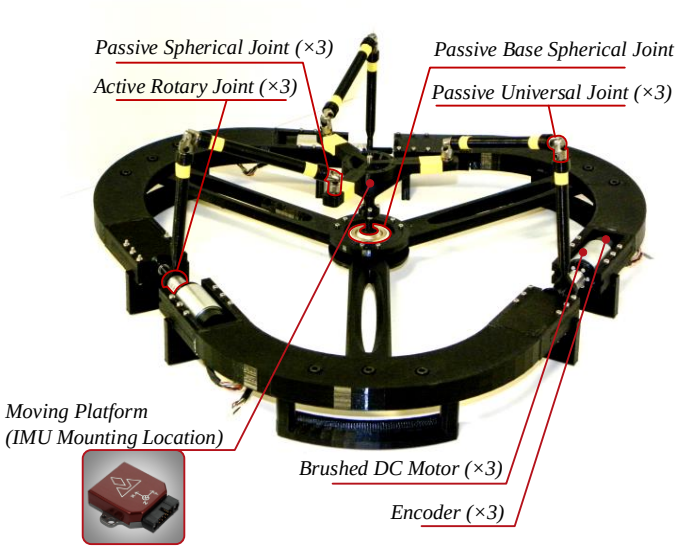

Figure 4.14. Experimental prototype of the 3-RUS/S manipulator

4.7.2. Experimental Results

The 3-RUS/S device's 1-DOF joints were controlled using a simple PI scheme with feedback supplied from the actuator's attached encoders. For the experiment, the device was made to track the 3-DOF motions undergone by an average human hip joint during a normal gait cycle [35, 36].

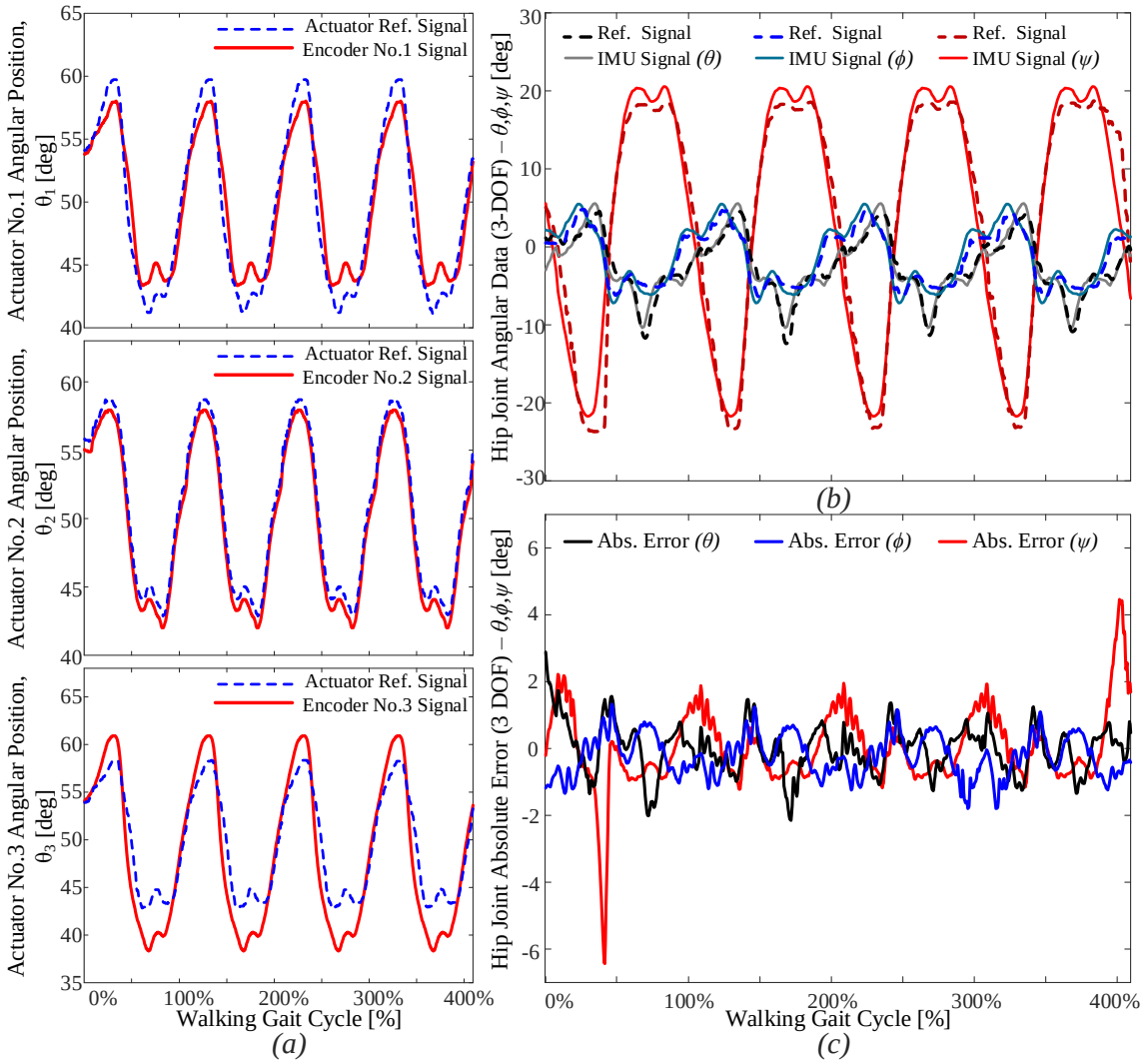

Figure 4.15. a) Comparison of reference signal and encoder feedback, b) comparison of desired end-effector orientation and IMU-measured value and c) absolute error between desired end-effector orientation and IMU-measured value during gait motion tracking of the 3-RUS/S

The reference signals provided to the motors derived from these desired 3-DOF motions through the inverse kinematics algorithm presented in Section 4.2, where θ

corresponded to hip abduction/adduction, ϕ to hip rotations, and ψ to flexion/extension motions. The experimental results of Figure 4.15 a) shows the reference signals provided to each actuator along with their angular position response, as measured by the system's encoders. Furthermore, Figure 4.15 b) also presents the original gait signals and moving platform's 3-DOF orientation response. Ultimately, the close agreement between input and output signals depicted in Figure 4.15 b) suggests that the proposed 3-RUS/S parallel mechanism is able to accurately track the motions associated with the human hip joint during a normal gait cycle. The observable errors between the reference signals and system response signals in Figure 4.15 c) can be primarily attributed to the simple control algorithm, which did not account for nonlinearity in the device dynamics.

4.8. Conclusion

This study proposed the design of an orientation parallel manipulator for possible application as a robotic hip exoskeleton. Algorithms were developed for unique solutions to both the forward and inverse kinematics problems. The forward kinematics procedure involved simple precursory computations to find universal joint positions, followed by more complex mathematics based on sphere intersections and distances between arbitrarily-oriented circles in 3-dimensional space to find spherical joint positions. It is recommended that numeric methods be employed when finding solutions to the latter problems. When applicable, each of a multiplicity in solutions must be evaluated for physical feasibility before a unique solution can be arrived upon. The forward kinematic algorithm then concludes with a set of linear equations and trigonometric functions. Contrarily, inverse kinematics solutions are taken as the positive roots of the inverse kinematics equation presented.

An experimental study of a prototype device's kinematic capabilities suggests that its design principle is feasible for application as a hip exoskeleton. More significantly, the experimental results indicate that the mechanism can provide full kinematic relation with the motions a human hip undergoes during normal gait cycles.

The advantages of using 3RUS/S mechanism as the actuating part of the hip exoskeleton can be attributed to its easy control algorithm and simple inverse

kinematics. The aforementioned manipulator contains 3 motors which already makes it a better candidate when compared to the Stewart-Gough manipulator that has 6 motors. The mechanism however has some shortcomings which are mainly related to its mechanical characteristics. These shortcomings include lack of compactness, which in turn affects aesthetic quality. Moreover, the system incorporates a universal and a spherical joint on each link and the moving platform is also constrained by a spherical joint. Overall, the mechanism contains 3 universal joints and 4 spherical joints. Physical universal or spherical joints, have the intrinsic problem of limited range of motion and can easily get locked in certain orientations and conditions. These characteristics would dramatically decrease the overall allowable workspace of the mechanism when fabricated and prototyped in reality. As a result, the 3-RUS/S manipulator may not be able to cover and support the desired ranges of motion required for the hip joint and/or the multi-DOF joints of its links could have a nonlinear behavior in certain conditions and loads.

Chapter 5.

Performance Analysis and Experimental Study of a 3-RRR Spherical Parallel Manipulator for Lower Limb Exoskeleton Applications

The presence of one or more joints with multiple active degrees-of-freedom (DOFs) in the pertinent limb complicates the design of an exoskeleton. One method to address this challenge is to restrict the motions that the exoskeleton supports about the multi-DOF joint. This is the common design method for current exoskeleton research and technologies [21, 22], [37, 38].

In this chapterthe use of a parallel robot paired with a mechanical structure that transmits motions to the targeted body part in a comfortable, non-restrictive way is proposed. One parallel robotic structure that has potential for use in such an application is the 3-RRR spherical parallel manipulator. Among previous works in the literature, Gosselin and Angeles present an inverse kinematics analysis, along with discussions of design optimization and singularities, for this manipulator in [63]. Gosselin and Lavoie further discuss the kinematic design and Jacobian derivation for the mechanism in [64]. Gosselin and Hamel have gone on to present a specific embodiment of the manipulator, the Agile Eye, in [65]; Gosselin and St-Pierre further develop its kinematic description and experimentation in [66]. More recently, Bai *et al*. revisit the forward displacement analysis of the 3-RRR manipulator and introduce a new embodiment, called the Agile Wrist, in [50]. Most recently, Niyetkaliyev and Shintemirov detail one method of obtaining forward and inverse kinematics solutions for the Agile Wrist design, including simulation results and numerical examples for verification in [52].

This chapter investigates the performance of the 3-RRR in the context of exoskeleton applications. Specifically, manipulability, dexterity, and rotational sensitivity

performance indices are evaluated for two different body-interfacing schemes of the manipulator when it is applied as a hip exoskeleton device; here it is assumed that the manipulator supports 3-DOF rotational motions of the upper leg with respect to the pelvis. Our findings suggest a 3-RRR manipulator can be employed as the hip actuator in an exoskeleton system; this represents an original contribution to the field of exoskeleton research.

5.1. Kinematic Considerations for the 3-RRR Spherical Parallel Manipulator

5.1.1. Kinematic Architecture

Figure 5.1 shows a geometrical schematic of a generalized 3-RRR manipulator. This device is considered a 3-DOF spherical mechanism because all of its moving linkages perform spherical motions about a common point, O, that is stationary with respect to its base structure [2, 3].That is, all particles' motions within the system can be unambiguously described by radial projections on the surface of a unit sphere centered at the aforementioned stationary point. Consequentially, the only permissible lower-pair joint within a spherical mechanism's limbs is a revolute joint; furthermore, all joint axes must intersect at the common stationary point mentioned above. In Figure 5.1, linkages are labeled 0–7, where 0 indicates the fixed base structure and 7 corresponds to the manipulator's end-effector (i.e. the moving platform). A_i, B_i, and C_i denote the three revolute joints of each limb i, where $i = 1, 2, 3$ and only A_i joints are active.

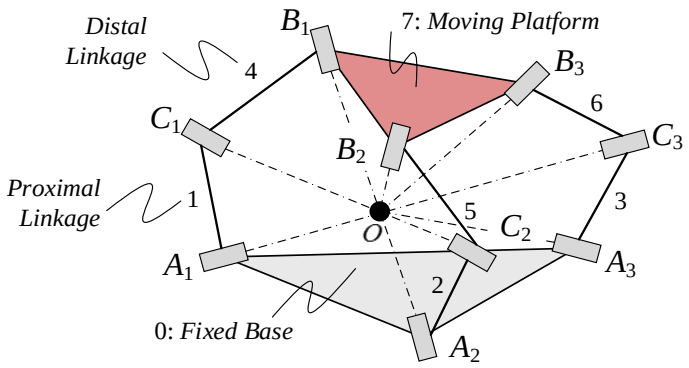

Figure 5.1. Schematic illustration of a generalized 3-RRR manipulator [36]

Note that two notable embodiments of the 3-RRR manipulator are the Agile Eye and Agile Wrist, as mentioned in the previous section and shown in Fig 5.2 (*a*) and Figure 5.2 (*b*), respectively. Although mechanically distinct, these two embodiments have the same inverse kinematics procedure, which is reviewed in the subsection that follows.

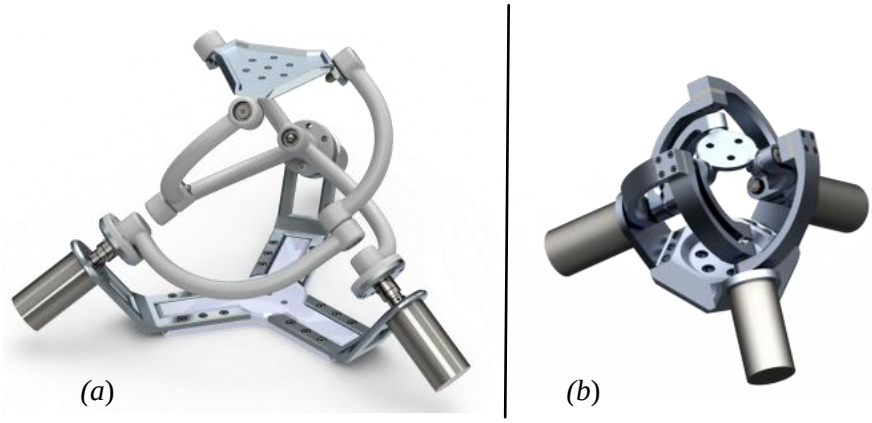

Figure 5.2. a) Agile eye and b) agile wrist embodiments of the 3-RRR manipulator

5.1.2. Inverse Kinematic Derivation

Inverse kinematics analysis for the 3-RRR manipulator has been examined extensively [16, 29], [25–27]. One approach is briefly revisited here again for the sake of completeness and to acclimatize the reader to the notations and naming conventions used subsequently in this research study.

To start, direction vectors $\mathbf{u_1}$, $\mathbf{u_2}$, and $\mathbf{u_3}$ specify the rotational axes of the system's three active A_i joints, as shown in Figure 5.3. These vectors have constant values with respect to the global frame (with origin O) because they correspond to fixed joints. Next, input scalar variables θ_1, θ_2, and θ_3 define the angular states of the respective active joints. Direction vectors $\mathbf{w_1}$, $\mathbf{w_2}$, and $\mathbf{w_3}$ in turn specify the rotational axes of the joints between the three proximal-distal link pairs (i.e. the C_i joints). These vectors vary in element values with respect to the global frame because they correspond to free joints. The final set of direction vectors: $\mathbf{v_1}$, $\mathbf{v_2}$, and $\mathbf{v_3}$, specify the rotational axes of the joints between the three connection points of the distal links to the end effector (i.e. the B_i joints). Again, these vectors vary with respect to the global frame because they correspond to free joints.

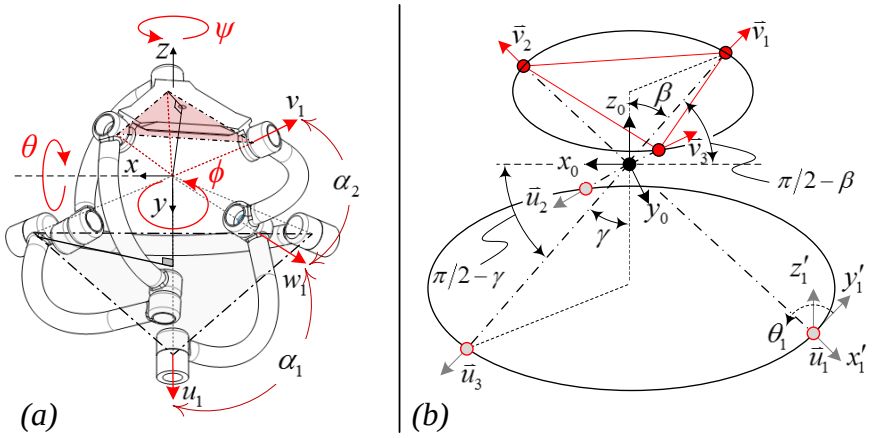

Figure 5.3. 3-RRR schematics with parameters and direction vectors labelled

Scalar constant α_1 specifies the angle between each actuated A_i joint and corresponding proximal C_i joint within the plane containing both of these joints as well as the global origin, O. The value of α_1 used for the 3-RRR design analyzed here is $90°$. The second scalar constant, α_2, specifies the angle between each proximal C_i joint and corresponding distal B_i joint within the plane containing both of these joints as well as the global origin. The value of α_2 used for the 3-RRR design considered here is also $90°$. Third, scalar constant β indicates the angle between the $\mathbf{v_i}$ direction vectors and the global z-axis when the device is in its 'home' position (i.e. when the plane created by A_i joint positions is parallel to that defined by the B_i points). The value of β used here is $54.75°$. Fourth, scalar constant γ indicates the angle between the $\mathbf{u_i}$ direction vectors and

the vertical axis (i.e. the global z-axis). Unlike β, this value is constant for all mechanism states because the joints corresponding to the $\mathbf{u}_i$ direction vectors are fixed relative to the global frame. The value of γ used in this analysis is also $54.75°$.

Finally, scalar constants η_1, η_2, and η_3 are used to specify the locations of the active joints associated with direction vectors $\mathbf{u}_1$, $\mathbf{u}_2$, and $\mathbf{u}_3$ and 'home-positioned' distal passive joints associated with $\mathbf{v}_1$, $\mathbf{v}_2$, and $\mathbf{v}_3$ within the global x-y plane. Measured with respect to the positive y-axis, the values of η_1, η_2, and η_3 are $0°$, $120°$, and $240°$ respectively. Using this convention, η_i directly specifies the directions $\mathbf{u}_i$ in the global x-y plane and specifies the directions $\mathbf{v}_i$ in the global x-y plane when added to $60°$ and the mechanism is in its 'home' position. Note that the above parameter values are not independent, as they are related through geometry.

Equations for the $\mathbf{u}_i$ direction vectors can be derived in terms of the η_i and γ parameters discussed above. This derivation involves the following fixed-frame rotation process: rotation of a local frame F_1 (i.e. originally identical to the global frame) by $(90° - \eta)$ about the global ${}^0y$-axis and then rotation of F_1 by η_i about the ${}^0z$-axis. This overall transformation is represented mathematically in [67]. Note that a superscript "0" indicates an axis or vector expressed with respect to the global frame.

$$R_{01} = R_z\left(\eta_i + 90°\right) R_y\left(90° - \gamma\right) = \begin{bmatrix} -S\eta_i S\gamma & -C\eta_i & -S\eta_i C\gamma \\ C\eta_i S\gamma & -S\eta_i & C\eta_i C\gamma \\ -C\gamma & 0 & S\gamma \end{bmatrix} \tag{5.1}$$

It follows that the x-axis of the resulting R_{01} orientation frame is equal to the direction vector $\mathbf{u}_i$:

$$\mathbf{u}_i = \begin{bmatrix} -S\eta_i S\gamma \\ C\eta_i S\gamma \\ -C\gamma \end{bmatrix}^T \tag{5.2}$$

Direction vectors $\mathbf{w}_i$ are in turn related to the corresponding $\mathbf{u}_i$ vectors through a fixed rotation by α_1 within the plane containing O, A_i, and C_i, along with a variable rotation dependent on actuator angle θ_i. The parameterization of this transformation can be considered a set of current frame rotations: first a rotation of θ_i about the local ${}^1x$-axis

and then a rotation of α_1 about the updated local z-axis. In matrix format, an expression for this is as follows:

$$R_x(\theta_i)R_z(\alpha_1)=\begin{bmatrix} C\alpha_1 & -S\alpha_1 & 0 \\ -S\theta_i S\alpha_1 & -S\theta_i C\alpha_1 & -C\theta_i \\ C\theta_i S\alpha_1 & C\theta_i C\alpha_1 & -S\theta_i \end{bmatrix} \tag{5.3}$$

Now, to obtain expression in terms of the global coordinate system, the set of rotations described above must be pre-multiplied by R_{01}. Finally, the set of direction vectors $\mathbf{w_i}$ are obtained from the resulting matrix set as the x-axes for each i, as shown below:

$$\mathbf{w_i}=\begin{bmatrix} \left(-S\eta_i C\gamma C\theta_i + C\eta_i S\theta_i\right)S\alpha_1 - S\eta_i S\gamma C\alpha_1 \\ \left(C\eta_i C\gamma C\theta_i + S\eta_i S\theta_i\right)S\alpha_1 + C\eta_i S\gamma C\alpha_1 \\ -C\gamma C\alpha_1 + S\gamma C\theta_i S\alpha_1 \end{bmatrix}^T \tag{5.4}$$

Similar to the derivation for $\mathbf{u_i}$ vectors summarized in Eq. (5.1) and (5.2), the $\mathbf{v_i}$ vectors can be established via two spatial rotations as follows when the device is in its 'home' position:

$$R_{03}=R_z(\eta_i)R_y(\beta) \tag{5.5}$$

Again, $\mathbf{v_i}$ is given as the x-axis component of the orientation matrix shown in Eq. (5.5). To determine the $\mathbf{v_i}$ directions after the mechanism's end-effector has undergone roll, pitch, and/or yaw rotations, R_{03} must be pre-multiplied by another transformation:

$$\begin{bmatrix} v_{ix} \\ v_{iy} \\ v_{iz} \end{bmatrix}=\begin{bmatrix} 1 \\ 0 \\ 0 \end{bmatrix}\cdot R_z(\psi)R_y(\phi)R_x(\theta)R_{03} \tag{5.6}$$

Given that all direction vectors $\mathbf{w_i}$ and $\mathbf{v_i}$ are of unit length, the angle between corresponding $\mathbf{w_i}$ and $\mathbf{v_i}$ vectors is α_2 (by the parameter's definition), and the geometric definition of the vector dot product, the following equation relates the two sets of direction vectors:

$$\mathbf{w_i}\cdot\mathbf{v_i}=\cos\alpha_2 \qquad\qquad i=1,\ 2,\ 3 \tag{5.7}$$

Now, through substitution of Eq. (5.4) and Eq. (5.6) into Eq. (5.7), a set of relationships between the system inputs and outputs is obtained. Upon performing this substitution and simplifying the result, the following equation is produced:

$$A \times tan^2(\theta_i / 2) + B \times tan(\theta_i / 2) + C = 0 \qquad i = 1, 2, 3 \qquad (5.8)$$

where

$$A = \left(-C\eta_i C\gamma S\alpha_1 + C\eta_i S\gamma C\alpha_1\right)v_{iy} + \left(S\eta_i C\gamma S\alpha_1 - S\eta_i S\gamma C\alpha_1\right)v_{ix} + \ldots\left(-C\gamma C\alpha_1 - S\alpha_1 S\gamma\right)v_{iz} - c\alpha_2 \qquad i = 1, 2, 3 \qquad (5.9)$$

$$B = 2S\eta_i S\alpha_1 v_{iy} + 2C\eta_i S\alpha_1 v_{ix} \qquad i = 1, 2, 3 \qquad (5.10)$$

$$C = \left(-S\eta_i C\gamma S\alpha_1 - S\eta_i S\gamma C\alpha_1\right)v_{ix} + \ldots\left(-C\gamma C\alpha_1 + S\alpha_1 S\gamma\right)v_{iz} + \left(C\eta_i C\gamma S\alpha_1 + C\eta_i S\gamma C\alpha_1\right)v_{iy} - c\alpha_2 \qquad i = 1, 2, 3 \qquad (5.11)$$

It follows that the input angle required to achieve a desired end-effector positional output can be found with the following equation:

$$\theta_i = 2atan\left(\frac{-B \pm \sqrt{B^2 - 4AC}}{2A}\right) \qquad i = 1, 2, 3 \qquad (5.12)$$

Eqs. (5.10 – 5.12) represent the solution to the inverse kinematics problem for the 3-RRR manipulator because they provide the required active joint states, θ_i, necessary to achieve a desired orientation of the end-effector. That is, once end-effector rotations θ, ϕ, and ψ, are established, the associated angular states of the active revolute joints can be identified.

5.2. Jacobian Analysis

A number of generally accepted performance indices for parallel manipulators are often published as a method for comparing various robotic manipulators [36]. The values of these indices usually have physical significance and applications for design optimization [68]. The three indices considered in this study, which are manipulability, dexterity, and rotational sensitivity, all derive from the Jacobian matrix of a manipulator.

Thus, the 3-RRR device's Jacobian development is discussed in this section, before the performance indices are examined in the next section.

As shown above, two components of the Jacobian are produced: J_x and J_q. The combination of these components yields the complete Jacobian matrix:

$$\dot{\mathbf{q}} = \mathrm{J}_q^{-1}\mathrm{J}_x\dot{\mathbf{X}} = \mathrm{J}\dot{\mathbf{X}} \tag{5.13}$$

when Eq. (5.13) is once for each of i = 1, 2, and 3, three scalar equations are produced. These can be arranged in matrix form as follows:

$$\begin{bmatrix} (\mathbf{w}_1 \times \mathbf{v}_1)^T \\ (\mathbf{w}_2 \times \mathbf{v}_2)^T \\ (\mathbf{w}_3 \times \mathbf{v}_3)^T \end{bmatrix} \boldsymbol{\omega}_b = -\begin{bmatrix} \mathbf{w}_1 \times \mathbf{u}_1.\mathbf{v}_1 & 0 & 0 \\ 0 & \mathbf{w}_2 \times \mathbf{u}_2.\mathbf{v}_2 & 0 \\ 0 & 0 & \mathbf{w}_3 \times \mathbf{u}_3.\mathbf{v}_3 \end{bmatrix} \dot{\mathbf{q}} \tag{5.14}$$

Combining (5.13) and (5.14) yields a complete form of the 3-RRR manipulator's Jacobian matrix:

$$\mathrm{J} = \mathrm{J}_q^{-1}\mathrm{J}_x = -\begin{bmatrix} \mathbf{w}_1 \times \mathbf{u}_1.\mathbf{v}_1 & 0 & 0 \\ 0 & \mathbf{w}_2 \times \mathbf{u}_2.\mathbf{v}_2 & 0 \\ 0 & 0 & \mathbf{w}_3 \times \mathbf{u}_3.\mathbf{v}_3 \end{bmatrix}^{-1} \begin{bmatrix} (\mathbf{w}_1 \times \mathbf{v}_1)^T \\ (\mathbf{w}_2 \times \mathbf{v}_2)^T \\ (\mathbf{w}_3 \times \mathbf{v}_3)^T \end{bmatrix} \tag{5.15}$$

Recall that vectors $\mathbf{u}_i$, $\mathbf{w}_i$, and $\mathbf{v}_i$ can be computed from Eq. (5.2), Eq. (5.4), and Eq. (5.7) respectively.

5.3. Performance Indices

With the 3-RRR manipulator's Jacobian matrix derived, it is now possible to evaluate several of the device's performance indices. In doing so, two methods for attaching the device to the human body are considered, as shown in Figure 5.4. Furthermore, only flexion-extension and abduction-adduction motions are considered; the final major DOF of the hip joint (i.e. internal/external rotation) is assumed to be constant and oriented such that the knee's axis of rotation is perpendicular to the sagittal plane of the body. As can be deduced from Figure 5.3, the device's ψ angle corresponds

to flexion/extension motions for Attachment Method 1, while ϕ is associated with those motions in Attachment Method 2; for both cases, θ corresponds to abduction/adduction motions. Additionally, a workspace range of $[-0.2\ 0.2]$ radians for both flexion-extension and abduction-adduction motions was considered for all local performance studies. Finally, the results below are only applicable when the parameter values (i.e. for α_1, α_2, β, γ, η_1, η_2, and η_3) are selected as per the discussion in Sec. 5.1.

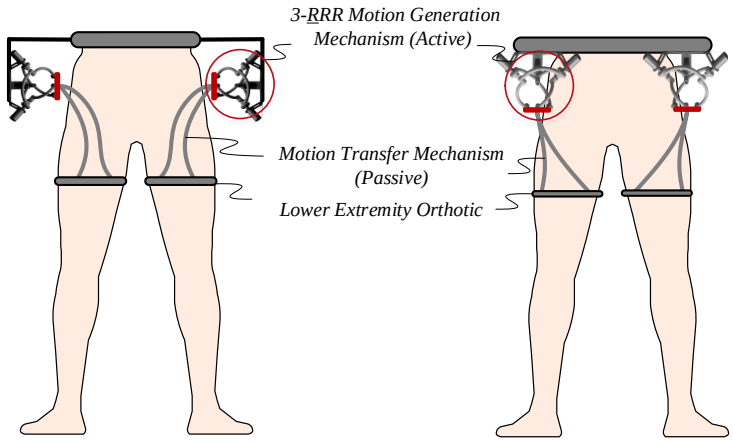

(a) Interfacing Scheme 1 *(b) Interfacing Scheme 2*

Figure 5.4. Considered 3-RRR attachment schemes for a hip exoskeleton

5.3.1. Manipulability

Figure 5.5 shows the 3-RRR device's manipulability deviation and statistical distribution within the considered workspace for the two attachment methods depicted in Figure 5.5. According to the surface plots, the manipulability of the 3-RRR is greatest when operating near its 'home' configuration and least near the boundaries of the considered workspace for both attachment methods. Comparatively, Attachment Method 1 achieves a greater average value for manipulability than Attachment Method 2. Furthermore, Method 1 achieves less variance in performance within the workspace considered. Therefore, scheme 1 is superior to scheme 2 in terms of manipulability.

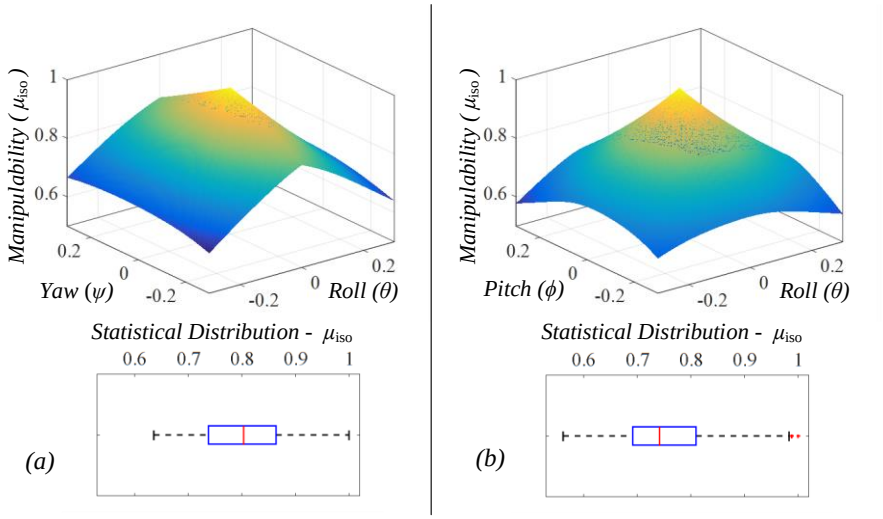

Figure 5.5. Manipulability for a) interfacing scheme 1 and b) interfacing scheme 2

5.3.2. Dexterity (Condition Number)

Figure 5.6 depicts dexterity index surface plots and statistical box plots for both body-attachment arrangements of the 3-RRR manipulator across its considered workspace. Similar to manipulability, these plots suggest that the mechanism's dexterity is greatest when configured in close proximity to its 'home' orientation and that it decreases as the device moves towards the boundaries of its considered workspace. Additionally, greater average dexterity and less dexterity variation are achieved when the 3-RRR robot is interfaced with the human body according to Attachment Method 1 as opposed to Method 2, which makes the former preferable.

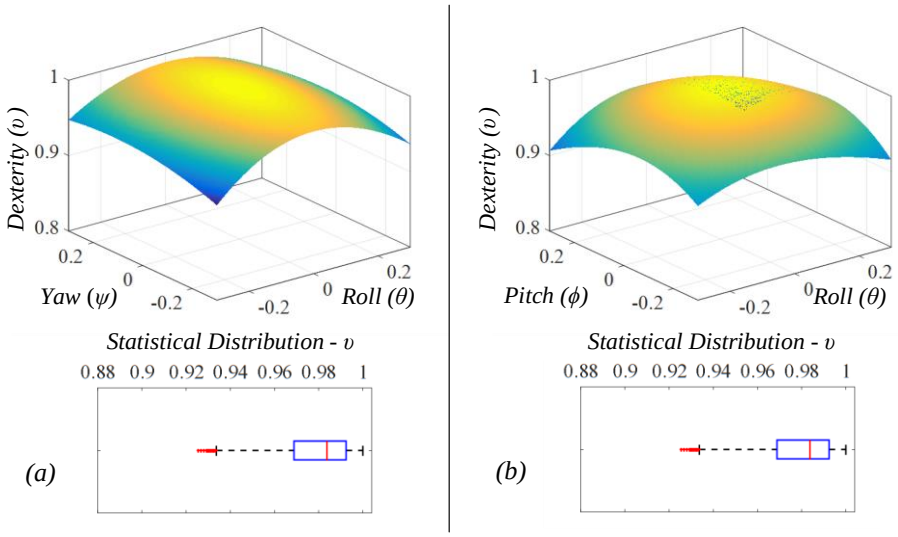

Figure 5.6. Dexterity for a) interfacing scheme 1 and b) interfacing scheme 2

5.3.3. Rotational Sensitivity

Figure 5.7 shows the sensitivity results for the 3-RRR manipulator when subject to the body-interfacing schemes of Figure 5.4 and constrained to the [–0.2 0.2] radian workspace range in both flexion-extension and abduction-adduction motions. Again, Attachment Method 1 demonstrates preferable performance to that of Method 2 because the former possesses the smaller-magnitude average and variance range in sensitivity index value. Furthermore, sensitivity performance is optimal for both arrangements near the device's 'home' orientation and degrades as the workspace limits are approached.

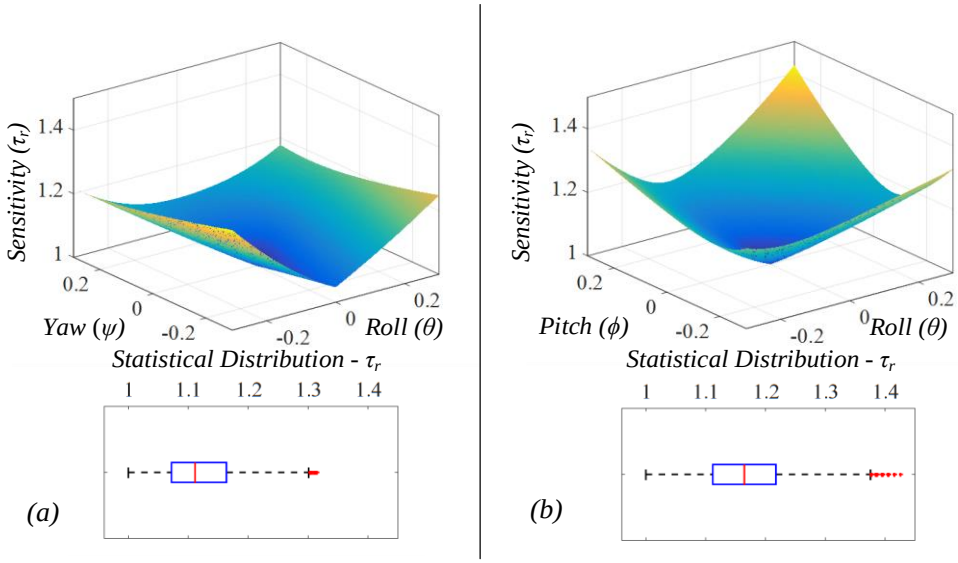

Figure 5.7. Sensitivity for a) interfacing scheme 1 and b) interfacing scheme 2

5.3.4. Overall Performance Comparison

In order to provide context to the 3-RRR mechanism's performance results, a comparison to those the 3-RUS/S orientation manipulator is shown in Figure 5.8.

As discussed in Sec. 5.3.1, a larger manipulability index value is generally preferable to a smaller one because greater values indicate that velocity can be transmitted to the end-effector in a more uniform manner. Similarly, greater dexterity index values are preferable, as they indicate greater kinematic accuracy. Meanwhile, small-magnitude sensitivity values are generally preferable to larger ones because actuator errors translate to more severe end-effector orientation errors for highly sensitive manipulators than less sensitive designs. Thus, given the results of Figure 5.8, the 3-RRR mechanism is a preferable design in terms of manipulability, sensitivity, and dexterity.

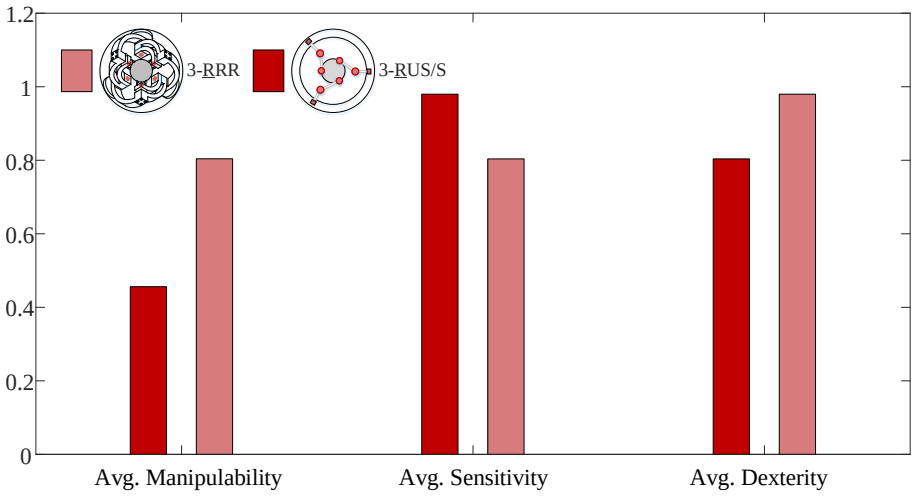

Figure 5.8. Performance comparison between 3-RRR and 3-RUS/S manipulator

5.4. Dynamic Simulation Results

Figure 5.9 shows simulated torque, velocity, and power curves for the 3-RUS/S mechanism actuators during normal gait cycle motions [35, 36]. These plots were obtained by subjecting a Matlab/SimMechanics simulation model's end-effector to the 3-DOF torques and motions experienced by a 75.16 kg person's hip during normal gait cycle motions, as provided by the OpenSim software, and monitoring motor torques and velocities using virtual sensors. Note that in the uppermost figure, only the torque in the axis of flexion/extension motions is shown. As can be observed in the uppermost plot, the parallel connection of actuators in the 3-RRR design causes the torque requirements of each individual actuator to be significantly less than the torque requirement at the end-effector (i.e. the hip torque). The maximum magnitude torque, velocity, and power associated with Interfacing Scheme 1 are 19.7 N.m, 3.7 rad/s, and 37.5 W, while those for Interfacing Scheme 2 are 46 N.m, 4 rad/s, and 43.5 W. Thus, in terms of torque, speed and power Scheme 1 is superior to Scheme 2. Note that a more accurate prediction of torque and power requirements can be made once the effects of the motion transfer mechanism are considered.

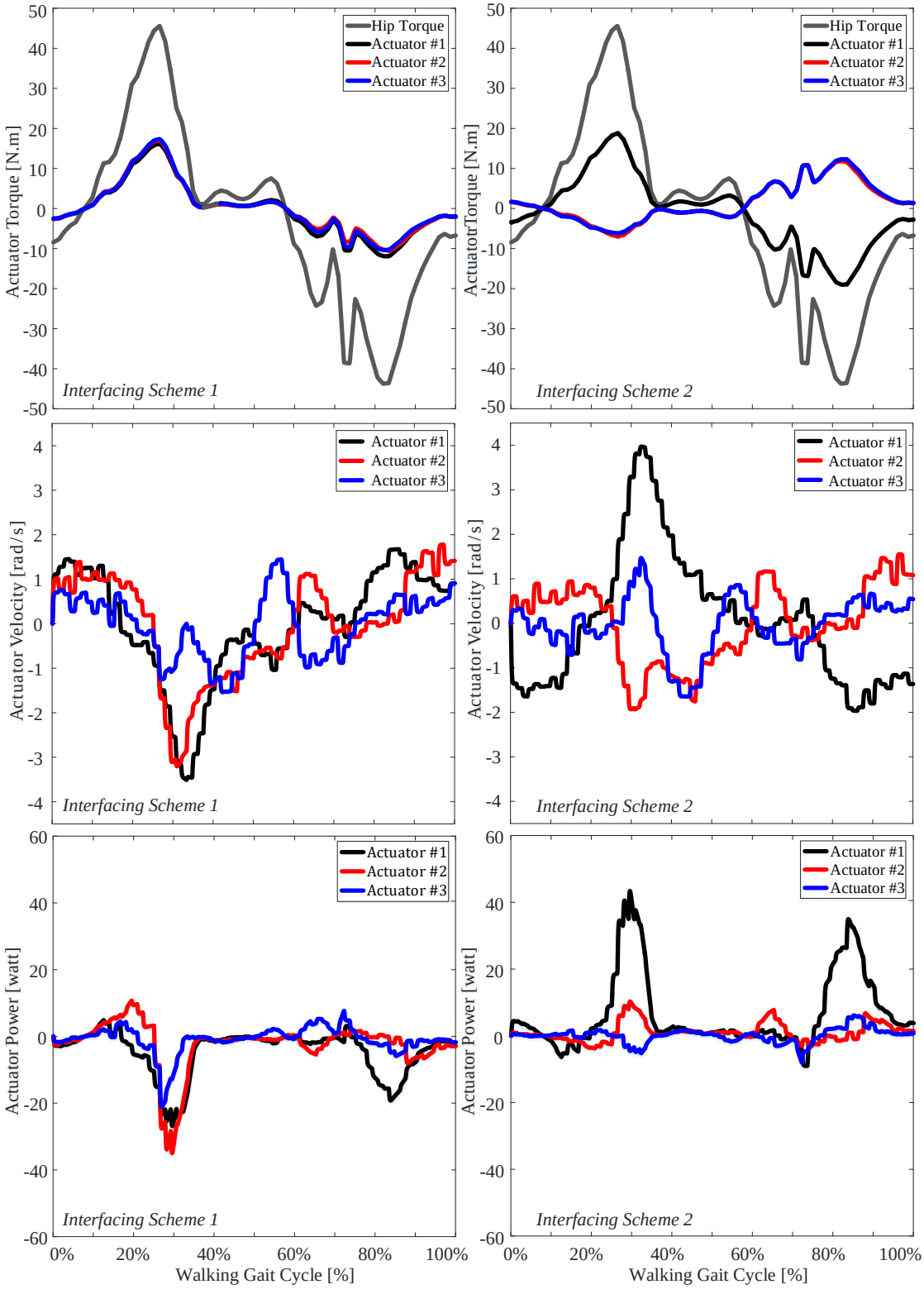

Figure 5.9. Torque, speed, and power required for the 3-RUS/S mechanism to emulate hip joint motion during normal gait

5.5. Experimental Study on the 3-RRR Manipulator

5.5.1. Mechanism Fabrication Details

In preparation for experimental tests on the 3-RRR manipulator design proposed in this study, a prototype system was fabrication. As shown in Figure 4.10, all linkage components of the device are 3D-printed, including the base structure, proximal and distal links, and end-effector platform. The prototype's passive revolute joints are composed of off-the-shelf shoulder screws, rotary ball bearings, and thrust bearings. Meanwhile, the active revolute joints are prototyped with Maxon RE-max 29 brushed DC motors. Lastly, a VectorNAV VN-100 Rugged inertial measurement unit (IMU) is attached to the end-effector platform for capturing orientation data during system operation.

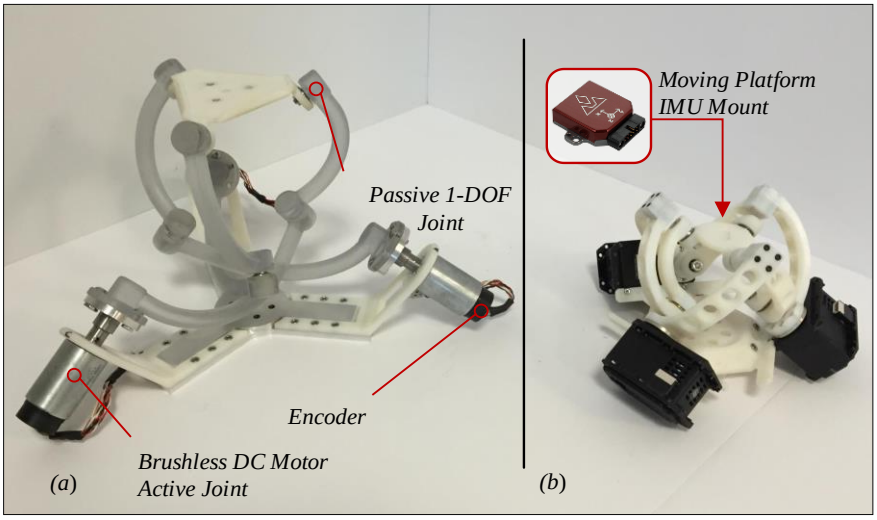

Figure 5.10. Experimental prototype of the a) agile eye and b) agile wrist

5.5.2. Experimental Results

The purpose of our experimental study on the 3-RRR prototype is to confirm its end-effector's ability to perform the 3-DOF motions experienced by the human hip joint during normal gait cycles. In order to complete this test, the prototype's motors are controlled with a simple proportional-integral (PI) scheme; angular feedback is provided by the actuator's attached encoders. In terms of test execution, reference signals for the

end-effector to track are provided by Stanford University's OpenSim software [35, 36]. Subsequently, motor reference signals are obtained by applying the inverse kinematics algorithm discussed in Sec. 5.1.2 to the OpenSim angular motion signals. Because Attachment Method 1 is expected to provide superior manipulability, dexterity, and sensitivity performance than Method 2, the motion strategy associated with Method 1 is utilized. That is, the prototype's ψ motions are matched to hip flexion-extension motions, θ to abduction-adduction, and ϕ to internal/external rotations.

The experimental results of Figure 5.11 depict the reference and response signals associated with the individual system motors. These are the motions required by the selected design and body-attachment scheme to achieve the hip motions associated with normal gait cycles at the end-effector, as determined by the inverse kinematics algorithm. In turn, Figure 5.11 presents an overlay of the resulting end-effector orientation angles, as captured by the system IMU, and the desired angles, as provided by the OpenSim software.

The results shown in Figure 5.11 indicate that the 3-RRR manipulator can achieve the same motion ranges as the human hip during normal gait cycles. Furthermore, the plots suggest that the mechanism can complete these motions with a similar rate as the human hip. The maximum absolute error between a single desired end-effector angle and measured angle is 7.6 degrees, and it applies to ψ (i.e. flexion-extension motions); the root mean squared error values for θ, ϕ, and ψ are 1.2 degrees, 0.7 degrees, and 3.1 degrees, respectively.

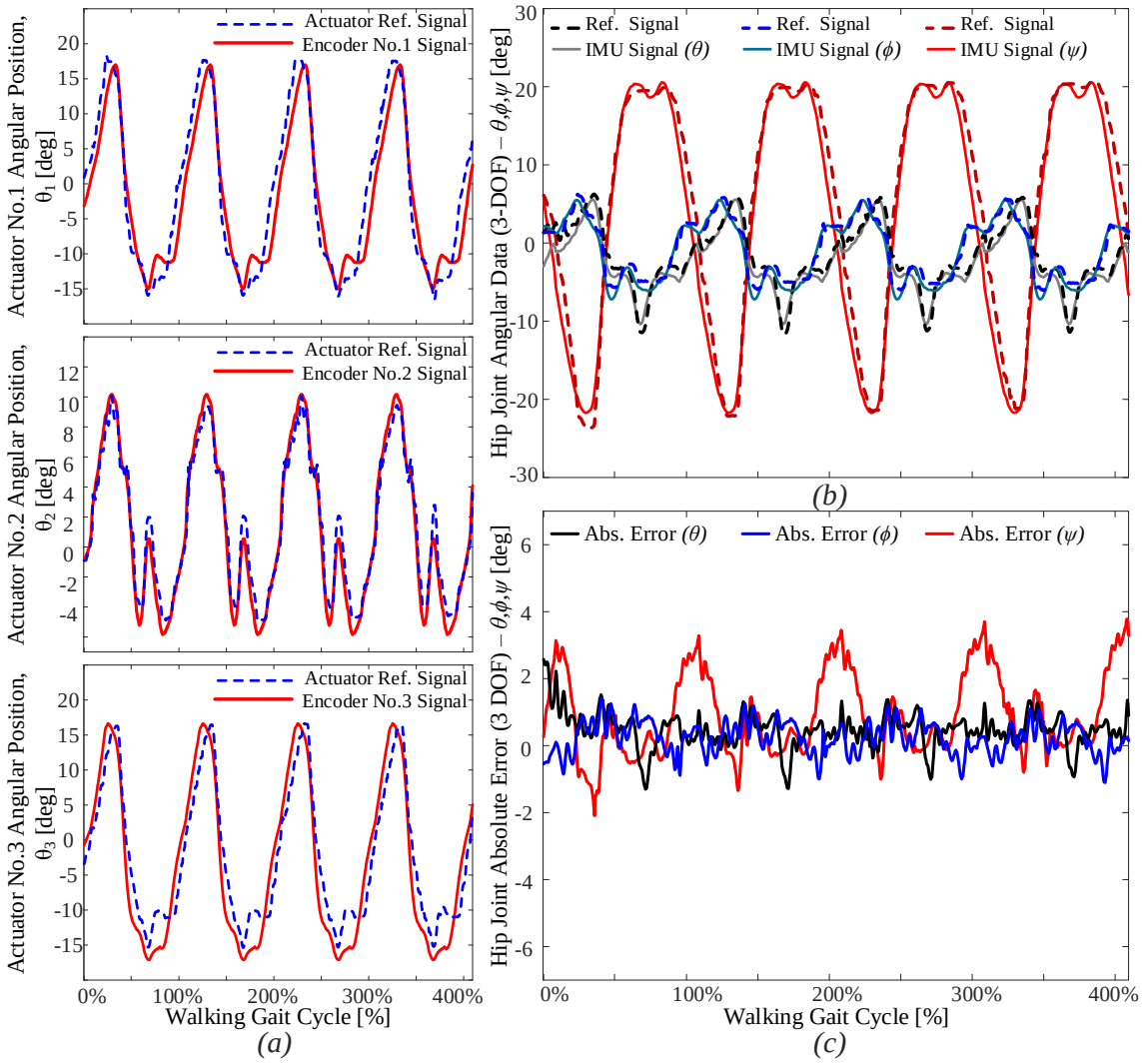

Figure 5.11. a) Comparison of reference signal and encoder feedback, b) comparison of desired end-effector orientation and IMU-measured value and c) absolute error between desired end-effector orientation and IMU-measured value during gait motion tracking 3-RRR

As shown in the absolute error plots of Figure 5.11, the error in ψ rises periodically during a rapid extension motion of the hip joint. This systematic error can be primarily attributed to the experiment's non-optimal control method, which does not account for inherent nonlinearities of the device's dynamics and inhibits the device from adequately tracking its reference signal. Therefore, the development of a more effective control algorithm would likely reduce the end-effector's orientation errors. Given this solution and the otherwise small magnitudes of error, it is feasible that the 3-RRR manipulator be used within a hip exoskeleton system.

5.6. Conclusion

This chapter proposed the use of the well-established 3-RRR spherical parallel manipulator as a robotic component within a hip exoskeleton system. Before investigating the mechanism's performance for two different body-attachment methods and presenting the results of a motion-tracking experiment, the device's inverse kinematics and Jacobian matrix development procedures were revisited.

The performance study results indicate the body-interfacing scheme 1 is superior in terms average value and variability for manipulability, dexterity, and rotational sensitivity indices. As can be expected, the manipulator's performance is optimal when configured at its initial 'home' orientation and degrades as the end-effector moves away from this state.

For the experimental study, a prototype manipulator's end-effector was controlled to track the motions experienced by a human hip joint during normal gait cycles. In summary, the general agreement between input and output signals depicted in the result figures suggests that application of this 3-RRR design as a hip exoskeleton is feasible. Furthermore, this application poses a motion assistance for multi-DOF body joints.

Chapter 6.

Design and Kinematic Analysis of a Hybrid SRRP/S Manipulator for Orientation and Motion Guidance of Spherical Joints

Various mechanical systems could be improved by or altogether rely on a robotic mechanism that provides orientation guidance for a ball-and-socket or spherical joint. Such applications generally require two guidance properties: minimal intrusiveness to the targeted joint and its associated mechanical system, and decoupled angular position control for each of the three degrees-of-freedom (DOFs) that define the joint's spatial orientation. Consequentially, the robotic guidance mechanism must provide kinematic relation with the 3-DOF rotational capability of the spherical joint and develop torques along three perpendicular axes at the target joint, while minimizing or preventing intrusive force assertion at that point.

One major shortcoming associated with robotic orientation guidance mechanisms for spherical joints is their lack of complete kinematic relation with the targeted joint. In terms of hip exoskeleton applications, this limitation restricts the range of hip-joint motions for which mechanism offers guidance to an orientation space less extensive than normal human capabilities. Based on current literature in the field of wearable robotics and exoskeletons, the majority of exoskeletons associated with ball-and-socket joints do not provide full kinematic relation with all three DOFs [30], [69]–[81] ,[82].

In order to overcome these shortcomings, a robotic mechanism that combines a spherical parallel manipulator, providing 3-DOF rotational motion generation about one point in space and a passive mechanism that non-intrusively transmits the spherical motion to a target ball-and-socket joint located at another point in space is proposed. Specifically, the device focuses on hip exoskeleton application and employs the Agile Eye, a spherical parallel manipulator embodiment introduced by Gosselin and Hamel in

[65]. The kinematic analysis of the Agile Eye is already well-established, with a kinematic description and experimentation completed by Gosselin and St-Pierre in [66]. Furthermore, the family of devices in which the Agile Eye belongs, the 3-RRR manipulator design, is analyzed in many more pieces of literature. Gosselin and Angeles document an inverse kinematics analysis, singularity analysis, and design optimization procedure for the 3-RRR in [83]; Bai *et al*. present a forward displacement analysis and introduce another design embodiment, the Agile Wrist, in [84]; Niyetkaliyev and Shintemirov detail a systematic approach for obtaining forward and inverse kinematics solutions for the Agile Wrist and present verification in the form of simulations and numerical examples in [52]. Note that design-related parameter values differ but the kinematic analysis is identical between the Agile Wrist and the Agile Eye.

This chapter presents a novel SRRP/S mechanism design, incorporating the well-established Agile Eye, that enables decoupled and orientation guidance of a ball-and-socket or spherical joint. The kinematic architecture associated with the design is described and both inverse and forward kinematic analyses for the complete mechanism are detailed. With focus on hip exoskeleton application, simulation results are presented as verification of the inverse kinematics algorithm. Furthermore, the results obtained from a prototype device during a gait motion experiment are documented as an indication of the device's ability to convey and guide 3-DOF rotational motion to a ball-and-socket joint.

6.1. Mechanical Design of the SRRP/S mechanism

The following subsections respectively describe the mechanical architecture of the SRRP/S mechanism in both a general context and with regard to specific application as a hip exoskeleton device.

6.1.1. General Schematic Design

Figure 6.1 shows a mechanical schematic of the mechanism proposed in this paper. The design includes a 3-RRR manipulator composed of three parallel-connected 1-DOF rotary joints, which are designated with 'R'; underlined letters indicate that the

associated joint is active, while joints without underlined labels are passive. In accordance with this labelling convention, the Figure 6.1 schematic indicates that two passive rotary joints are serially attached to the 3-RRR manipulator's end-effector, followed by a series-connected 1-DOF passive prismatic joint (designated with 'P'). Finally, the prismatic joint connects to the target 3-DOF ball-and-socket or spherical joint, which is labelled with 'S'. The lack of an underline in the spherical joint's label confirms that it is assumed to be passive.

As a consequence of this design scheme, a suitable technical name for the proposed mechanism, including the target spherical joint, is (3-RRR)RRP/S. Within the brackets, '3-RRR' represents the three parallel-connected limbs, each containing one active and two passive rotary joints; furthermore, the 'RRP' immediately following the closing bracket suggests the series connection of the associated passive joints, and the ending '/S' represents the passive spherical-joint constraint asserted by the target spherical joint on the final prismatic joint in the kinematic chain. Alternatively, the mechanism's name can be shortened to SRRP/S, because the 3-RRR component effectively represents an active spherical joint.

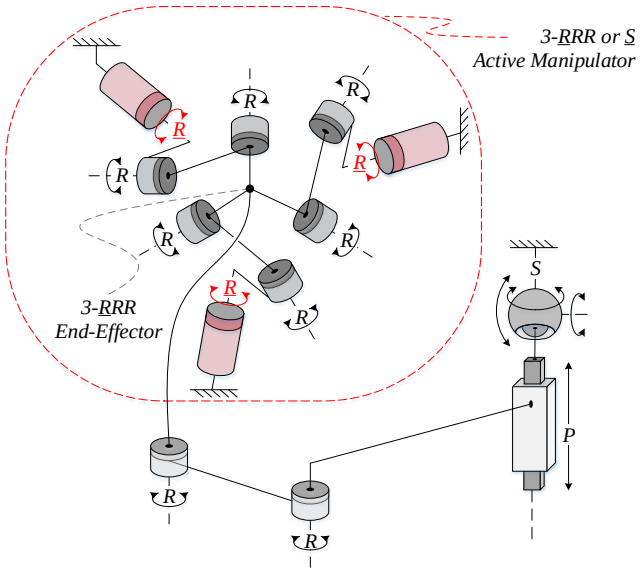

Figure 6.1. Mechanical schematic of the proposed SRRP/S mechanism

6.1.2. Design for Hip Exoskeleton Applications

As mentioned earlier, one particularly relevant application for the SRRP/S mechanism is its embodiment as a hip exoskeleton attached to the human body. For this application, the spherical joint targeted for orientation guidance is the human hip joint. Therefore, the body's pelvis, hip joint, and femur are all included within the mechanical structure of the mechanism. Here, the pelvis acts as the base reference to which each active joint in the 3-RRR manipulator as well as the socket for the hip joint are rigidly connected. In our design, the 3-RRR manipulator takes the form of an Agile Eye oriented sideways with its base structure attached to a 'pelvis orthotic', which in turn attaches to the user's pelvis. These connections are clarified by the design illustration in Figure 6.2. The Agile Eye's base plane containing all three active rotational joint is positioned such that it is always parallel to the body's sagittal plane (i.e. dividing the body into left and right halves).

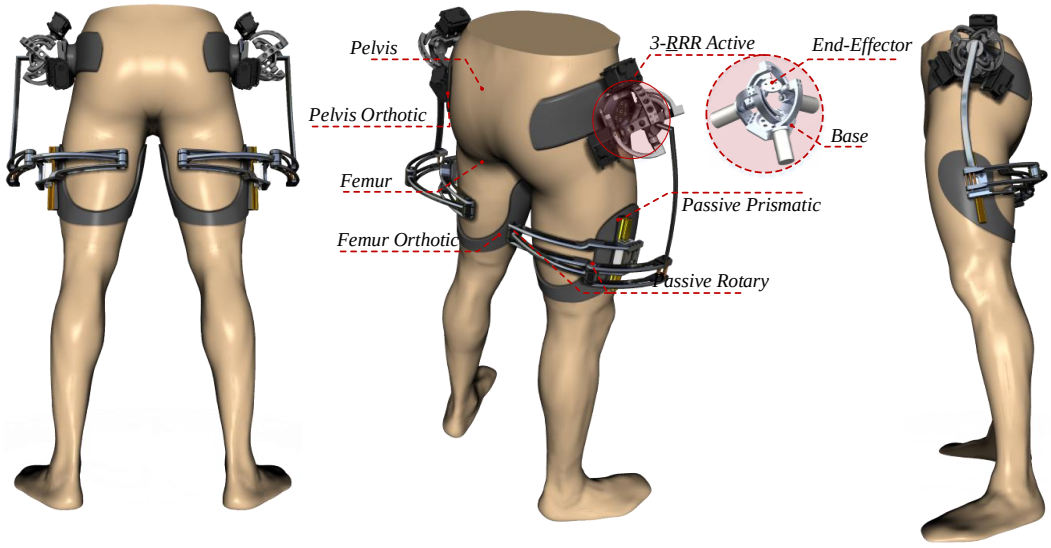

Figure 6.2. Mechanical design of the SRRP/S as a hip exoskeleton

Within this hip exoskeleton design, it is assumed that the human femur bone connects rigidly to the passively rotating ball of the hip's ball-and-socket structure. The SRRP/S mechanism's prismatic joint then achieves a fixed position with respect to the femur through attachment to the external surface of the upper leg via a 'femur orthotic', as shown in Figure 6.2. The two passive rotary joints located between the Agile Eye and

prismatic joint in the mechanism's kinematic chain are positioned posterior to the upper leg by way of rigid linkages extending down and backward from the Agile Eye and backward from the prismatic joint. A rigid linkage also connects these two rotary joints to each other.

The coordinated actions of the active rotary joints within the Agile Eye device cause its end-effector and consequentially the rigidly attached passive rotary joint to rotate in one or a combination of three mutually-perpendicular directions about a center-of-rotation point; this point is located between the Agile Eye's base and end-effector structures. The kinematic constraints associated with the passive rotary and prismatic joints subsequently convey a unique orientation to the hip joint (i.e. the femur relative to the pelvis) for every configuration of the Agile Eye within its practical workspace. Therefore, decoupled flexion/extension, abduction/adduction, and internal/external rotation motions can be transmitted to the user's hip joint by controlled actuations of the Agile Eye's active joint inputs. The relationship between the desired hip orientation output and the required corresponding angular states of the active joint inputs can be determined through the inverse kinematics analysis of the mechanism. Such an analysis is included in the following section.

6.2. Kinematic Analysis of the SRRP/S Mechanism

In the following subsections, a system of parameter and reference frame notations is introduced before both inverse and forward kinematic analyses for the SRRP/S mechanism are detailed.

6.2.1. Notation for Reference Frames, Joints and Motions

The geometrical schematic of Figure 6.3 shows three important reference frames associated with the SRRP/S mechanism that is used during the kinematic analyses beginning in the next subsection. The first of these frames, with origin position denoted by vector $\mathbf{p}$, is fixed to the user's pelvis structure and denoted as frame P. Recall from the previous section that the pelvis provides the base reference for both the Agile Eye and hip joint; thus, frame P is considered the global reference frame hereafter. The P frame's x, y, and z axes, denoted with subscript 'p', are directed leftward, posteriorly (i.e.

backward), and cranially (i.e. upward) with respect to the human user's body, respectively. Frame F, with origin positioned concentric to the hip joint at $\mathbf{f}$, is fixed to the femur and thereby indicates its spatial orientation with respect to the global frame. Finally, the S frame has its origin, $\mathbf{s}$, positioned at the Agile Eye's centre-of-rotation and is fixed with respect to the Agile Eye's end-effector; this plane therefore provides the Agile Eye's end-effector orientation with respect to the global frame. The SRRP/S mechanism's 'home' configuration is achieved when the correspondent axes of each of the aforementioned frames are pointed in the same directions, as is shown in Figure 5.3. Also, as indicated for frame P, the x, y, and z axes of the F and S frames are differentiated by subscripts 'f' and 's', respectively.

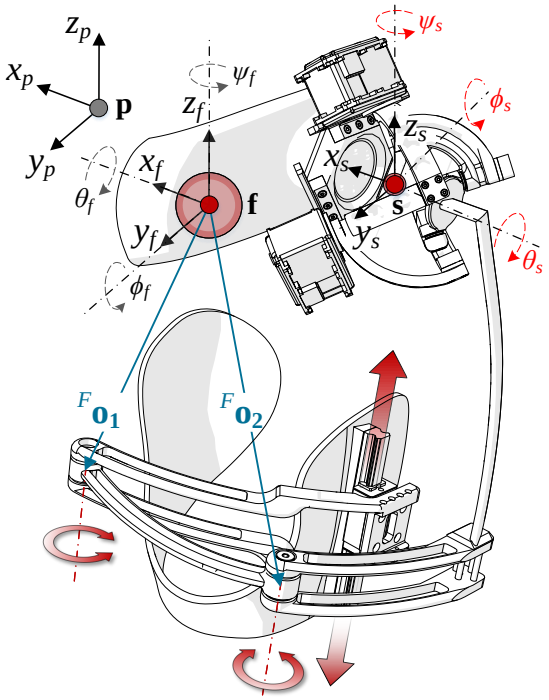

Figure 6.3. Schematic of SRRP/S's posterior side in 'home' configuration

In addition to reference frame notations, it is necessary to denote the positions of the two passive rotary joints located between the Agile Eye and prismatic joint within the SRRP/S mechanism's kinematic chain. As shown in Figure 6.3, the position of the rotary joint directly linked to the prismatic joint is given by $\mathbf{o_1}$ and that directly linked to the Agile Eye's end-effector is given by $\mathbf{o_2}$. Furthermore, upon undergoing the inverse kinematic procedure presented in the next subsection, the reader will find that these rotary joint

positions must be represented with respect to frame F. Therefore, in Figure 5.3, the $\mathbf{o_1}$ and $\mathbf{o_2}$ points are shown as arrowed lines originating from origin **f** and, as a result, are marked with superscript 'F' (see Figure 6.3). This left-side superscript convention for indicating a vector's frame representation is used through the remainder of this paper. Also, note that the positions of the hip joint and active spherical joint (i.e. the Agile Eye's center-of-rotation) have already been established as **f** and **s**, respectively.

Next, naming conventions for frame rotations must be established before the discussion of inverse kinematics analysis begins. In this paper, variables θ, ϕ, and ψ respectively correspond to rotations about a frame's x-axis, y-axis, and z-axis. If the assumed order of rotations is: fixed-frame x-axis rotation, fixed-frame y-axis rotation, and then current-frame z-axis rotation, the associated rotation is marked with an asterisk (i.e. '*'). Alternatively, if the order of rotations follows conventional roll-pitch-yaw parameterization (i.e. fixed-frame x-axis, fixed-frame y-axis, then fixed-frame z-axis rotations), then the associated rotation variable is not marked with an asterisk. Additionally, rotations associated with frame **f** are marked with a 'f' subscript, while rotations corresponding to frame **s** are indicated with a 's' subscript.

6.2.2. Inverse Kinematics

The inverse kinematics problem, as defined in [57], requires that a function for device actuator states be determined in terms of variables that define the spatial orientation of the femur with respect to the pelvis reference frame. Here, these variables are the θ_f, ϕ_f, and ψ_f angles associated with the three rotational DOFs of the hip joint, as introduced in Figure 5.3. One geometrically-based inverse kinematics procedure is presented below in two parts. First, the relationship between the θ_f, ϕ_f, and ψ_f angles and the θ_s, ϕ_s, and ψ_s angles of the Agile Eye's end-effector will be established. Second, the relationship between the Agile Eye's end-effector angles and its active joint input states, which has already been investigated extensively in relevant literature including [22, 23, 25], will be reviewed.

***- Determination of Z_s -Axis Direction Vector*.** An imperative observation to begin our kinematic analysis is that the axis of action for each of the passive joints located between the hip and Agile Eye end-effector are parallel. This design detail geometrically constrains the z_f-axis and z_s-axis to be oriented in the same direction for all system

configurations, as schematically illustrated in Figure 6.4. Therefore, once a desired femur orientation is established, the globally-represented direction vector for the z_s-axis is also established.

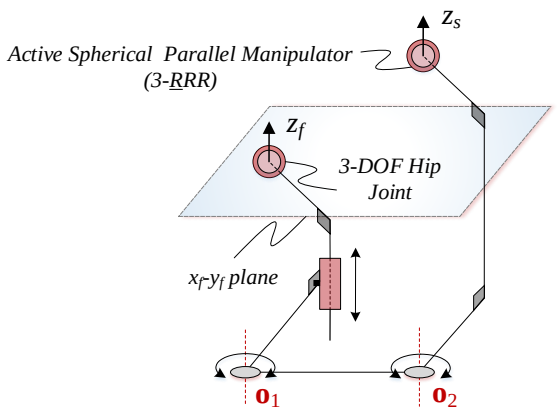

Figure 6.4. Schematic illustration of constraint on z_f and z_x axes

A common method to represent frame orientations is through a three-row by three-column transformation matrix, in which the columns correspond to direction vectors for the frame's axes. In order to relate such a matrix to three rotations in mutually perpendicular directions, a representation scheme and order for the rotations must first be established. As implied by Figure 6.3 and the discussion of rotations in Sec. 6.1, the representation for the θ_f, ϕ_f, and ψ_f angles has been chosen as fixed-frame parameterization with respect to the global P frame. The order of rotations is chosen as θ_f about the x_p-axis first, ϕ_f about the y_p-axis second, and ψ_f about the z_p-axis third (i.e. conventional roll-pitch-yaw representation). Mathematically, the orientation for the F frame, corresponding to the femur, is obtained with respect to the global frame as follows:

$$R_{PF} = R_{z,\psi_f} R_{y,\phi_f} R_{x,\theta_f} \tag{6.1}$$

Because right-hand coordinate frames are used, the terms in the right-hand side of Eq. (6.1) are the basic, single-axis rotation matrices corresponding to the axis indicated in subscript. Therefore, Eq. (6.1) can be expanded into:

$$R_{PF} = \overbrace{\begin{bmatrix} C\phi_f C\psi_f & S\theta_f S\phi_f C\psi_f - C\theta_f S\psi_f & C\theta_f S\phi_f C\psi_f + S\theta_f S\psi_f \\ C\phi_f S\psi_f & S\theta_f S\phi_f S\psi_f + C\theta_f C\psi_f & C\theta_f S\phi_f S\psi_f - S\theta_f C\psi_f \\ -S\phi_f & S\theta_f C\phi_f & C\theta_f C\phi_f \end{bmatrix}}^{\left[{}^P\mathbf{x}_f \quad {}^P\mathbf{y}_f \quad {}^P\mathbf{z}_f\right]} \tag{6.2}$$

where C represents the cosine function and S represents the sine function in this context. In simplified form, Eq. (6.2) can be expressed as:

$$R_{PF} = \begin{bmatrix} r_{11} & r_{12} & r_{13} \\ r_{21} & r_{22} & r_{23} \\ r_{31} & r_{23} & r_{33} \end{bmatrix} \tag{6.3}$$

In addition to providing the direction vectors for the F frame's axes with respect to the global frame, R_{PF} is a transformation matrix that converts a vector's representation from the F frame to the global P frame when pre-multiplied by it. Furthermore, based on the design observation described above, the necessary ${}^P\mathbf{z}_s$ direction vector to achieve the femur orientation indicated by Eq. (6.2) can be obtained directly from the matrix's third column as follows:

$${}^P\mathbf{z}_s = \begin{bmatrix} C\theta_f S\phi_f C\psi_f + S\theta_f S\psi_f \\ C\theta_f S\phi_f S\psi_f - S\theta_f C\psi_f \\ C\theta_f C\phi_f \end{bmatrix} \tag{6.4}$$

***- Redefinition of Frame F Rotation Angles*.** Once the direction vector for the z_s-axis is known with respect to the global frame as per Eq. (6.4), the overall orientation of frame S can be determined as a local rotation about that axis. Here, the term 'local rotation' corresponds to the final current-frame rotation when a frame orientation is represented as two fixed-frame rotations followed by a final current-frame rotation. The fixed-frame rotations occur about the global x and y axes respectively and the final current-frame rotation occurs about the updated z-axis, the F frame's orientation would be expressed as:

$$R_{PF} = R_{y,\phi_f^*} R_{x,\theta_f^*} R_{z,\psi_f^*}$$

$$R_{PF} = \begin{bmatrix} C\theta_f^* C\psi_f^* + S\theta_f^* S\phi_f^* S\psi_f^* & -S\theta_f^* C\psi_f^* + C\theta_f^* S\phi_f^* S\psi_f^* & C\phi_f^* S\psi_f^* \\ S\theta_f^* C\phi_f^* & C\theta_f^* C\phi_f^* & -S\theta_f^* \\ -C\theta_f^* S\psi_f^* + S\theta_f^* S\phi_f^* C\psi_f^* & S\theta_f^* S\psi_f^* + C\theta_f^* S\phi_f^* C\psi_f^* & C\phi_f^* C\psi_f^* \end{bmatrix} \tag{6.5}$$

After grouping and manipulating the terms of R_{PF} in Eq. (6.5), the newly-defined orientation angles can be isolated and expressed in terms of the original roll-pitch-yaw input angles as follows:

$$\theta_f^* = \text{atan2}\left(r_{32}r_{13} - r_{12}r_{33}, r_{11}r_{33} - r_{31}r_{13}\right) \tag{6.6}$$

$$\psi_f^* = \text{atan2}\left(r_{21}r_{32} - r_{31}r_{22}, r_{11}r_{22} - r_{21}r_{12}\right) \tag{6.7}$$

$$\phi_f^* = \text{atan2}\left(r_{11}r_{32} - r_{31}r_{12}, (r_{11}r_{33} - r_{31}r_{13}) / \cos(\theta_f^*)\right) \tag{6.8}$$

When the problem is interpreted as z_s-axis establishment and then a local rotation, the latter portion is geometrically reduced to two dimensions through its evaluation in the x_f–y_f plane (which is always parallel to the x_s–y_s plane), as shown in Figure 6.5. Furthermore, the Agile Eye end-effector's local rotation is composed from two sources. First, the leading two fixed-frame rotations cause the position of point **s** relative to **f** to vary because of the offset between the always-parallel x_f–y_f and x_s–y_s planes (i.e. parallax effect). In turn, the Agile Eye end-effector must rotate with respect to the x_f–y_f plane in order to compensate for this change in relative position. Second, local rotation of the femur (i.e. frame F) acts through the quasi-four-bar-mechanism created by linkages and rotary joints connecting the prismatic joint to the Agile Eye's end-effector to necessitate rotation of the latter. These two distinct stages of motion aid in the SRRP/S mechanism's kinematic analysis, but would not be separately observed in reality.

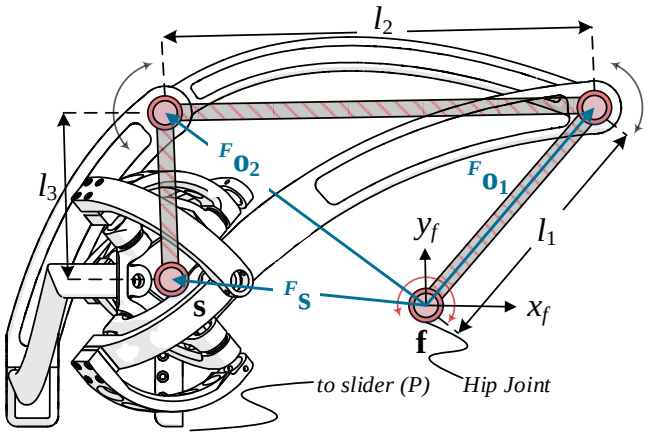

Figure 6.5. Schematic view of SRRP/S device from x_f-y_f plane

- Determination of ζ_1 – Part 1 of Frame S Local z-Rotation. The first source of the Agile Eye end-effector's local rotation is illustrated in Figure 6.6. In the figure, a prime

marking (i.e. ') is used to show updated points or axes after the device undergoes $R_{x,\theta f^*}$ and $R_{y,\phi f^*}$ orientation transformations but not yet the $R_{z,\psi f^*}$ current-frame rotation. As mentioned earlier, these leading two fixed-frame rotations cause the position of point **s** to change within the F frame. Consequentially, the position of rotary joint $\mathbf{o}_2$ projected onto the x_f–y_f plane also shifts.

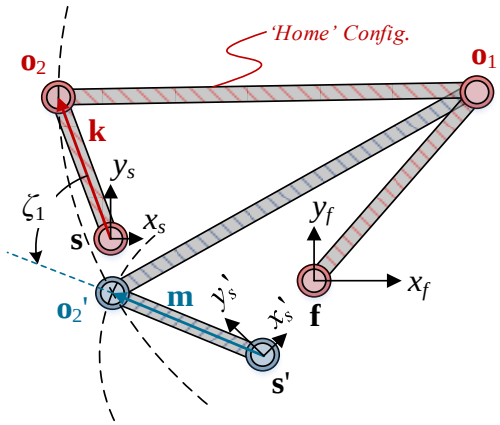

Figure 6.6. x_f-y_f plane view of device after $\mathbf{R}_{x,\theta^*}$ and $\mathbf{R}_{y,\theta^*}$ rotations

In terms of inverse kinematics procedure, a desired orientation for frame F is known, and the global position of point **s** is fixed; that is:

$$^{P}\mathbf{s} = \begin{bmatrix} ^{P}s_x & ^{P}s_y & ^{P}s_z \end{bmatrix}^T \tag{6.9}$$

where the scalar coordinates $^{P}s_x$, $^{P}s_y$, and $^{P}s_z$ are constants. Therefore, it is readily possible to express point **s** in terms of frame F after the leading two fixed-frame rotations by employing the transpose of the corresponding transformation matrices given in Eq. (6.5):

$$^{F}\mathbf{s}' = \begin{bmatrix} ^{F}s_x' & ^{F}s_y' & ^{F}s_z' \end{bmatrix}^T = \left(R_{y,\phi_f^*} R_{x,\theta_f^*} \right)^T {}^{P}\mathbf{s} \tag{6.10}$$

Next, our SRRP/S device design and reference frame definitions ensure that the x- and y-coordinates of rotary joint position $\mathbf{o}_1$ remain fixed when represented in frame F:

$$^{F}\mathbf{o}_1 = \begin{bmatrix} ^{F}o_{1x} & ^{F}o_{1y} & ^{F}o_{1z} \end{bmatrix}^T \tag{6.11}$$

where $^{F}o_{1x}$ and $^{F}o_{1y}$ are constants. Note that the z-coordinate varies because of the prismatic joint's single degree-of-freedom. Eqs. (6.10) and Eq. (6.11) fully define the 2D positions of points **s** and $\mathbf{o}_1$ in the x_f–y_f plane after the leading two fixed-frame rotations;

now it is possible to determine the planar position of $\mathbf{o}_2'$ as the point of intersection between circles centered at points $\mathbf{o}_1$ and $\mathbf{s}'$. These circles have respective radii of l_2 and l_3, as per Figure 6.5, due to the geometrical constraints imposed by the device's corresponding rigid linkages. It follows that a basic evaluation of the intersection between the two circle's equations results determination of x- and y-coordinates for ${}^F\mathbf{o}_2'$:

$$ {}^F o_{2x}' = \frac{-b_1 - \sqrt{b_1^2 - 4a_1c_1}}{2a_1} \tag{6.12} $$

$$ {}^F o_{2y}' = A_1\left({}^F o_{2x}'\right) + B_1 \tag{6.13} $$

where Eqs. (6.14–18) define the complete expressions for which the A_1, B_1, a_1, b_1, and c_1 variables are substituted. Note the lesser quadratic root is chosen in Eq. (6.12) because our design decisions and frame definitions require that the true ${}^F\mathbf{o}_2'$ position must always have the more negative x-coordinate value.

$$ A_1 = \left({}^F o_{1x} - {}^F s_x'\right) \Big/ \left({}^F s_y' - {}^F o_{1y}\right) \tag{6.14} $$

$$ B_1 = \frac{l_4^2 + \left({}^F s_x'\right)^2 + \left({}^F s_y'\right)^2 - l_1^2 - {}^F o_{1x}^2 - {}^F o_{1y}^2}{2\left({}^F s_y' - {}^F o_{1y}\right)} \tag{6.15} $$

$$ a_1 = A_1^2 + 1 \tag{6.16} $$

$$ b_1 = 2\left(A_1 B_1 - {}^F o_{1x} - A_1({}^F o_{1y})\right) \tag{6.17} $$

$$ c_1 = {}^F o_{1x}^2 + B_1^2 - 2B_1({}^F o_{1y}^2) + {}^F o_{1y}^2 - l_2^2 \tag{6.18} $$

Now, the first component of the S frame's local z-axis rotation is determined as the angle between the 'home' state of linkage l_3 and its angular state after the first two fixed-frame rotations. This is shown as ζ_1 in Figure 6.6. Mathematically, the angle can be determined as that between vector $\mathbf{k}$, which points from point $\mathbf{s}$ to point $\mathbf{o}_2$ when the device is in its 'home' configuration, and vector $\mathbf{m}$, which points from $\mathbf{s}'$ to $\mathbf{o}_2'$:

$$ {}^F\mathbf{k} = {}^F\mathbf{o}_2\Big|_{R_{PF}=I_3} - {}^F\mathbf{s}\Big|_{R_{PF}=I_3} = \begin{bmatrix} {}^F k_x & {}^F k_y \end{bmatrix}^T \tag{6.19} $$

$$ {}^F\mathbf{m} = {}^F\mathbf{o}_2' - {}^F\mathbf{s}' = \begin{bmatrix} {}^F m_x & {}^F m_y \end{bmatrix}^T \tag{6.20} $$

From Eqs. (6.19) and (6.20), it follows that ζ_1 can be determined as:

$$\zeta_1 = \operatorname{atan2}\left(C_1, C_2\right) \tag{6.21}$$

where C_1 and C_2 are given by:

$$C_1 = \frac{{}^F m_y - {}^F m_x \, {}^F k_y / {}^F k_x}{\left({}^F k_x^2 + {}^F k_y^2\right) / {}^F k_x} \tag{6.22}$$

$$C_2 = \left({}^F m_x + \frac{{}^F m_y - {}^F m_x \, {}^F k_y / {}^F k_x}{\left({}^F k_x^2 + {}^F k_y^2\right) / {}^F k_x} \right) / {}^F k_x \tag{6.23}$$

- Determination of ζ_2 – Part 2 of Frame S Local z-Rotation. The final current-frame rotation about the updated z_f-axis places the F frame in its final desired orientation. Upon evaluating the device's response to this rotation, a frame F rotation would further reposition $\mathbf{s}$ in terms of frame F. Equivalently and perhaps more easily understood, this rotation can be expressed as a rotation of point $\mathbf{o}_1$ about the F frame origin with the $\mathbf{s}'$ point remaining unchanged. This latter interpretation is illustrated in Figure 6.7. Recall that ψ_f^* is determined in Eq. (6.7).

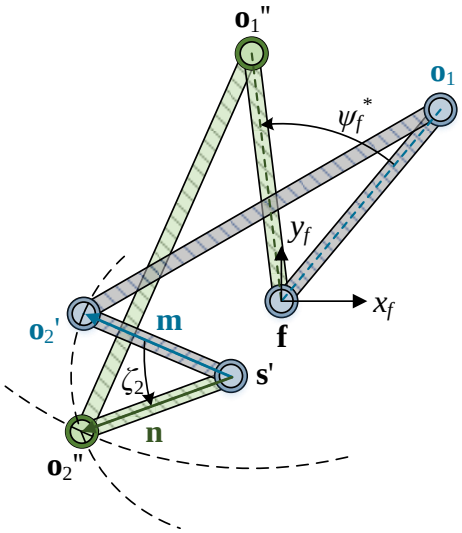

Figure 6.7. x_f plane view of device after ψ_f^* rotation applied to $\mathbf{o}_1$

It follows from the figure that the updated position for point ${}^F\mathbf{o}_1$, denoted with a double-prime marking (i.e. "), can be determined by applying a z-axis rotation of magnitude ψ_f^* to its original position:

$$ {}^{F}\mathbf{o}_1'' = \begin{bmatrix} C\psi_f^* & -S\psi_f^* & 0 \\ S\psi_f^* & C\psi_f^* & 0 \\ 0 & 0 & 1 \end{bmatrix} {}^{F}\mathbf{o}_1 \tag{6.24} $$

As mentioned in Sec. 6.2, Eq. (6.11), the x- and y-coordinates of ${}^{F}\mathbf{o}_1$ are constant, while its z-coordinate varies with the prismatic joint's motion. In the analysis to follow, only the known x- and y-coordinates of ${}^{F}\mathbf{o}_1''$ are required, so the z- coordinate in Eq. (6.24) can be ignored. The ${}^{F}\mathbf{o}_1''$ point should be considered as distinct from ${}^{F}\mathbf{o}_1''$ for this analysis method; they identify relative positions for the same rotary joint at different stages of motion (not occurring separately in actuality).

Next, the updated location of point ${}^{F}\mathbf{o}_2$ within the configuration state shown in Figure 6.7 must be determined; it is also marked with a double-prime for the sake of clarity. As before, this can be achieved by finding the x_f–y_f plane intersection of two circles: one of radius l_2 centred at ${}^{F}\mathbf{o}_1''$ and the other or radius l_3 centred at ${}^{F}\mathbf{s}'$. Taking the solution associated with the lesser x-coordinate value due to design and frame definition decisions, the results are given in the following equations:

$$ {}^{F}o_{2x}'' = \frac{-b_2 - \sqrt{b_2^{\,2} - 4a_2c_2}}{2a_2} \tag{6.25} $$

$$ {}^{F}o_{2y}'' = A_2\left({}^{F}o_{2x}''\right) + B_2 \tag{6.26} $$

where Eqs. (6.27–6.31) define the substitution variables therein.

$$ A_2 = \left({}^{F}o_{1x}'' - {}^{F}s_x'\right) \Big/ \left({}^{F}s_y' - {}^{F}o_{1y}''\right) \tag{6.27} $$

$$ B_2 = \frac{l_4^2 + \left({}^{F}s_x'\right)^2 + \left({}^{F}s_y'\right)^2 - l_1^2 - \left({}^{F}o_{1x}''\right)^2 - \left({}^{F}o_{1y}''\right)^2}{2\left({}^{F}s_y' - {}^{F}o_{1y}''\right)} \tag{6.28} $$

$$ a_2 = A_2^{\,2} + 1 \tag{6.29} $$

$$ b_2 = 2\left(A_2B_2 - {}^{F}o_{1x}'' - A_2\left({}^{F}o_{1y}''\right)\right) \tag{6.30} $$

$$ c_2 = \left({}^{F}o_{1x}''\right)^2 + B_2^{\,2} - 2B_2\left({}^{F}o_{1y}''\right)^2 + \left({}^{F}o_{1y}''\right)^2 - l_2^2 \tag{6.31} $$

Now, the second component of the S frame's local z-axis rotation is evaluated as the angle between previously established vector $\mathbf{m}$ and an updated vector $\mathbf{n}$, pointing from ${}^{F}\mathbf{s}'$ to ${}^{F}\mathbf{o}_2''$:

$$ {}^{F}\mathbf{n} = {}^{F}\mathbf{o}_2'' - {}^{F}\mathbf{s}' = \begin{bmatrix} {}^{F}n_x & {}^{F}n_y \end{bmatrix}^T \tag{6.32} $$

The angle between the two vectors is represented by ζ_2 and is determined as:

$$\zeta_2 = \operatorname{atan2}\left(C_3, C_4\right) \tag{6.33}$$

where the C_3 and C_4 variables are given by:

$$C_3 = \frac{{}^F n_y - {}^F n_x \, {}^F m_y / {}^F m_x}{\left({}^F m_x^2 + {}^F m_y^2\right) / {}^F m_x} \tag{6.34}$$

$$C_4 = \left({}^F n_x + \frac{{}^F n_y - {}^F n_x \, {}^F m_y / {}^F m_x}{\left({}^F m_x^2 + {}^F m_y^2\right) / {}^F m_x} \right) / {}^F m_x \tag{6.35}$$

The overall local rotation of the S frame about its z-axis is finally taken as the sum of the ζ_1 and ζ_2 angles:

$$\psi_s^* = \zeta_1 + \zeta_2 \tag{6.36}$$

It follows that the orientation of frame S with respect to the global frame can be determined as an ordered multiplication of rotation matrices. The ζ_1 and ζ_2 angles are derived with respect to the orientation of frame F after its leading two fixed-frame rotations, so the orientation of frame S begins with the same two fixed-frame rotations. Subsequently, ψ_s^* represents the final current-frame z-axis rotation for frame S. Altogether, the transformation matrix providing the S frame's orientation with respect to the global frame is:

$$R_{PS} = R_{y,\theta_f^*} R_{x,\phi_f^*} R_{z,\psi_s^*} = \begin{bmatrix} q_{11} & q_{12} & q_{13} \\ q_{21} & q_{22} & q_{23} \\ q_{31} & q_{32} & q_{33} \end{bmatrix} \tag{6.37}$$

For completeness, it is important to represent the orientation given in Eq. (6.37) as angles associated with conventional roll-pitch-yaw form (i.e. angles corresponding to ordered x-axis, y-axis, then z-axis fixed frame rotations). These are determined via appropriate grouping and manipulation of the matrix's terms:

$$\psi_s = \operatorname{atan2}\left(q_{21}q_{13} - q_{11}q_{23}, q_{11}q_{22} - q_{21}q_{12}\right) \tag{6.38}$$

$$\phi_s = \operatorname{atan2}\left(q_{32}q_{13} - q_{12}q_{33}, q_{22}q_{33} - q_{23}q_{32}\right) \tag{6.39}$$

$$\theta_s = \operatorname{atan2}\left(q_{22}q_{13} - q_{12}q_{23}, (q_{11}q_{22} - q_{21}q_{12}) / \cos(\psi_s)\right) \tag{6.40}$$

where Eqs. (6.38–6.40) respectively provide roll-pitch-yaw rotation angles about the S frame's z, y, and x axes as illustrated in Figure 6.3 (i.e. $R_{PS} = R_{z,\psi S}R_{y,\phi S}R_{x,\theta S}$).

With the orientation of the Agile Eye's end-effector determined through frame S, the next stage of the inverse kinematics analysis is that of the Agile Eye itself. This analysis has already been examined extensively in several works of literature [22–25, 27]. One approach is briefly revisited here again for the sake of completeness. For this isolated analysis, a new fixed reference frame G is introduced; as shown in Figure 6.8, the new frame's origin lies on the centre-of-rotation of the Agile Eye's end-effector with its z_g-axis perpendicular to and directed away from the plane containing each of the three active joints, identified by $\mathbf{u_1}$, $\mathbf{u_2}$, and $\mathbf{u_3}$ (to be further defined below). Thus, point $\mathbf{s}$ is the origin for both frames S and G. Furthermore, this G frame's y_g-axis is directed towards the active joint identified with subscript '1' when projected into the x_g–y_g plane (i.e. the plane passing through the device's centre-of-rotation and parallel to the plane containing all active joints). It follows that the Agile Eye end-effector's orientation angles with respect to frame *G* are related to those derived in Eqs. (6.38–6.40) as:

$$\psi = -\theta_s \tag{6.41}$$

$$\phi = \psi_s \tag{6.42}$$

$$\theta = -\phi_s \tag{6.43}$$

where ψ, ϕ, and θ represent the rotation angles about the new frame's z_g, y_g, and x_g axes respectively. Vectors $\mathbf{u_1}$, $\mathbf{u_2}$, and $\mathbf{u_3}$ provide directions for the rotational axes of the Agile Eye's three active joints. Because they are positioned at points fixed to the Agile Eye's base structure, these vectors have constant values with respect to the S, G, and global P frames.

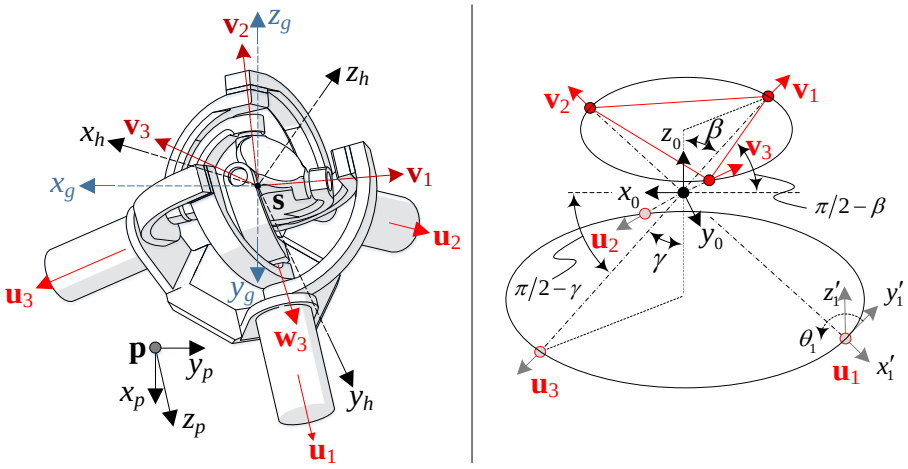

Figure 6.8. Agile eye schematics with parameters and direction vectors labelled

6.2.3. Forward Kinematics

For the sake of completeness, a discussion of the SRRP/S mechanism's forward kinematics procedure is included here. To start, the forward kinematics procedure requires derivation of a relationship between the Agile Eye's active joint states and end-effector orientation, assuming that the former is known and the latter is to be determined [57]. In the interest of focusing on the SRRP/S mechanism's novel components, this initial stage of forward kinematics procedure is not detailed here; the reader may refer to Niyetkaliyev's and Shintemirov's work in [52], where one approach is explored thoroughly. Note that the procedure associated with the Agile Wrist in their work also applies to the Agile Eye, because these are two design embodiments of the same base mechanism: the 3-RRR manipulator.

Thus, our discussion begins with the assumption of an established algorithm for θ_s, ϕ_s, and ψ_s angles in terms of θ_i active joint inputs:

$$\psi_s = g\left(\theta_1, \theta_2, \theta_3\right) \tag{6.44}$$

$$\phi_s = g\left(\theta_1, \theta_2, \theta_3\right) \tag{6.45}$$

$$\theta_s = g\left(\theta_1, \theta_2, \theta_3\right) \tag{6.46}$$

where 'g' signifies a mathematical function in a generalized sense (i.e. the g function may vary for each instance of its use). The succeeding procedure for relating Agile Eye

end-effector orientation to hip orientation ultimately mirrors the inverse kinematics process given in Secs. 6.2.1–6.2.2.

First, the assumedly known values for θ_s, ϕ_s, and ψ_s provides the orientation of the Agile Eye end-effector with respect to the global P frame:

$$R_{PS} = R_{z,\psi_s} R_{y,\phi_s} R_{x,\theta_s} = \begin{bmatrix} q_{11} & q_{12} & q_{13} \\ q_{21} & q_{22} & q_{23} \\ q_{31} & q_{32} & q_{33} \end{bmatrix} \tag{6.47}$$

In accordance with the kinematic constraints imposed by the axes of action of the SRRP/S mechanism's passive joints located between the Agile Eye and hip, the globally represented z-axis of the S frame directly provides that of the hip's F frame:

$${}^{P}\mathbf{z}_f = \begin{bmatrix} q_{13} \\ q_{23} \\ q_{33} \end{bmatrix} \tag{6.48}$$

Next, the orientation information associated with the S frame can be alternatively represented as a composition of fixed-frame x-axis then y-axis rotations, followed by a final current-frame z-axis rotation:

$$R_{PS} = R_{y,\phi_s^*} R_{x,\theta_s^*} R_{z,\psi_s^*} = \begin{bmatrix} q_{11} & q_{12} & q_{13} \\ q_{21} & q_{22} & q_{23} \\ q_{31} & q_{32} & q_{33} \end{bmatrix} \tag{6.49}$$

where the values for θ_s^*, ϕ_s^*, and ψ_s^* can be derived from the grouping and trigonometric evaluation of q_{ij} terms; i and j = 1, 2, 3. It follows that the mechanism can be analyzed in a plane normal to the action axes of passive rotary and prismatic joints between Agile Eye end-effector and hip by considering the leading fixed frame rotations associated with θ_s^* and ϕ_s^*. Specifically considering the x_s-y_s plane after these two transformations, the hip's position relative to the Agile Eye end-effector's centre-of-rotation is computed as:

$${}^{S}\mathbf{f}' = \begin{bmatrix} {}^{S}f_x' & {}^{S}f_y' & {}^{S}f_z' \end{bmatrix}^T = \left(R_{y,\phi_s^*} R_{x,\theta_s^*} \right)^T {}^{P}\mathbf{f} \tag{6.50}$$

where the prime marking (i.e. ') indicates that only the leading two fixed-frame rotations of the end-effector are considered.

Now, the first component of the hip's local z-axis rotation, ξ_1, can be attributed to the newly established relative positioning of $\mathbf{f}'$ and $\mathbf{s}$ in the x_s-y_s plane. Since joint position $\mathbf{o}_2$ is fixed relative to the S frame (see Figure 6.3), the $\mathbf{o}_1'$ position can be readily determined as the intersection point between a circle of radius l_2 centred at $\mathbf{o}_2$ and

another of radius l_1 centered at $\mathbf{f}'$. Note that the intersection of lesser x_s-coordinate value is the correct selection for the parameters and frame definitions established in our design. The value of ξ_1 is then obtained as the angle between the 'home' configuration vector difference (${}^S\mathbf{o}_1 - {}^S\mathbf{f}$) and difference of the preliminarily updated vectors (${}^S\mathbf{o}_1' - {}^S\mathbf{f}'$):

$$\xi_1 = g\left(\left[{}^S\mathbf{o}_1 - {}^S\mathbf{f}\right], \left[{}^S\mathbf{o}_1' - {}^S\mathbf{f}'\right]\right) \tag{6.51}$$

where g again represents a generalized function. Note that Eq. (6.51) should be formulated in such a manner that negative values for ξ_1 can be appropriately differentiated from positive values, similar to Eqs. (6.21–6.23) for ζ_1.

The second component of the hip's local z-axis rotation, represented by ξ_2, can be considered as the result of the S frame's final local z-axis rotation acting through quasi-four-bar-mechanism created by the passive joints connecting the S and F frames. First, if the $\mathbf{f}'$ point is interpreted as fixed during this rotation, the effect of the S frame's local z-axis rotation can instead be considered a repositioning of point $\mathbf{o}_2$ to $\mathbf{o}_2''$:

$${}^S\mathbf{o}_2'' = \begin{bmatrix} C\psi_s^* & -S\psi_s^* & 0 \\ S\psi_s^* & C\psi_s^* & 0 \\ 0 & 0 & 1 \end{bmatrix} {}^S\mathbf{o}_2 \tag{6.52}$$

Again, the double prime marking (i.e. '') specifies that the current-frame z-axis rotation of the S frame is considered at this point in the analysis. As a result of this joint's repositioning, the other passive rotary joint's position must also move from $\mathbf{o}_1'$ to $\mathbf{o}_1''$. The latter position can be determined within the x_s-y_s plane by evaluating the intersection of circles centred at $\mathbf{o}_2''$ and $\mathbf{f}'$, similar to the derivation of ξ_1. Lastly, the value of ξ_2 is obtained as the angle between the vector (${}^S\mathbf{o}_1' - {}^S\mathbf{f}'$) and its updated value of (${}^S\mathbf{o}_1'' - {}^S\mathbf{f}'$):

$$\xi_2 = g\left(\left[{}^S\mathbf{o}_1' - {}^S\mathbf{f}'\right], \left[{}^S\mathbf{o}_1'' - {}^S\mathbf{f}'\right]\right) \tag{6.53}$$

Eq. (6.53) should also be formulated in such a manner that negative values for ξ_2 can be appropriately differentiated from positive values. Finally, the total local z-axis rotation for the frame F, shown as ψ_f^*, is obtained as the sum of ξ_1 and ξ_2. Moreover, the final orientation of the frame F can be obtained as:

$$R_{PF} = \left(R_{y,\theta_s^*} R_{x,\phi_s^*}\right) R_{z,\psi_f^*} = \begin{bmatrix} r_{11} & r_{12} & r_{13} \\ r_{21} & r_{22} & r_{23} \\ r_{31} & r_{32} & r_{33} \end{bmatrix} \tag{6.54}$$

If desired, the terms of R_{PF} can be grouped and trigonometrically evaluated to provide the associated roll-pitch-yaw angles of the hip, visualized as the θ_f, ϕ_f, and ψ_f

angles in Figure 6.3. This completes the forward kinematics procedure for the SRRP/S mechanism, relating known Agile Eye active joint inputs θ_i to the resulting spatial orientation of the hip joint.

6.3. Verification of Kinematic Analysis

The inverse kinematics procedure described in Sec. 6.2 was verified by a series of simulations using a fully-articulated SolidWorks 3D model of the SRRP/S mechanism, virtual actuators, and a virtual inertial measurement unit (IMU). Table 6.1 presents the pertinent design parameters employed on the 3D model. For the first simulation, the virtual actuator's control signals were derived from a desired hip joint orientation signal via our inverse kinematics algorithm. The resulting orientation signal of the model hip joint was then captured using the virtual IMU and compared to the original, desired orientation signal. Figure 6.9 shows overlaid plots of the desired and virtually-measured signals corresponding to the hip joint's orientation during normal gait cycles; these gait signals are provided by Stanford University's OpenSim software [29, 30]. The software used to complete this task was a synthesis of SolidWorks, Simulink, and SimMechanics.

Table 6.1. Device parameters used for simulations

Parameter (i.e. for $i, j = 1, 2, 3$)	**Value**
Position of 3-RRR centre-of-rotation, ${}^{P}\mathbf{s}$	[-115.6 0 138.2] mm
Linkage l_3 vector in F frame, ${}^{F}\mathbf{k}$	[-23 104]
Length of linkage l_3, $\|{}^{F}\mathbf{k}\|$	106.51m
Position of rotary joint 1 in F frame, ${}^{F}\mathbf{o}_1$	[61.5 106.5]mm
Coupler link length, l_2	200.25 mm

The second set of simulations tests the inverse kinematics accuracy during the hip's flexion/extension, abduction/adduction, and internal/external rotation motions in isolation from each other. Figure 6.10 presents overlay plots of control and virtual response signals corresponding to sine wave motions in each isolated DOF of the hip. The amplitudes for each motion were selected to approximately match the largest amplitudes experienced during normal gait cycles. Furthermore, Figure 6.10 shows the error distribution associated with the two motions set to constant zero values.

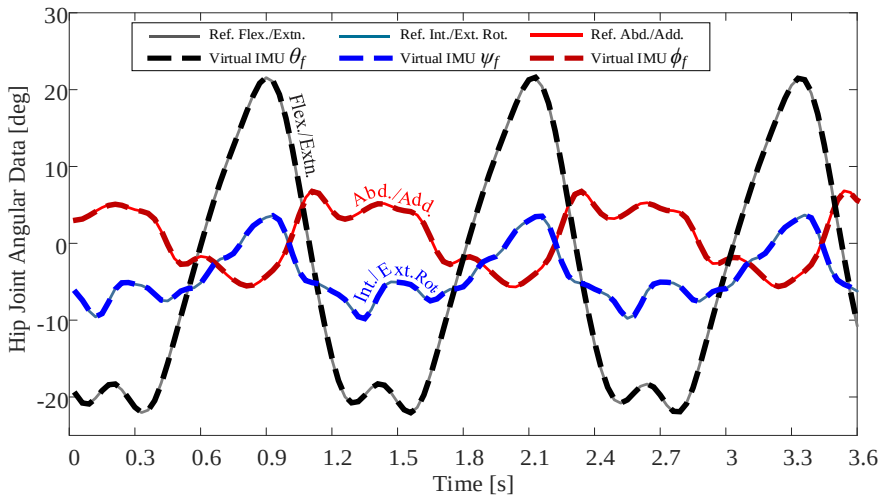

Figure 6.9. Overlay plots of desired and virtually-measured 3-DOF hip joint angles associated with normal gait cycles

The general agreement between the control signals and virtual response of the simulated hip joint as shown in Figure 6.9 and 6.10 suggests the validity of the inverse kinematics procedure described in this paper. The error box plots of Figure 6.10 suggest that the maximum error associated with motions prescribed to zero is less than 1.5 degrees, and that internal/external rotation motions tend to cause less error in the other hip DOFs when performed in isolation.

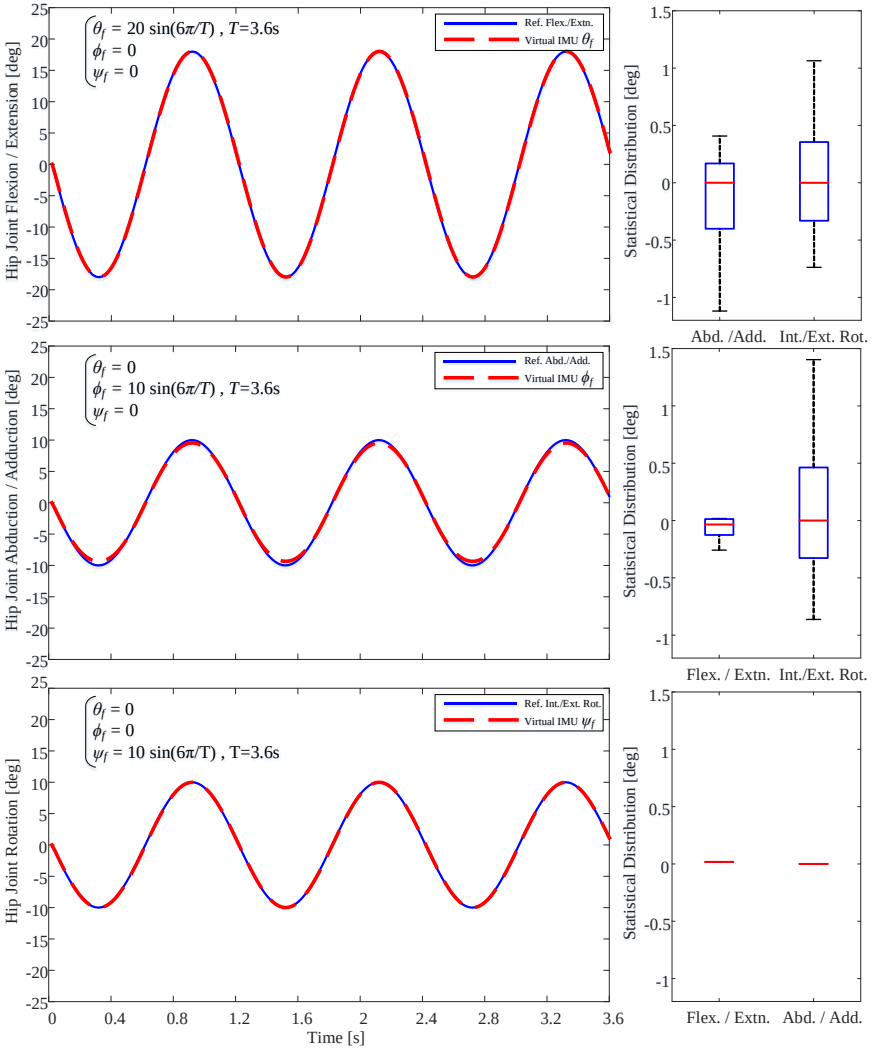

Figure 6.10. Overlay plots of desired and virtually measured 3-DOF hip joint motions and corresponding error boxplots

The complexity of the amalgamated inverse kinematics algorithm resulting from the combination of Eqs. (6.1–6.43) makes it prone to slight computational errors when implemented in practice. This is especially true when the desired motion is not pure yaw (i.e. an isolated signal for ψ_f) because errors associated with the hip's z-axis orientation are propagated through and amplified by the remainder of the algorithm. A potential source of significant error amplification is the quasi-four-bar-mechanism structure composed of the Agile Eye's end-effector, subsequent two passive rotary joints, and hip joint when observed in the x_s-y_s plane or x_f-y_f plane. For the spherical joint positioning application under consideration, it is most appropriate to design the four-bar-mechanism such that input linkage rotations (i.e. the link characterized by l_3) are not amplified at the

output linkage (i.e. characterized by l_1), thereby minimizing device sensitivity and susceptibility to error amplification.

6.4. Dynamic Simulation on the SRRP/S Mechanism

Figure 6.11 shows simulated torque, velocity, and power curves for the actuators of the SRRP/S mechanism during normal gait cycle motions [35, 36]. These plots were obtained by subjecting a Matlab/SimMechanics simulation model of the SRRP/S mechanism to the lower limb motions experienced by a 75.16 kg person's hip, knee and aknle during normal gait cycle motions, as provided by the OpenSim software, and monitoring motor torques and velocities using virtual sensors. In this simulation study the exoskeleton structure was assumed to be made from an Aluminum material. The mass properties feature of SolidWorks software measured the overall weight of the mechanism including all the bolts and nuts required for assembling the mechanism. As a result, the overall weight of the exoskeleton mechanism was estimated to be 2.9 kg. The maximum magnitude torque, velocity, and power associated with the SRRP/S mechanism are 30 N.m, 1.9 rad/s, and 28.5 W.

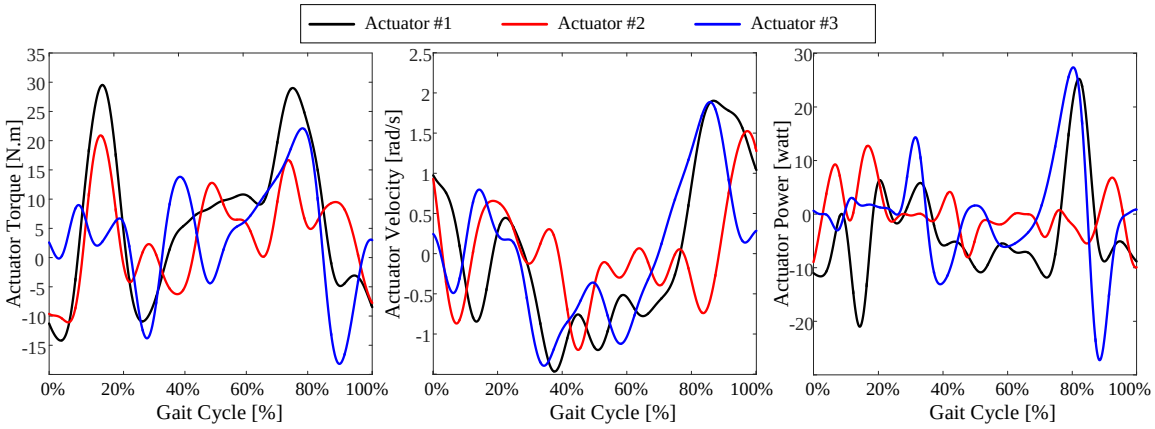

Figure 6.11. Torque, speed, and power required for the SRRP/S device to emulate hip joint motion during normal gait

6.5. Experimental Study on the SRRP/S Mechanism

The simulation results of Sec. 6.3 provide useful insight on the correctness of the inverse kinematics algorithm derived in this study. However, they do not account for

possible practical issues, including but not limited to: design imperfections introduced during fabrication, mechanical interferences, etc. Therefore, a physical prototype of the SRRP/S was constructed to facilitate experimental data collections that would further validate our kinematic analysis and the mechanism's practical performance. The following sections discuss the fabrication method employed and experimental results obtained.

6.5.1. Mechanism Fabrication Details

The prototype mechanism is composed of two main parts: an exoskeleton structure that embodies the SRRP kinematic architecture and a dummy structure that embodies the passive spherical joint targeted for motion assistance. The exoskeleton's pelvis and femur orthotic parts are produced from a 3D printer. The remaining structural components of the exoskeleton are fabricated from aluminum using a CNC machine. Additionally, the exoskeleton's passive joint components are realized as off-the-shelf parts; meanwhile, the active 1-DOF rotary joints are realized as Maxon DCX32L DC motors with ENX16 absolute encoders, each controlled by an EPOS2 50/5 Positioning Controller. Next, the dummy structure is actualized as a mannequin with a modified hip joint. The primary modification made to the mannequin is the installation of a ball-and-socket joint at its hip to facilitate realistic 3-DOF rotational motion capability of the femur with respect to the pelvis. The complete SRRP/S mechanism is constructed such that the parameters given in Table 6.1 remain applicable. Figure 6.12 shows a photograph of the physical prototype along with two views of the CAD model from which it is based.

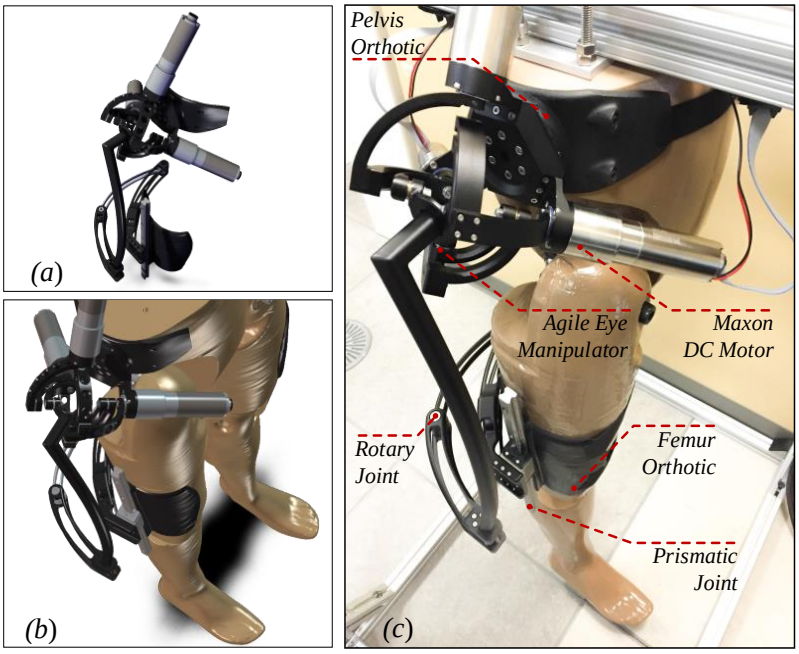

Figure 6.12. a) CAD model of SRRP in isolation, b) CAD model of SRRP/S assembly, and c) photo of physical SRRP/S prototype

6.5.2. Experimental Results

For our experimental study of the SRRP/S mechanism, the same normal gait cycle motion that was used during the simulations (i.e. obtained from OpenSim [29, 30]), was employed as the dummy hip joint's motion control signal. This desired output signal was converted to individual motor signals in real-time via the inverse kinematics algorithm detailed in Sec. 6.2. The aforementioned controller unit was used to control the motors' motions during the tracking task based on feedback from the encoder sensors. Figure 6.12 shows overlaid plots of the reference signal and encoder feedback for each motor during the normal gait tracking experiment. Ultimately, the general agreement between control and feedback signals in these plots suggests that SRRP/S mechanism is physically able to accurately track the motions associated with the human hip joint during normal gait.

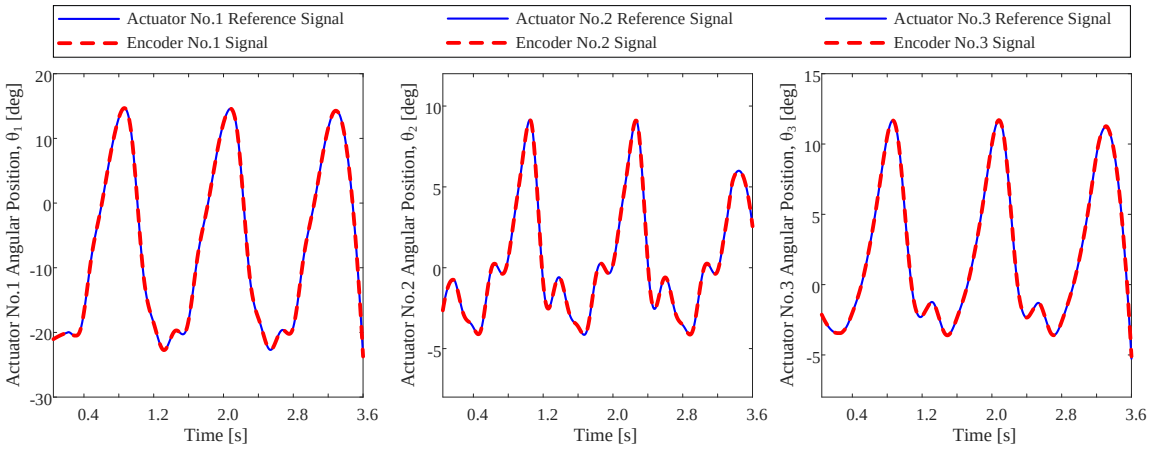

Figure 6.13. Experimentally-acquired control and feedback signals for each SRRP/S motor during normal ait tracking

6.6. Conclusion

This study presented the design, kinematic analysis, simulation, and experimentation of a novel robotic SRRP/S mechanism proposed for application in minimally-intrusive motion assistance for ball-and-socket joints. The design incorporates a subsystem capable of producing active 3-DOF rotational motions, a passive motion-transmission subsystem, and the ball-and-socket joint targeted for motion guidance. For our proposed design, the active spherical joint is realized by the well-established Agile Eye parallel manipulator; motion-transmission is accomplished using carefully-positioned, serially-connected passive rotary and prismatic joints. Overall, the coordinated motions of these subsystems enable our design with the novel capability to convey fully defined kinematic motions to the targeted spherical joint.

This study's kinematic analysis details one geometrically-based approach to solving both the inverse and forward kinematics problems. Both of these mathematical processes have been previously documented for the Agile Eye component alone in several other works of literature, while the complete SRRP/S mechanism's kinematic analysis is novel. Beyond the Agile Eye manipulator, the kinematic analysis procedure can be summarized for both the inverse and forward problems as: first asserting the mechanical constraint that motion-transmission joints' axes of action are parallel, and then determining component rotations about these axes given the spatial constraints associated with the design.

Simulation and experimental evaluations of the mechanism were conducted as a means of validating the kinematic analysis results. These evaluations focus on the specific application of the device as a wearable hip exoskeleton intended to guide spherical motions about human's hip joint. The simulation findings indicate that the SRRP/S mechanism is capable of guiding its passive spherical joint through the same motions that a human hip undergoes during normal gait cycles. Further, the simulations suggest that the mechanism can isolate motion in each of the three rotational degrees-of-freedom associated with the target joint, with error less than $1.5°$ in the either degree-of-freedom meant to be zero (i.e. in order to isolate the third DOF). Additionally, the experimental results demonstrate that the mechanism is physically and practically capable of tracking normal gait cycle motions at the targeted joint. An important realization evoked by the simulation results is that the motion-transmission subsystem's design, which takes the form of a quasi-four-bar-mechanism, can significantly increase mechanism sensitivity for certain design parameter selections. As such, future work includes the optimization of the motion-transmission joint positions with the objective of minimizing device sensitivity and, thus, error amplification.

Chapter 7.

Design and Kinematic Analysis of a Hybrid SPRR/S Manipulator for Orientation and Motion Guidance of Spherical Joints

This chapter presents a novel SPRR/S mechanism design, incorporating the well-established Agile Eye, that enables decoupled and orientation guidance of a ball-and-socket or spherical joint. The kinematic architecture associated with the design is described and both inverse and forward kinematic analyses for the complete mechanism are detailed. With focus on hip exoskeleton application, simulation results are presented as verification of the inverse kinematics algorithm. Furthermore, the results obtained from a prototype device during a gait motion experiment are documented as an indication of the device's ability to convey and guide 3-DOF rotational motion to a ball-and-socket joint.

7.1. Mechanical Design of the SPRR/S mechanism

The following subsections respectively describe the mechanical architecture of the SPRR/S mechanism in both a general context and with regard to specific application as a hip exoskeleton device.

7.1.1. General Schematic Design

Figure 7.1 depicts a mechanical schematic of the mechanism that has been proposed in this chapter. As labelled in the Figure 7.1, the design includes a 3-RRR spherical parallel manipulator composed of three parallel-connected 1-DOF rotary joints, which are designated with 'R'; underlined letters indicate that the associated joint is

active, while joints without underlined labels are passive. In accordance with this labelling convention, the schematic indicates that a passive prismatic joint (designated with ‘P’) is serially attached to the 3-RRR manipulator’s end-effector, followed by two serially-connected passive rotary joints. Finally, the final passive rotary joint connects to the target 3-DOF ball-and-socket or spherical joint, which is labelled with ‘S’. The lack of an underline in the spherical joint’s label confirms that it is assumed to be passive.

As a consequence of this design scheme, a suitable technical name for the proposed mechanism, including the target spherical joint, is (3-RRR)PRR/S. Within the brackets, ‘3-RRR’ represents the three parallel-connected limbs (i.e. Agile Eye), each containing one active and two passive rotary joints; the ‘PRR’ immediately following the closing bracket suggests the series connection of the associated passive joints, and the ending ‘/S’ represents the passive spherical-joint constraint asserted by the target spherical joint on the final prismatic joint in the kinematic chain. Alternatively, the mechanism’s name can be shortened to SPRR/S, because the 3-RRR component effectively represents an active spherical joint.

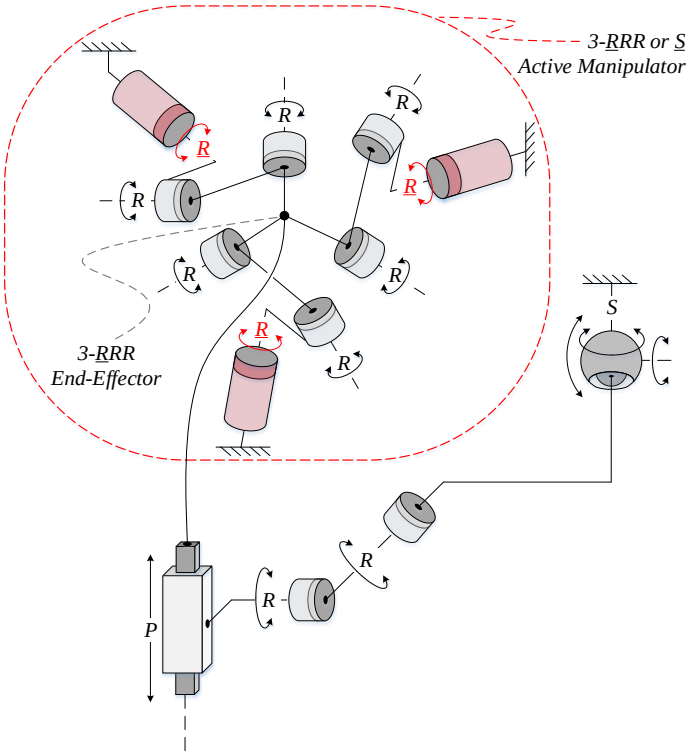

Figure 7.1. Mechanical schematic of the proposed SPRR/S mechanism

7.1.2. Design for Hip Exoskeleton Applications

As stated earlier, one application for the SPRR/S mechanism is its embodiment as a hip exoskeleton attached to the human body. For this particular application, the spherical joint targeted for orientation guidance is the human hip joint. Consequently, the body's pelvis, hip joint, and femur are all included within the mechanical structure of the mechanism. In this mechanism the pelvis serves as the base reference to which each active joint in the 3-RRR manipulator as well as the socket for the hip joint are rigidly connected. In our design, the 3-RRR manipulator takes the form of an Agile Eye oriented sideways with its base structure attached to a 'pelvis orthotic', which in turn attaches to the user's pelvis. These connections are clarified by the design illustration in Figure 7.2. It is assumed that the Agile Eye's base plane containing all three active rotational joint positions is always parallel to the body's sagittal plane.

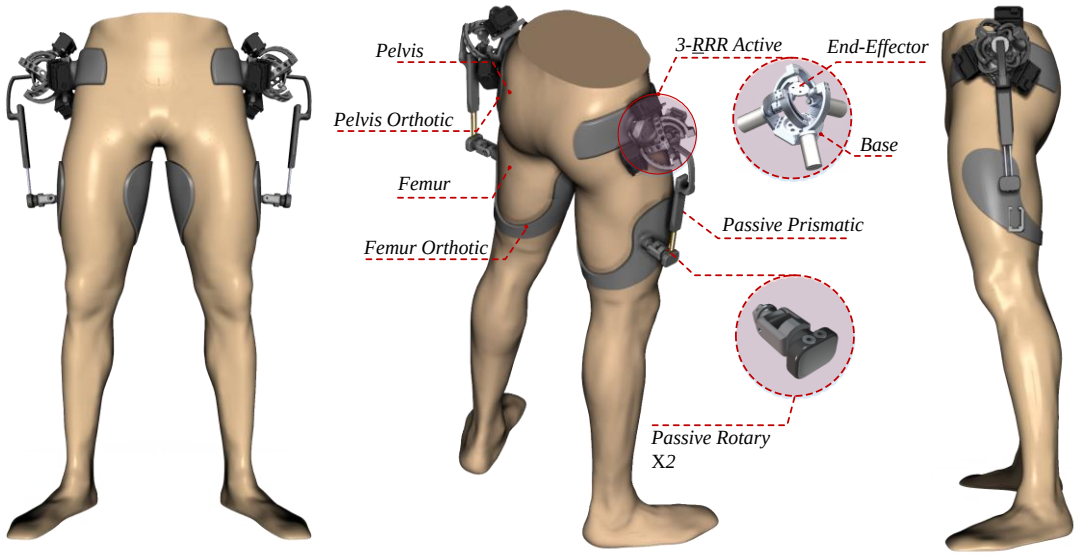

Figure 7.2. Mechanical design of the SPRR/S as a hip exoskeleton

Within this hip exoskeleton design, it is assumed that the human femur bone connects rigidly to the passively rotating ball of the hip's ball-and-socket structure. The SPRR/S mechanism's final rotary joint along its kinematic chain then achieves a fixed position with respect to the femur through attachment to the external surface of the upper leg via a 'femur orthotic', as shown in Figure 7.2. The two passive joints located between the Agile Eye and final rotary joint (i.e. one rotary and one prismatic) are positioned beside the upper leg by way of rigid linkages extending down from the Agile Eye. The coordinated actions of the active rotary joints within the Agile Eye device cause

its end-effector, and consequentially the rigidly attached passive prismatic joint, to rotate in one or a combination of three mutually-perpendicular directions about a center-of-rotation point; this point is located between the Agile Eye's base and end-effector structures. The kinematic constraints associated with the passive rotary joints subsequently convey a unique orientation to the hip joint (i.e. the femur relative to the pelvis) for every configuration of the Agile Eye within its practical workspace. Therefore, decoupled flexion/extension, abduction/adduction, and internal/external rotation motions can be transmitted to the user's hip joint by controlled actuations of the Agile Eye's active joint inputs. The relationship between the desired hip orientation output and the required corresponding angular states of the active joint inputs can be determined through inverse kinematics analysis of the mechanism. Such an analysis is included in the following section.

7.2. Kinematic Analysis of the SPRR/S Mechanism

In the following subsections, a system of parameter and reference frame notations is introduced before both inverse and forward kinematic analyses for the SPRR/S mechanism are detailed.

7.2.1. Notation for Reference Frames, Joints and Motions

The geometrical schematic of Figure 7.3 shows three important reference frames associated with the SPRR/S mechanism that is used during the first stage of kinematic analyses beginning in the next subsection. The first of these frames, with origin position denoted by vector $\mathbf{p}$, is fixed to the user's pelvis structure and denoted as frame P. Recall from the previous section that the pelvis provides the base reference for both the Agile Eye and hip joint; thus, frame *P* is considered the global reference frame hereafter. The P frame's x, y, and z axes, denoted with subscript 'p', are directed leftward, posteriorly (i.e. backward), and cranially (i.e. upward) with regard to the human user's body, respectively. Frame F, with origin positioned concentric to the hip joint at $\mathbf{f}$, is fixed to the femur and thereby indicates its spatial orientation with respect to the global frame. Finally, the S frame has its origin, $\mathbf{s}$, positioned at the Agile Eye's centre-of-rotation and is fixed with respect to the Agile Eye's end-effector; this plane therefore provides the Agile

Eye's end-effector orientation with respect to the global frame. The SPRR/S mechanism's 'home' configuration is achieved when the correspondent axes of each of the aforementioned frames are pointed in the same directions, as is shown in Figure 7.3. Also, the x, y, and z axes of the F and S frames are differentiated by subscripts 'f' and 's', respectively.

In addition to reference frame notations, it is necessary to denote positions associated with the two passive rotary joints located between the Agile Eye and prismatic joint within the SPRR/S mechanism's kinematic chain. As shown in Figure 7.3, the position of the rotary joint directly linked to the femur orthotic is given by $\mathbf{o}_1$. Next, $\mathbf{o}_2$ is located at the intersection of the adjacent passive rotary joint's axis of action and an axis parallel to the prismatic joint's axis of action that passes through **s**. Furthermore, upon undergoing the inverse kinematic procedure presented in the next subsection, the reader will find that these rotary joint positions must be represented with respect to frame F. Therefore, within Figure 7.3, the $\mathbf{o}_1$ and $\mathbf{o}_2$ points are shown as arrowed lines originating from origin **f** and, as a result, are marked with superscript 'F' (see Figure 7.3). This left-side superscript convention for indicating a vector's frame representation is used through the remainder of this paper. Also, note that the positions of the hip joint and active spherical joint (i.e. the Agile Eye's center-of-rotation) have already been established as **f** and **s** respectively.

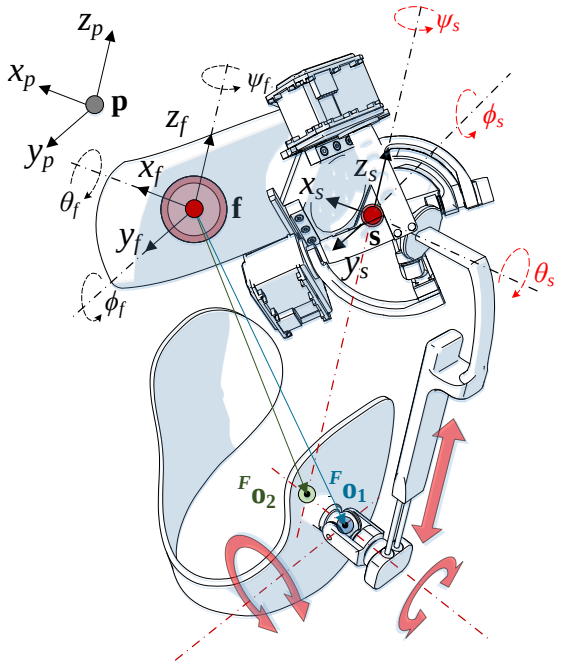

Figure 7.3. Geometrical schematic of SPRR/S's posterior side in 'home' configuration

Naming conventions for frame rotations must also be established before the discussion of inverse kinematics analysis begins. In this paper, variables θ, ϕ, and ψ respectively correspond to rotations about a frame's x-axis, y-axis, and z-axis. If the assumed order of rotations is: fixed-frame x-axis rotation, fixed-frame y-axis rotation, and then current-frame z-axis rotation, the associated rotation is marked with an asterisk (i.e. '*'). Alternatively, if the order of rotations follows conventional roll-pitch-yaw parameterization (i.e. fixed-frame x-axis, fixed-frame y-axis, then fixed-frame z-axis rotations), then the associated rotation variable is not marked with an asterisk. Additionally, rotations associated with frame **f** are marked with a 'f' subscript, while rotations corresponding to frame **s** are indicated with a 's' subscript.

The second stage of inverse kinematics evaluations focuses on the Agile Eye mechanism, which is schematized in Figure 7.4 with frames and joint positions labelled. For this isolated analysis, a new fixed reference frame G is introduced; this new frame's origin lies on the centre-of-rotation of the Agile Eye's end-effector with its z_g-axis perpendicular to and directed away from the plane containing each of the three active joints, identified by $\mathbf{u}_1$, $\mathbf{u}_2$, and $\mathbf{u}_3$ (to be further defined below). Thus, point **s** is the origin for both frames S and G. Furthermore, this G frame's y_g-axis is directed towards the active joint identified with subscript '1' when projected into the x_g–y_g plane (i.e. the plane

passing through the device's centre-of-rotation and parallel to the plane containing all active joints).

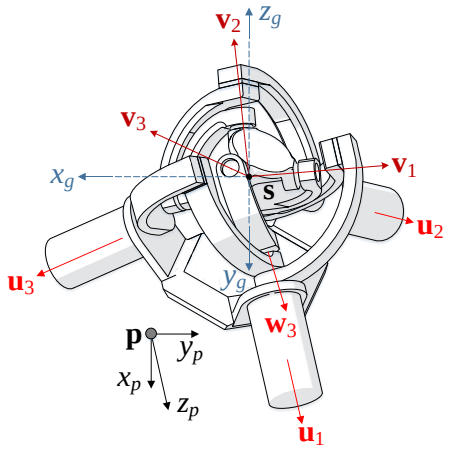

Figure 7.4. Agile Eye schematic with the direction vectors labelled

7.2.2. Inverse Kinematics

The inverse kinematics problem, as defined in [57], requires that a function for device actuator states be determined in terms of variables that define the spatial orientation of the femur with respect to the pelvis reference frame. Here, these variables are the θ_f, ϕ_f, and ψ_f angles associated with the three rotational DOFs of the hip joint, as introduced Figure 7.3. One geometrically-based inverse kinematics procedure is presented below in two parts. First, the relationship between the θ_f, ϕ_f, and ψ_f angles and the θ_s, ϕ_s, and ψ_s angles of the Agile Eye's end-effector will be established. Second, the relationship between the Agile Eye's end-effector angles and its active joint input states, which has already been investigated extensively in relevant literature including [22, 23, 25], will be reviewed.

- Orientation of Frame S with respect to Frame P. To start, the chosen relationship between rotations and frame rotations is formalized. A common method to represent frame orientations is through a three-row by three-column transformation matrix, in which the columns correspond to direction vectors for the frame's axes. In order to relate such a matrix to three rotations in mutually perpendicular directions, a representation scheme and order for the rotations must first be established.

As implied by Figure 7.3 and the discussion of rotations in Sec. 7.1, the representation for the θ_f, ϕ_f, and ψ_f angles has been chosen as fixed-frame parameterization with

respect to the global P frame. The order of rotations is chosen as θ_f about the x_p-axis first, ϕ_f about the y_p-axis second, and ψ_f about the z_p-axis third (i.e. conventional roll-pitch-yaw representation). Mathematically, the orientation for the F frame, corresponding to the femur, is obtained with respect to the global frame as follows:

$$R_{PF} = R_{z,\psi_f} R_{y,\phi_f} R_{x,\theta_f} \tag{7.1}$$

Because right-hand coordinate frames are used, the terms in the right-hand side of Eq. (7.1) are the basic, single-axis rotation matrices corresponding to the axis indicated in subscript. Therefore, Eq. (7.1) can be expanded into:

$$R_{PF} = \overbrace{\begin{bmatrix} C\phi_f C\psi_f & S\theta_f S\phi_f C\psi_f - C\theta_f S\psi_f & C\theta_f S\phi_f C\psi_f + S\theta_f S\psi_f \\ C\phi_f S\psi_f & S\theta_f S\phi_f S\psi_f + C\theta_f C\psi_f & C\theta_f S\phi_f S\psi_f - S\theta_f C\psi_f \\ -S\phi_f & S\theta_f C\phi_f & C\theta_f C\phi_f \end{bmatrix}}^{\left[{}^P\mathbf{x}_f \quad {}^P\mathbf{y}_f \quad {}^P\mathbf{z}_f \right]} \tag{7.2}$$

where C represents the cosine function and S represents the sine function in this context. Now, as a preliminary computation, the coordinates of vector $\mathbf{s}$ expressed in frame F can be determined:

$${}^F\mathbf{s} = R_{PF}^T {}^P\mathbf{s} \tag{7.3}$$

where the superscript 'T' indicates the matrix transpose and ${}^P\mathbf{s}$ is a constant vector because the Agile Eye's centre-of-rotation remains fixed with regard to frame P. With vector $\mathbf{s}$ established in terms of frame F, the system is now observed from the y_f–z_f plane. Such a view of the exoskeleton is schematized in Figure 7.5.

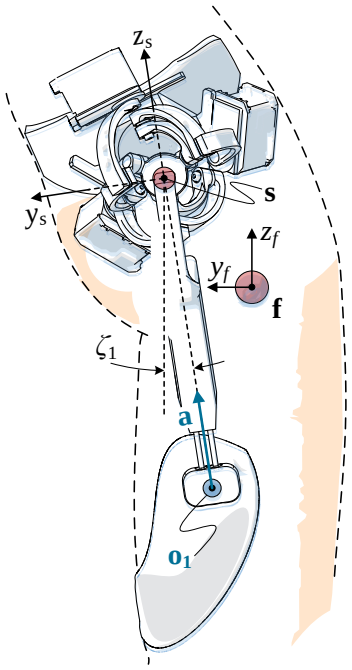

Figure 7.5. Schematic view of SPRR/S device from y_f–z_f plane

The position of $\mathbf{o_1}$ is constant with respect to frame F because it is associated with the passive rotary joint affixed to the femur orthotic. Using ${}^{F}\mathbf{o_1}$ the newly determined ${}^{F}\mathbf{s}$ vector, the direction of the z_s-axis in the y_f–z_f plane can be found as:

$$\mathbf{a} = \frac{{}^{F}\mathbf{s} - {}^{F}\mathbf{o}_1}{\left\| {}^{F}\mathbf{s} - {}^{F}\mathbf{o}_1 \right\|} = \begin{bmatrix} a_x & a_y & a_z \end{bmatrix}^T \tag{7.4}$$

for which the a_x component is meaningless. The meaningful two-dimensional information of this direction vector can be expressed as a rotation as follows:

$$\zeta_1 = \operatorname{atan2}\left(a_y, a_z\right) \tag{7.5}$$

This is the first of two angles required to specify the orientation of frame S with respect to frame F; only two angles are required because only two rotational DOFs exist (i.e. the passive rotary joints sequentially attached the femur orthotic) between the structures to which these frames are attached. The second of said angles can be determined through observation of the system from the x_f–z_f plane, as depicted in Figure 7.6.

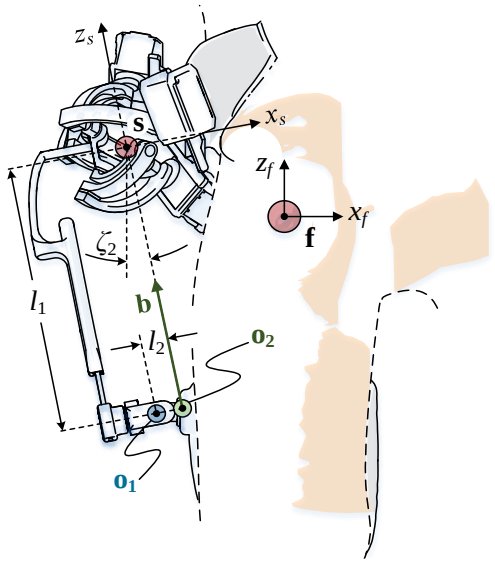

Figure 7.6. Schematic view of SPRR/S device from x_f–z_f plane

As a known design parameter, the Euclidean distance between points $\mathbf{o_1}$ and $\mathbf{o_2}$ is a constant l_2. Therefore, recalling that ${}^F\mathbf{o_1}$ is constant and ${}^F\mathbf{s}$ is given by Eq. 7.3, the planar distance between $\mathbf{o_2}$ and $\mathbf{s}$ can be determined:

$$l_1 = \sqrt{\left\| \begin{bmatrix} {}^F s_x & {}^F s_z \end{bmatrix} - \begin{bmatrix} {}^F o_{1x} & {}^F o_{1z} \end{bmatrix} \right\|^2 - {l_2}^2} \tag{7.6}$$

Next, the ${}^F o_{2x}$ and ${}^F o_{2z}$ vector components can be found at the intersection of two circles within the x_f–z_f plane: the first with radius l_1 centred at ${}^F\mathbf{s}$ and the second with radius l_2 centred at ${}^F\mathbf{o_1}$. Eq. 7.7 and Eq. 7.8 provide the results given by this evaluation of circle intersections:

$${}^F o_{2x} = \frac{-b_1 + \sqrt{{b_1}^2 - 4a_1c_1}}{2a_1} \tag{7.7}$$

$${}^F o_{2z} = A_1\left({}^F o_{2x}\right) + B_1 \tag{7.8}$$

where Eqs. 7.9–7.13 define the complete expressions for the A_1, B_1, a_1, b_1, and c_1 variables. Note the greater quadratic root is chosen in Eq. 7.7 because our design decisions and frame definitions require that the true ${}^F\mathbf{o}_2$ position must always have the more positive x-coordinate value.

$$A_1 = \left({}^F o_{1x} - {}^F s_x\right) \Big/ \left({}^F s_z - {}^F o_{1z}\right) \tag{7.9}$$

$$B_1 = \frac{l_2^2 + \left({}^F s_x\right)^2 + \left({}^F s_z\right)^2 - l_1^2 - {}^F o_{1x}^2 - {}^F o_{1z}^2}{2\left({}^F s_z - {}^F o_{1z}\right)} \tag{7.10}$$

$$a_1 = A_1^2 + 1 \tag{7.11}$$

$$b_1 = 2\left(A_1 B_1 - {}^F o_{1x} - A_1({}^F o_{1z})\right) \tag{7.12}$$

$$c_1 = {}^F o_{1x}^2 + B_1^2 - 2B_1({}^F o_{1z}^2) + {}^F o_{1z}^2 - l_2^2 \tag{7.13}$$

Now, the direction of the z_s-axis in the x_f–z_f plane can be determined as the normalized difference between planar projections of the ${}^F\mathbf{s}$ and ${}^F\mathbf{o}_2$ vectors:

$$\mathbf{b} = \frac{\begin{bmatrix} {}^F s_x & {}^F s_z \end{bmatrix} - \begin{bmatrix} {}^F o_{2x} & {}^F o_{2z} \end{bmatrix}}{\left\| \begin{bmatrix} {}^F s_x & {}^F s_z \end{bmatrix} - \begin{bmatrix} {}^F o_{2x} & {}^F o_{2z} \end{bmatrix} \right\|} = \begin{bmatrix} b_x & b_z \end{bmatrix}^T \tag{7.14}$$

Like before, this direction vector can be expressed as a planar rotation using the atan2 function:

$$\zeta_2 = \text{atan2}\left(-b_x, b_z\right) \tag{7.15}$$

As shown in Figure 7.6, note that the b_x component must be negative by our design and frame definition decisions, so this value is negated in Eq. 7.15.

With both angles required to specify the orientation of frame S with respect to frame F now established, the transformation matrix describing this relative orientation can now be formalized. The transformation matrix is acquired through a rotation about the y_f-axis by $-\zeta_2$ followed by a rotation about the updated x-axis by angle $-\zeta_1$:

$$R_{FS} = R_{y,-\zeta_2} R_{x,-\zeta_1} = \begin{bmatrix} C\zeta_2 & S\zeta_1 S\zeta_2 & -C\zeta_1 S\zeta_2 \\ 0 & C\zeta_1 & S\zeta_1 \\ S\zeta_2 & -S\zeta_1 C\zeta_2 & C\zeta_1 C\zeta_2 \end{bmatrix} = \begin{bmatrix} {}^F\mathbf{x}_s & {}^F\mathbf{y}_s & {}^F\mathbf{z}_s \end{bmatrix} \tag{7.16}$$

where the resulting matrix provides direction vectors of the frame S axes represented in frame F. Note that the rotation angles are negative because their positive values correspond to negative rotations about their associated axes, as depicted in Figure 7.5 and Figure 7.6. Also note that the order of rotations in Eq. 7.16 is significant because it ensures that the x_s-axis remains parallel to the x_f–z_f plane; in physical terms, this represents the physical constraint that the passive prismatic joint cannot rotate about its axis of action.

$$R_{PS} = \begin{bmatrix} R_{PF}{}^{F}\mathbf{x}_s & R_{PF}{}^{F}\mathbf{y}_s & R_{PF}{}^{F}\mathbf{z}_s \end{bmatrix} = \begin{bmatrix} {}^{P}\mathbf{x}_s & {}^{P}\mathbf{y}_s & {}^{P}\mathbf{z}_s \end{bmatrix} \tag{7.17}$$

Finally, the Agile Eye's orientation, as given by frame S, can be expressed in terms of the pelvis reference frame P by pre-multiplying each frame S axis (expressed in frame F) by the R_{PF} transformation matrix developed in Eq. 7.2:

Eq. (17) completes the first stage of inverse kinematics derivation, as it provides a representation of the frame S orientation with respect to frame P.

***- Inverse Kinematics of Agile Eye*.** With the orientation of the Agile Eye's end-effector determined through frame S, the next stage of inverse kinematics analysis is that of the Agile Eye itself. This analysis has already been examined extensively in several works of literature [22–25, 27].

For this stage of inverse kinematics procedure, frame G will be used as the reference, instead of frame P. Therefore, the orientation matrix given in Eq. 7.17 is expressed as angles associated with conventional roll-pitch-yaw form (i.e. angles corresponding to ordered x-axis, y-axis, then z-axis fixed frame rotations). These are determined via appropriate grouping and manipulation of the matrix's terms:

$$\psi_s = \operatorname{atan2}\left(q_{21}q_{13} - q_{11}q_{23}, q_{11}q_{22} - q_{21}q_{12}\right) \tag{7.18}$$

$$\phi_s = \operatorname{atan2}\left(q_{32}q_{13} - q_{12}q_{33}, q_{22}q_{33} - q_{23}q_{32}\right) \tag{7.19}$$

$$\theta_s = \operatorname{atan2}\left(q_{22}q_{13} - q_{12}q_{23}, (q_{11}q_{22} - q_{21}q_{12}) / \cos(\psi_s)\right) \tag{7.20}$$

where

$$R_{PS} = \begin{bmatrix} q_{11} & q_{12} & q_{13} \\ q_{21} & q_{22} & q_{23} \\ q_{31} & q_{32} & q_{33} \end{bmatrix} \tag{7.21}$$

Eqs. 7.18–2.20 respectively provide roll-pitch-yaw rotation angles about the S frame's z, y, and x axes as illustrated in Figure 7.3 (i.e. $R_{PS} = R_{z,\psi s}R_{y,\phi s}R_{x,\theta s}$). Next, the angles are redefined in terms of frame *G*. Given the relation between frames *P* and *G*, as shown in Figure 7.4, these redefined angles are:

$$\psi = -\theta_s \tag{7.22}$$

$$\phi = \psi_s \tag{7.23}$$

$$\theta = -\phi_s \tag{7.24}$$

where ψ, ϕ, and θ represent the rotation angles about the new frame's z_g, y_g, and x_g axes respectively. Now, the inverse kinematics process for the Agile Eye begins with developing equations for the 3D $\mathbf{u}_i$ direction vectors in terms of the scalar parameters given in chapter 3.

7.2.3. Forward Kinematics

For the sake of completeness, a discussion of the SPRR/S mechanism's forward kinematics procedure is included here. However, this discourse will be significantly briefer than the preceding one on inverse kinematics. To start, the forward kinematics procedure requires derivation of a relationship between the Agile Eye's active joint states and end-effector orientation, assuming that the former is known and the latter is to be determined [57]. In the interest of focusing on the SPRR/S mechanism's novel components, this initial stage of forward kinematics procedure is not detailed here; the reader may refer to Niyetkaliyev's and Shintemirov's work in [52], where one approach is explored thoroughly. Note that the procedure associated with the Agile Wrist in their work also applies to the Agile Eye, because these are two design embodiments of the same base mechanism: the 3-RRR manipulator.

Thus, our discussion begins with the assumption of an established algorithm for θ_s, ϕ_s, and ψ_s angles in terms of θ_i active joint inputs:

$$\psi_s = g\left(\theta_1, \theta_2, \theta_3\right) \tag{7.25}$$

$$\phi_s = g\left(\theta_1, \theta_2, \theta_3\right) \tag{7.26}$$

$$\theta_s = g\left(\theta_1, \theta_2, \theta_3\right) \tag{7.27}$$

where 'g' signifies a mathematical function in a generalized sense (i.e. the g function may vary for each instance of its use). The succeeding procedure for relating Agile Eye end-effector orientation to hip orientation ultimately mirrors the inverse kinematics process given in Secs. 7.2.1–7.2.2.

First, the assumedly known values for θ_s, ϕ_s, and ψ_s provides the orientation of the Agile Eye end-effector with respect to the global P frame:

$$R_{PS} = R_{z,\psi_s} R_{y,\phi_s} R_{x,\theta_s} = \begin{bmatrix} q_{11} & q_{12} & q_{13} \\ q_{21} & q_{22} & q_{23} \\ q_{31} & q_{32} & q_{33} \end{bmatrix} \tag{7.28}$$

Next, the system is observed from the x_s–z_s plane, as shown in Figure 7.7. Because the location of the hip joint at **f** is fixed relative to frame P, the position of **f** in terms of frame S can be found as follows:

$$^{S}\mathbf{f} = R_{PS}^{T}\, ^{P}\mathbf{f} \tag{7.29}$$

where $^{P}\mathbf{f}$ is constant and R_{PS} is given by Eq. 7.28. Furthermore, rotary joint position $\mathbf{o_1}$ is located at a known distance l_3 from **f** because it is rigidly attached to the femur orthotic. Additionally, the mechanical constraints associated with the exoskeleton structure ensure that $^{S}o_{1x}$ has a value of $-l_2$. Therefore, the value of the $^{S}o_{1z}$ coordinate can be determined as the negative intersect between a circle of radius l_3 centered at $^{S}\mathbf{f}$ and line $x_s = {}^{S}o_{1x} = -l_2$:

$$^{S}o_{1z} = \frac{-D_1 - \sqrt{D_1^{\,2} - 4E_1}}{2} = -l_1 \tag{7.30}$$

where

$$D_1 = -2\left(^{S}f_z\right) \tag{7.31}$$

$$E_1 = l_2^{\,2} + \left(^{S}f_z\right)^2 + 2l_2\left(^{S}f_x\right) + \left(^{S}f_x\right)^2 - l_3^{\,2} \tag{7.32}$$

As shown in Figure 7.7, the angle between the z_f-axis and line connecting $\mathbf{o_1}$ and **f** is given by δ_1, which is a known design parameter because $^{F}\mathbf{o_1}$ is a constant. Now, within the x_s–z_s plane, the acute angle between the vertical and line connecting $\mathbf{o_1}$ and **f** is given by δ_2:

$$\delta_2 = \operatorname{atan2}\left(^{S}f_x - {}^{S}o_{1x},\, ^{S}f_z - {}^{S}o_{1z}\right) \tag{7.33}$$

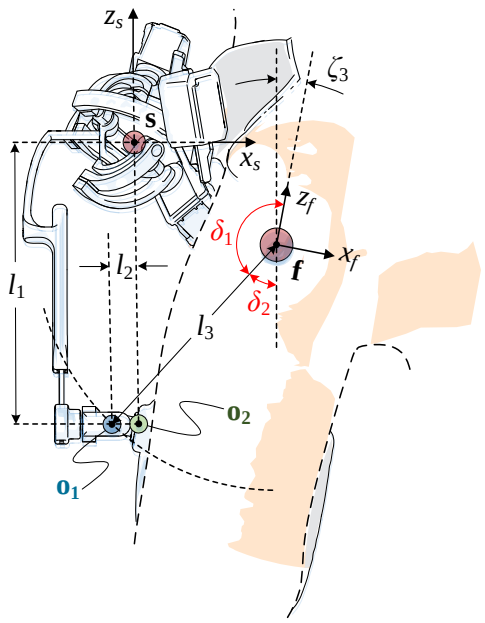

Figure 7.7. Schematic view of SPRR/S device from x_s–z_s plane

The angle between the z_f-axis and z_s-axis within the x_s–z_s plane is then given as:

$$\zeta_3 = \delta_1 + \delta_2 - 180° \tag{7.34}$$

Now observing the system from the y_s–z_s plane, as shown in Figure 7.8, the angle between z_f and the line connecting $\mathbf{o_1}$ and $\mathbf{f}$ is known as a design parameter; this angle is characterized as δ_3. The angle between the y_s–z_s plane's vertical and the line connecting $\mathbf{o_1}$ and $\mathbf{f}$ can be found as follows:

$$\delta_4 = \text{atan2}\left({}^S o_{1y} - {}^S f_y, {}^S f_z - {}^S o_{1z}\right) \tag{7.35}$$

where ${}^S o_{1y}$ is equal to zero for this design. Finally, the angle between the z_f-axis and z_s-axis within the y_s–z_s plane is given as:

$$\zeta_4 = \delta_3 + \delta_4 - 180° \tag{7.36}$$

With both of the two necessary angles required to specify the orientation of frame F with respect to frame S established, the transformation matrix describing this relative orientation can be found. The transformation matrix is acquired through a rotation about the y_s-axis by ζ_3 followed by a rotation about the updated x-axis by angle ζ_4:

$$R_{SF} = R_{y,\zeta_3} R_{x,\zeta_4} = \begin{bmatrix} C\zeta_3 & S\zeta_3 S\zeta_4 & S\zeta_3 C\zeta_4 \\ 0 & C\zeta_4 & -S\zeta_4 \\ -S\zeta_3 & C\zeta_3 S\zeta_4 & C\zeta_3 C\zeta_4 \end{bmatrix} = \begin{bmatrix} {}^S\mathbf{x}_f & {}^S\mathbf{y}_f & {}^S\mathbf{z}_f \end{bmatrix} \tag{7.37}$$

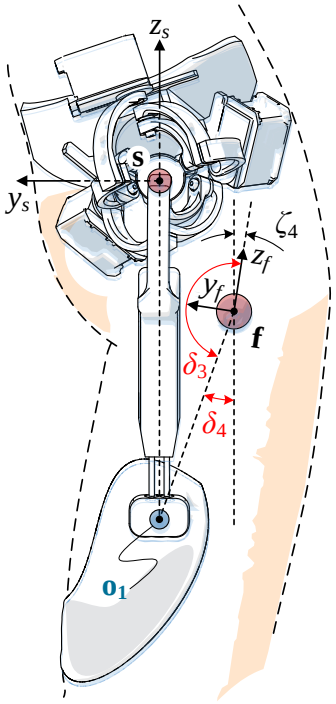

Figure 7.8. Schematic view of SPRR/S device from y_s–z_s plane

where the resulting matrix provides direction vectors of the frame F axes represented in frame S. Note that the rotation angles are positive because their positive values correspond to positive rotations about their associated axes, as depicted in Figure 7.7 and Figure 7.8. Also note that the order of rotations in Eq. 7.37 is significant because it ensures that the x_s-axis remains parallel to the x_f–z_f plane; as mentioned earlier, this represents the physical constraint that the passive prismatic joint cannot rotate about its axis of action.

Lastly, the femur frame F can be expressed in terms of the pelvis reference frame P by pre-multiplying each frame F axis (expressed in frame S) by the R_{PS} transformation matrix developed in Eq. 7.28:

$$R_{PF} = \begin{bmatrix} R_{PS}\,{}^{S}\mathbf{x}_f & R_{PS}\,{}^{S}\mathbf{y}_f & R_{PS}\,{}^{S}\mathbf{z}_f \end{bmatrix} = \begin{bmatrix} {}^{P}\mathbf{x}_f & {}^{P}\mathbf{y}_f & {}^{P}\mathbf{z}_f \end{bmatrix} \tag{7.38}$$

If desired, the terms of R_{PF} can be grouped and trigonometrically evaluated to provide the associated roll-pitch-yaw angles of the hip, visualized as the θ_f, ϕ_f, and ψ_f angles in Figure 7.3. This completes the forward kinematics procedure for the SPRR/S

mechanism, relating known Agile Eye active joint inputs θ_i to the resulting spatial orientation of the hip joint.

7.3. Simulation-Based Verification of Kinematic Analysis

The inverse kinematics procedure described in Sec. 7.2 can be verified by a series of simulations using a fully-articulated SolidWorks 3D model of the SPRR/S mechanism, virtual actuators, and a virtual inertial measurement unit (IMU). The software used to complete this task was a synthesis of SolidWorks, Simulink, and SimMechanics. Table 7.1 defines the design parameters employed on the 3D model. For the first simulation, the virtual actuator's control signals were derived from a desired hip joint orientation signal via our inverse kinematics algorithm. The resulting orientation signal of the model hip joint was then captured using the virtual IMU and compared to the original, desired orientation signal.

Table 7.1. Device parameters used for simulations

Parameter (i.e. for $i, j = 1, 2, 3$)	**Value**
Position of 3-RRR center-of-rotation, ${}^{P}\mathbf{s}$	[-115.6 0 138.2] mm
Position of rotary joint $\mathbf{o}_1$ in F frame, ${}^{F}\mathbf{o}_1$	[-23 104]
Distance between $\mathbf{o}_1$ and $\mathbf{o}_2$, l_2	200.25 mm

Figure 7.9 shows overlaid plots of the desired and virtually-measured signals corresponding to the hip joint's orientation during normal gait cycles; these gait signals are provided by Stanford University's OpenSim software [29, 30].

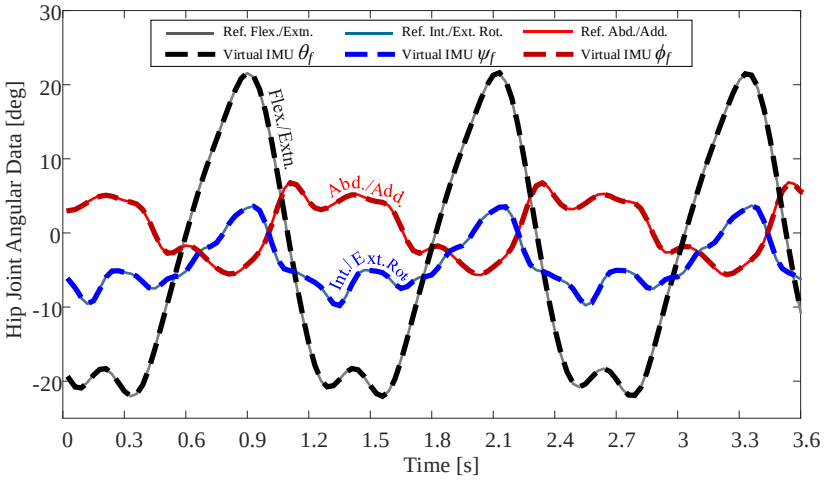

Figure 7.9. Overlay plots of desired and virtually-measured 3-DOF hip joint angles associated with normal gait cycles

Furthermore, Figure 7.10 shows overlaid plots of the desired and virtually-measured signals corresponding to the moving platform of the Agile Eye during normal gait cycles. By comparing Figure 7.9 and Figure 7.10, one can observe that the Agile eye's moving platform needs to undergo a much smaller rotation in orientation workspace in order to compensate the motion required for the Hip joint during the walking gait cycle. As shown in the Figure 7.10, the θ_s component of the Agile Eye end-effector's motion is almost equal to the flexion motion of the hip joint when such a motion is performed. Contrarily, the Agile Eye undergoes less rotation than the hip when abduction and rotation motion is undergone at the hip joint.

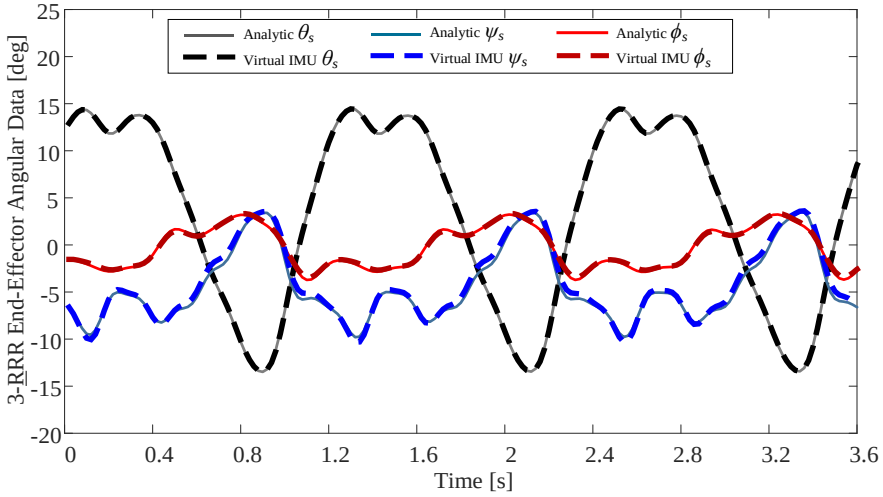

Figure 7.10. Overlay plots of desired and virtually-measured angles of the Agile Eye's moving platform associated with normal gait cycles

Figure 7.11 shows the maximum range for each major motion of the hip joint (i.e. flexion/extension, abduction/adduction, and internal/external rotation) as permitted by the SPRR/S exoskeleton device. At each of these limits, the device's prismatic slider reaches a mechanical stop that prevents further motion beyond the limit. The mechanical restrictions on the exoskeleton motions match the average limits of human capability at the hip joint. This design decision was made in the interest of the user's safety in advance of human trials [30]. However, electrical switches can also be installed within the prismatic joint's track to allow detection of threshold postures before mechanical limits are met. These switches can be used in conjunction with a control scheme that avoids motions that lead to threshold postures. Also, note that the track design may be altered to provide a greater or less ranges of motions, for applications or individuals that require such adjustment.

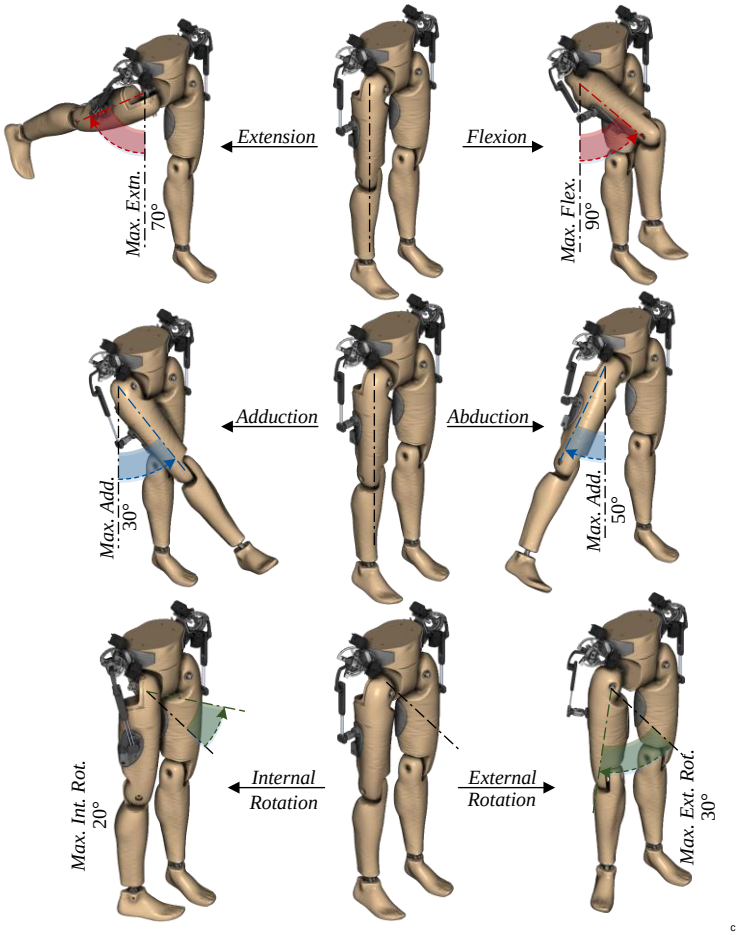

Figure 7.11. Ranges of motion of the SPRR/S mechanism

The second set of simulations tests the inverse kinematics accuracy during the hip's flexion/extension, abduction/adduction, and internal/external rotation motions when they are isolated from each other. Figure 7.12 presents overlay plots of control and virtual response signals corresponding to sine wave motions in each isolated DOF of the hip. The amplitudes for each motion were selected to approximately match the largest amplitudes experienced during normal gait cycles. Furthermore, Figure 7.12 shows the error distribution associated with the two motions set to constant zero values.

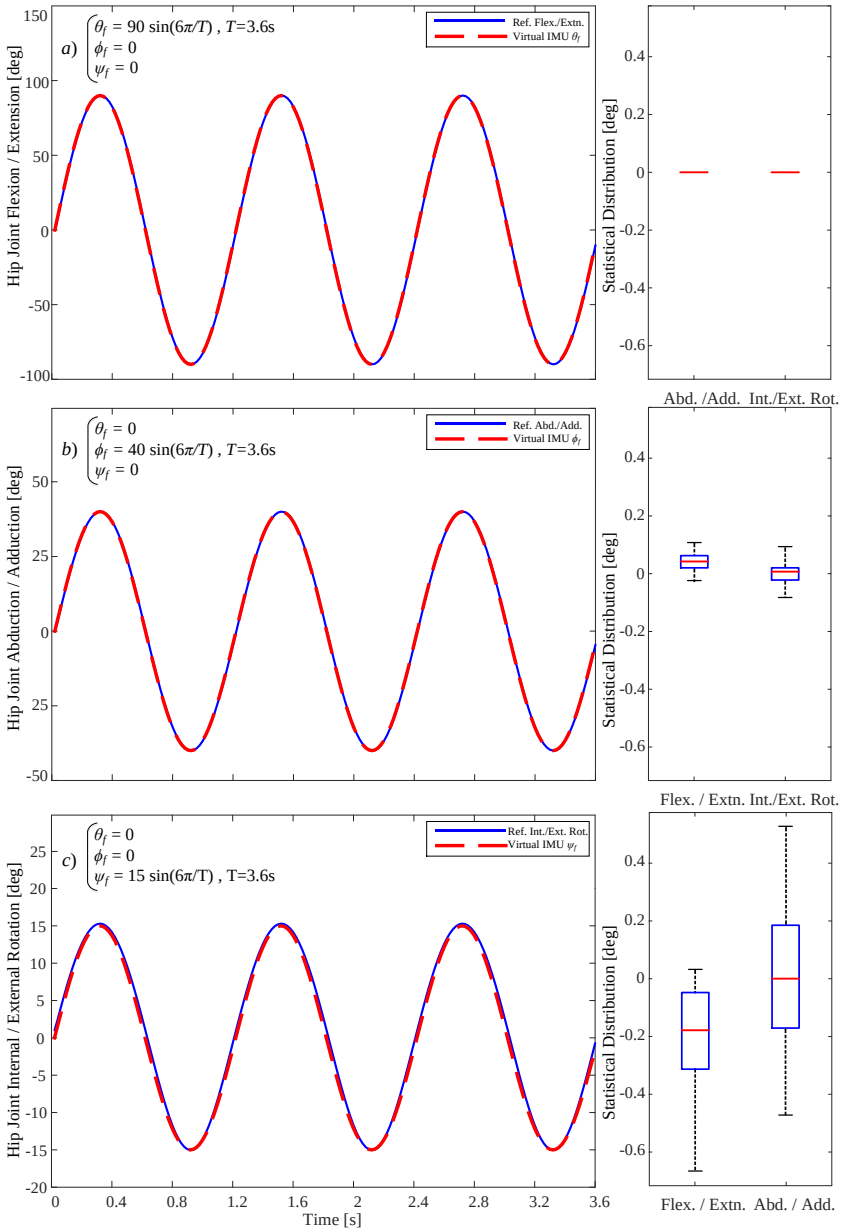

Figure 7.12. Overlay plots of desired and virtually measured 3-DOF hip joint motions and corresponding error boxplots

The general agreement between the control signals and virtual response of the simulated hip joint as shown in Figure 7.9 and 7.10 suggests the validity of the inverse kinematics procedure described in this paper. The error box plots of Figure 7.10 suggest that the maximum error associated with motions prescribed to zero is less than 0.5 degrees, and that internal/external rotation motions tend to cause less error in the other hip DOFs when performed in isolation.

7.4. Dynamic Simulation on the SPRR/S Mechanism

Figure 7.13 shows simulated torque, velocity, and power curves for the actuators of the SPRR/S mechanism during normal gait cycle motions [35, 36]. These plots were obtained by subjecting a Matlab/SimMechanics simulation model of the SRRP/S mechanism to the lower limb motions experienced by a 75.16 kg person's hip, knee and aknle during normal gait cycle motions, as provided by the OpenSim software, and monitoring motor torques and velocities using virtual sensors. In this simulation study the exoskeleton structure was assumed to be made from an Aluminum material. The mass properties feature of SolidWorks software measured the overall weight of the mechanism including all the bolts and nuts required for assembling the mechanism. As a result, the overall weight of the exoskeleton mechanism was estimated to be 2.4 kg. The maximum magnitude torque, velocity, and power associated with the SRRP/S mechanism are 25 N.m, 2.4 rad/s, and 21.5 W.

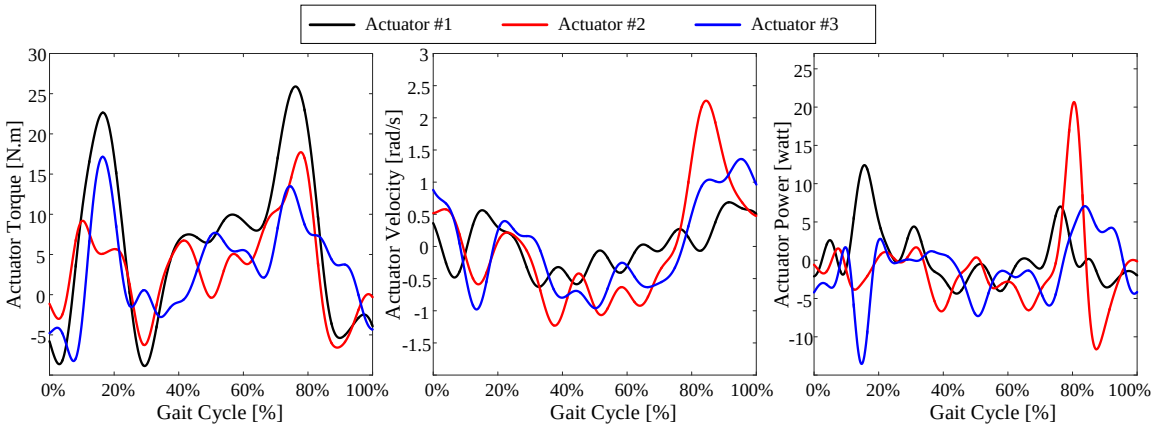

Figure 7.13. Torque, speed, and power required for the SPRR/S device to emulate hip joint motion during normal gait

7.5. Experimental Study on the SPRR/S Mechanism

The simulation results of Sec. 7.3 provide a useful understanding on the accuracy of the inverse kinematics algorithm derived in this study. However, they do not account for possible practical issues, including but not limited to: design imperfections introduced during fabrication, mechanical interferences, etc. Therefore, a physical prototype of the SPRR/S was fabricated to enable experimental data collections that

would further confirm our kinematic analysis and the mechanism's practical performance. The following sections discuss the fabrication method employed and experimental results obtained.

7.5.1. Mechanism Fabrication Details

The prototype mechanism is composed of two main parts: an exoskeleton structure that embodies the SPRR kinematic architecture and a dummy structure that embodies the passive spherical joint targeted for motion assistance. The exoskeleton's pelvis and femur orthotic parts are produced from a 3D printer. The remaining structural components of the exoskeleton are fabricated from aluminum using a CNC machine. Additionally, the exoskeleton's passive joint components are realized as off-the-shelf parts; meanwhile, the active 1-DOF rotary joints are realized as Maxon DCX32L DC motors with ENX16 absolute encoders, each controlled by an EPOS2 50/5 Positioning Controller. Next, the dummy structure is actuated as a mannequin with a modified hip joint. The primary modification made to the mannequin is the installation of a ball-and-socket joint (i.e. swivel joint) at its hip to facilitate realistic 3-DOF rotational motion capability of the femur with respect to the pelvis. The complete SPRR/S mechanism is constructed such that the parameters given in Table 7.1 remain applicable. Figure 7.14 shows a picture of the physical prototype along with a view of the CAD model from which it is based.

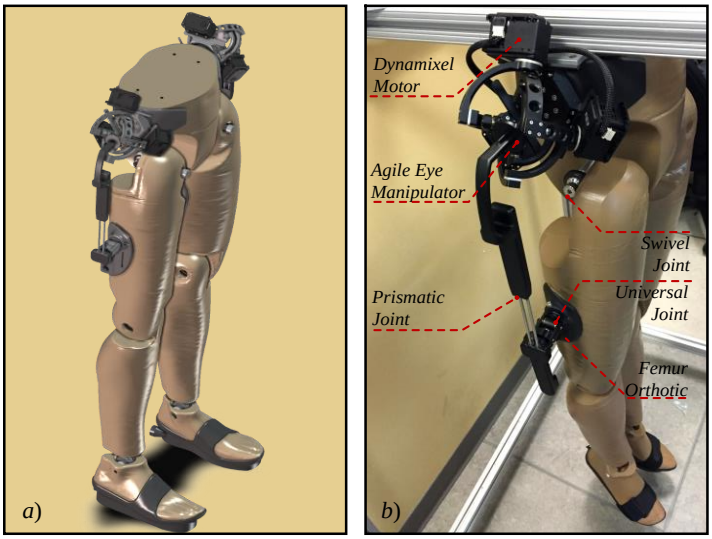

Figure 7.14. a) CAD model of SPRR/S assembly, and b) photo of physical SPRR/S

7.5.2. Experimental Results

For our experimental study of the SRRP/S mechanism, the same normal gait cycle motion that was used during the simulations (i.e. obtained from OpenSim [29, 30]), was employed as the dummy hip joint's motion control signal. This desired output signal was converted to individual motor signals in real-time via the inverse kinematics algorithm detailed in Sec. 7.2. The aforementioned controller unit was used to control the motors' motions during the tracking task based on feedback from the encoder sensors. Figure 7.15 shows overlaid plots of the reference signal and encoder feedback for each motor during the normal gait tracking experiment. The agreement between control and feedback signals in these plots satisfies that SPRR/S mechanism is physically able to accurately track the motions associated with the human hip joint during normal gait.

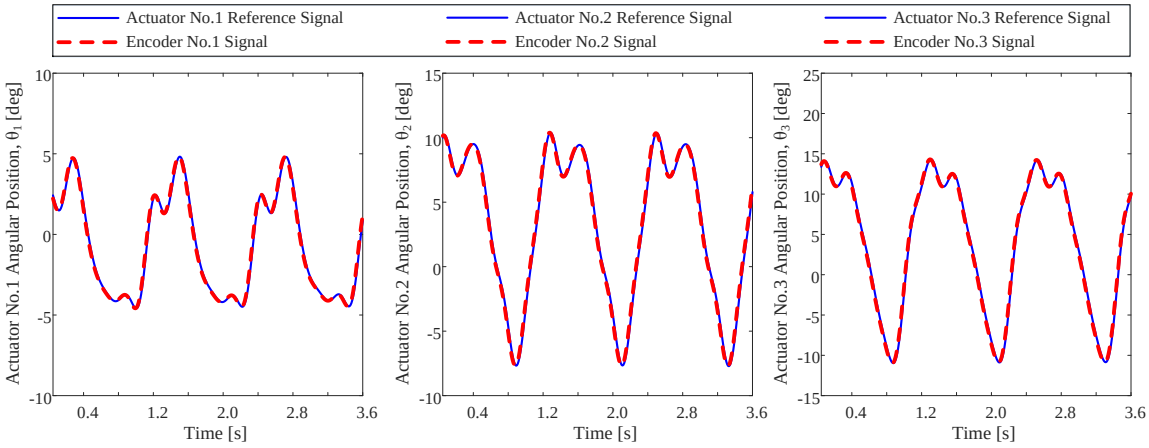

Figure 7.15. Experimentally-acquired control and feedback signals for each SPRR/S motor during normal gait tracking

7.6. Conclusion

This study presented the design, kinematic analysis, simulation, and experimentation of a novel robotic SPRR/S mechanism meant for assisting motion for a ball-and-socket joint. The design encompasses a subsystem that is able to produce active 3-DOF rotational motions, a passive motion-transmission subsystem, and the ball-and-socket joint targeted for motion guidance. Overall, the coordinated motions of these subsystems enable our design to transport fully defined motions to the targeted spherical joint.

Simulation and experimental evaluations of the mechanism were performed as a means of validating the kinematic analysis results. These evaluations focus on the specific application of the device as a wearable hip exoskeleton that is designed to transfer and guide spherical motions about human's hip joint. The simulation findings indicate that the SPRR/S mechanism is in fact able to fully define and guide its targeted passive spherical joint through the same motions that a human hip undergoes. Furthermore, the findings from our simulations results suggest that the mechanism is able to isolate motion in each of the three rotational degrees-of-freedom associated with the target spherical joint. Ultimately, the experimental results indicate that the mechanism is physically capable of transferring and tracking normal gait cycle motions at the targeted joint.

Overall, this research study investigated the feasibility of using three different parallel manipulators for the hip exoskeleton application. These mechanisms were, spatial, orientation and spherical parallel manipulators. A number of performance indices was chosen in order to compare these embodiments and to come up with a candidate solution. It was concluded that the spherical parallel manipulator would be a viable solution to use in hip exoskeleton application; however, the spherical parallel manipulator by nature has far less range of motion compared to the allowable workspace seen on the hip joint. To tackle this shortcoming a serial chain of passive joints was designed and assembled to the existing spherical manipulator in order to amplify its range of motion.

Chapter 8.

Summary and Future Work

8.1. Summary of Thesis

The goal of this research study was to design and manufacture a robotic structure that is able to produce rotations about the hip joint. To do that, first a through anatomy study on the hip joint was conducted to gain an in-depth knowledge about its mechanical characteristics and functioning. Several conceptual designs were generated and carefully reviewed in terms of the joints' motion constraints and other design specifications and preferences in terms of functionality, simplicity and ease of wear. Three different embodiments of parallel manipulators capable of transferring active 3-DOF rotational motions to the human upper leg was explored. It was concluded that the Agile Eye is the most viable and suitable candidate to be incorporated within the hip exoskeleton.

With the Agile Eye as the final solution, two generations of hybrid spherical manipulators were designed and fabricated. It was shown that the proposed mechanisms were able to fully define the position of the target hip joint. In summary, the study entailed a 3-DOF motion-generation system (i.e. Agile eye) that is mechanically capable of providing decoupled or combined 3-DOF rotational motion to a targeted 3-DOF joint by the way of a motion transfer mechanism. The target joint can be any 3-DOF rotational joint (e.g. ball-and-socket joint) or a quasi-3-DOF rotational joint. Furthermore, the motion transfer and target interfacing system prevents or minimizes forces along the protrusion's axis passing through the target joint, thereby reducing the risk of damage to the target system. The motion-generation system is additionally capable of causing the target system to pause and hold a constant angular position about its true or quasi 3-DOF rotational joint.

In another aspect, information on how to achieve the desired action or inaction of the target system should be provided to the motion-generation system by a motion-generation controller system. This controller system includes software execution commanding the motion-generation system's actuator action via an appropriate driver subsystem. Additionally, the software may accept control signals from a joystick, or it may execute based on a predefined signal. Furthermore, the controller system accepts and responds to information input from a motion detection and feedback system that interfaces with and monitors the target system. The motion detection and feedback system may acquire information on the target joint's state using one or more inertial measurement units, rotary encoder sensors, linear encoder sensors, etc.

The proposed design demonstrated improved abilities over competitor's products. Both an IMU based remote-control scheme and a predefined walking gait was used as a benchmark to test the functionality of the prototype. The mechanism was able to produce active 3-DOF motion on the hip joint of an anthropomorphic dummy. The mechanism was able to follow a walking gait.

Overall, we can conclude that the exoskeleton system designed can potentially be used to cover a wide range of mobility disorders and body structures. Our system has relatively simple design which is not difficult to control. It is a novel use of the Agile Eye spherical parallel manipulator for exoskeleton application. Finally, our system was successful in its functionality of performing walking gait motions, and successful in obtaining desired full hip joint range of motion.

8.2. Future Work

The following research directions can be considered as the continuation of this study:

- **Bio-feedback sensor design:** At this stage a reliable human interface should be introduced as the connection means between the human operator and exoskeleton. Current human machine interfaces (HMI) can be defined and categorized as: kinematic [85], dynamic [86] and neuromuscular, e.g. surface electromyography (EMG) [87] methods. Among them, neuromuscular

sensor based interfaces is the preferred method in capturing the human body motions. That is mainly because, these sensors are able to estimate the effects of muscle contractions even before these effects can be directly measured using other means (e.g., kinematic and dynamic interfaces) [88], [89]. One of the drawbacks of the biological signals such as skin surface EMG is high signal to noise ratio and uncertainties in signal interpretations. The shortcomings are related to complexity and fuzzy behaviour of human body. It is however recommended that the EMG signals should be considered as the primary input to the lower limb exoskeleton control system. The main objective in this section is the development of a signal processing algorithm to extract valid data out of the raw signal. To collect signals, sufficient number of tests has to be performed on human subjects.

- **Control design:** The controllers of the exoskeleton structure will be responsible to command motion and keep the structure balanced. As stated, the controller should receive input from the biofeedback sensors and provide commands for the actuators. In order to keep the integrity, avoid potential conflicts in sequences of tasks performance and completion by different actuators, and increase the computational throughput, all the high level commands should be made by a central controller. Several other issues such as stability, robustness, accuracy and operation safety should also be considered and tackled in the design of the controller.

- **Power consumption optimization:** The power needed to operate the lower limb exoskeleton can be estimated from the energy required by the actuators during walking on flat surface and climbing slopes. Mechanical losses such as friction in the joints should be incorporated in the simulation to estimate system efficiency. The effect of several factors including the weight of the structure, joints friction, electrical motors efficiency, and losses in power transmission mechanisms, on the power consumption of WLLAE should be investigated. Development of recharging circuit, power management modules should also be considered.

- **Performance evaluation through field tests:** Tasks related to operating the device, acquiring sensory data, and analyzing the results. The lower limb exoskeleton instrumented on a real human test subject should be tested in various situations such as siting, turning, and climbing and descending stairs and slopes. The sensors, actuators and controller parameters should then be tuned to achieve the best possible performance, depending on parameters such as the weight, type of disability, and muscles and skeleton condition of the user.

References

[1] D. Brown-Triolo, M. Roach, K. Nelson, and R. Triolo, “Consumer perspectives on mobility: implications for neuroprosthesis design.,” *Neural Repair*, vol. 39, pp. 659–670, 2002.

[2] A. Tsukahara, R. Kawanishi, Y. Hasegawa, and Y. Sankai, “Sit-to-stand and stand-to-sit transfer support for complete paraplegic patients with robot suit HAL.,” *Adv. Robot*, vol. 24, pp. 1615–1638, 2010.

[3] A. Esquenazi, M. Talaty, A. Packel, and M. Saulino, “The ReWalk powered exoskeleton to restore ambulatory function to individuals with thoracic-level motor-complete spinal cord injury.,” *Am. J. Phys. Med. Rehabil.*, vol. 91, no. 11, pp. 911–21, Nov. 2012.

[4] L. Riener R, ¨, A. M. nenburger L, Jezernik S, and D. V. Colombo G, “Patient-cooperative strategies for robotaided treadmill training: first experimental results.,” *IEEE Trans Neural Syst Rehabil Eng*, vol. 13, pp. 380–394, 2005.

[5] J. Cao, S. Xie, R. Das, and G. Zhu, “Control strategies for effective robot assisted gait rehabilitation: the state of art and future prospects.,” *Med Eng Phys*, vol. 6, pp. 1555–1566, 2014.

[6] G. Ostrovsky, “Berkeley Bionics eLEGS Exoskeleton Gets Paraplegics On Their Legs,”2010.[Online].Available:http://www.medgadget.com/2010/10/berkeley_bionics_ele gs_exoskeleton_gets_paraplegics_on_their_legs.html. [Accessed: 01-Sep-2015].

[7] “(N.D.). Berkeley Robotics & Human Engineering Laboratory: Austin.” [Online]. Available:http://bleex.me.berkeley.edu/research/exoskeleton/medicalexoskeleton/.

[8] “(N.D.). Ekso Bionicss [Online].” [Online].”Available: http://www.eksobionics.com/. [Accessed Sept. 4, 2014].

[9] “(N.D.). Indego.” [Online]. Available: http://www.indego.com/indego/en/news. [Accessed Sept. 8, 2014]. [10]“(N.D.). ReWalk.” [online] .

[11] “ReWalk Bionic Suit Personal Exoskeleton System Cleared by FDA for Home Use,” 2014. .

[12] “(N.D.). REX Bionics.” Available: http://rewalk.com/rewalker-gallery/. [Accessed

Sept. 8, 2014].

[13] “Neurogadget,” 2013. [Online]. Available: http://neurogadget.com/2013/03/13/mindwalker-exoskeleton-uses-eeg-cap-to-helpdisabled-people-walk-again/7532. [Accessed: 01-Sep-2015].

[14] “Cyberdyne.”[Online]. Available: http://www.cyberdyne.jp/english/products/LowerLimb_medical.html. [Accessed: 01-Sep-2015].

[15] “(N.D.). Honda.” Available: http://corporate.honda.com/innovation/walk-assist/. [Accessed Sept. 8, 2014]..

[16] S. Yang., “UC Berkeley researchers developing robotic exoskeleton that can enhance human strength and endurance,” 2004. [Online]. Available: http://www.berkeley.edu/new s/media/releases/2004/03/03_exo.shtml.

[17] A. B. Zoss et al, “Biomechanical design of the Berkeley lower extremity exoskeleton (BLEEX),” *IEEE/ASME Trans. Mechatronics*, vol. 11, pp. 128–138, 2006.

[18] M. Cenciarini and A. M. Dollar, “Biomechanical considerations in the design of lower limb exoskeletons.,” *IEEE Int. Conf. Rehabil. Robot.*, vol. 2011, p. 5975366, Jan. 2011.

[19] “(N.D.). Berkeley Robotics & Human Engineering Laboratory: ExoHiker.” .

[20] “(N.D.). Berkeley Robotics & Human Engineering Laboratory: ExoClimber.” .

[21] “Berkeley Robotics & Human Engineering Laboratory: HULC.” .

[22] “(N.D.) Lockheed Martin:HULC.”[Online]. Available:http://www.lockheedmartin.ca/us/pro ducts/hulc.html. [Accessed: 01-Sep-2015].

[23] C. J. Walsh, D. Paluska, K. Pasch, W. Grand, A. Valiente, and H. Herr, “Development of a lightweight, underactuated exoskeleton for load-carrying augmentation,” in *Proceedings 2006 IEEE International Conference on Robotics and Automation, 2006. ICRA 2006.*, 2006, pp. 3485–3491.

[24] A. (Andrew J. . Valiente, “Design of a quasi-passive parallel leg exoskeleton to augment load carrying for walking,” 2005.

[25] “(N.D.). Raytheon XOS 2 Exoskeleton, Second-Generation Robotics Suit, United States of America,” 2014. .

[26] “Feature: Wearable Exoskeletons That Give Humans Super Strength,” 2008. [Online]. Available: http://www.techeblog.com/index.php/tech-gadget/feature-

wearableex oskeletons-that-give-humans-super-strength. [Accessed: 01-Sep-2014].

[27] W. Erickson, C. Lee, and S. Schrader, “Disability Statistics from the 2013 American Community Survey (ACS),” Newyork, 2015.

[28] Statistics Canada, “Disability in Canada: Initial findings from the Canadian Survey on Disability,” Ottawa, 2012.

[29] A. B. Zoss, H. Kazerooni, and A. Chu, “Biomechanical design of the Berkeley lower extremity exoskeleton (BLEEX),” *IEEE/ASME Trans. Mechatronics*, vol. 11, no. 2, pp. 128–138, Apr. 2006.

[30] A. B. Zoss, H. Kazerooni, and A. Chu, “Biomechanical design of the Berkeley lower extremity exoskeleton (BLEEX),” *IEEE/ASME Trans. Mechatronics*, vol. 11, no. 2, pp. 128–138, Apr. 2006.

[31] J. Rose and J. G. Gamble, *HumanWalking*, 2nd ed. Baltimore:Williams & Wilkins, 1994.

[32] M. Ishii, K. Yamamoto, and K. Hyodo, “Stand-Alone Wearable Power Assist Suit – Development and Availability–,” *J. Robot. Mechatronics*, vol. 17, no. 5, pp. 575–583, Oct. 2005.

[33] A. Winter and Gait Data. Int. Soc., “Biomechanical Data Resources.” .

[34] C. Kirtley, “CGA Normative Gait Database,” *Hong Kong Polytechnic Univ.* [Online]. Available: http://guardian.curtin.edu.au/cga/data/.

[35] F. C. Anderson and M. G. Pandy, “A Dynamic Optimization Solution for Vertical Jumping in Three Dimensions.,” *Comput. Methods Biomech. Biomed. Engin.*, vol. 2, no. 3, pp. 201–231, 1999.

[36] Jean-Pierre Merlet, *Parallel Robots*, Second Edi. Sophia-Antipolis, France: Springer, 2006.

[37] D. Stewart, “A platform with six degrees of freedom,” *Proc. Inst. Mech. Eng.*, vol. 180, no. 1965, pp. 371–386, Jun. 1965.

[38] J.-P. Merlet, *Parallel Robots*, Second. Berlin/Heidelberg: Springer-Verlag, 2006.

[39] L.-W. Tsai, *Robot analysis : the mechanics of serial and parallel manipulators*. New York: J. Wiley and Sons, 1999.

[40] C. Gosselin, “Determination of the Workspace of 6-DOF Parallel Manipulators,” *J. Mech. Des.*, vol. 112, no. 3, p. 331, 1990.

[41] M. H. Abedinnasab and G. R. Vossoughi, “Analysis of a 6-DOF redundantly actuated 4-legged parallel mechanism,” *Nonlinear Dyn.*, vol. 58, no. 4, pp. 611–622, Dec. 2009.

[42] M. Takaiwa, T. Noritsugu, N. Ito, and D. Sasaki, “Wrist Rehabilitation Device Using Pneumatic Parallel Manipulator Based on EMG Signal,” *Int. J. Autom. Technol.*, vol. 5, no. 4, pp. 472–477, Jul. 2011.

[43] T. Onodera, M. Ding, H. Takemura, and H. Mizoguchi, “Design and development of Stewart platform-type assist device for ankle-foot rehabilitation,” in *2012 First International Conference on Innovative Engineering Systems*, 2012, pp. 1–6.

[44] S. Kucuk and Z. Bingul, “Comparative study of performance indices for fundamental robot manipulators,” *Rob. Auton. Syst.*, vol. 54, no. 7, pp. 567–573, Jul. 2006.

[45] C. Gosselin, “Kinematic Analysis Optimization and Programming of Parallel Robotic Manipulators,” McGill University, 1985.

[46] R. J. Farris, H. A. Quintero, S. A. Murray, K. H. Ha, C. Hartigan, and M. Goldfarb, “A preliminary assessment of legged mobility provided by a lower limb exoskeleton for persons with paraplegia.,” *IEEE Trans. Neural Syst. Rehabil. Eng.*, vol. 22, no. 3, pp. 482–90, May 2014.

[47] Z. Li, H. Xie, W. Li, and Z. Yao, “Proceeding of human exoskeleton technology and discussions on future research,” *Chinese J. Mech. Eng.*, vol. 27, no. 3, pp. 437–447, May 2014.

[48] C. M. Gosselin and E. Lavoie, “On the Kinematic Design of Spherical Three-Degree-of- Freedom Parallel Manipulators,” *Int. J. Rob. Res.*, vol. 12, no. 4, pp. 394–402, Aug. 1993.

[49] C. M. Gosselin and E. St-Pierre, “Development and Experimentation of a Fast 3-DOF Camera-Orienting Device,” *Int. J. Rob. Res.*, vol. 16, no. 5, pp. 619–630, Oct. 1997.

[50] S. Bai, M. R. Hansen, and J. Angeles, “A robust forward-displacement analysis of spherical parallel robots,” *Mech. Mach. Theory*, vol. 44, no. 12, pp. 2204–2216, Dec. 2009.

[51] Y. Jian and J. Angeles, “Kinematics simulation and control design of the Agile Wrist in a Dual-arm robotic mechanical systems,” in *2012 IEEE International Conference on Computer Science and Automation Engineering (CSAE)*, 2012, vol. 3, pp. 39–42.

[52] A. Niyetkaliyev and A. Shintemirov, “An approach for obtaining unique kinematic solutions of a spherical parallel manipulator,” in *2014 IEEE/ASME International*

Conference on Advanced Intelligent Mechatronics, 2014, pp. 1355–1360.

[53] J. Gallardo-Alvarado, M. A. García-Murillo, and L. Pérez-González, “Kinematics of the 3RRRS+S Parallel Wrist: A Parallel Manipulator Free of Intersecting Revolute Axes#,” *http://dx.doi.org/10.1080/15397734.2013.781480*, 2013.

[54] G. Cui, H. Zhou, H. Zhang, D. Zhang, and Y. Zhang, “Robust Design Optimization of a 4-UPS-S Parallel Manipulator for Orientation-Regulating Control System of Solar Gather Panels,” *J. Ind. Eng.*, vol. 2015, p. 10, 2015.

[55] C. Wang, Y. Fang, S. Guo, and Y. Chen, “Design and Kinematical Performance Analysis of a 3- R US/ R RR Redundantly Actuated Parallel Mechanism for Ankle Rehabilitation,” *J. Mech. Robot.*, vol. 5, no. 4, p. 41003, Jul. 2013.

[56] J. Enferadi and A. Shahi, “On the position analysis of a new spherical parallel robot with orientation applications,” *Robot. Comput. Integr. Manuf.*, vol. 37, pp. 151–161, Feb. 2016.

[57] M. W. Spong, S. Hutchinson, and M. Vidyasagar, *Robot Dynamics and Control*, 2nd ed. John Wiley & Sons, 2004.

[58] N. Palastanga, D. Field, and R. W. Soames, *Anatomy and Human Movement Structure and Function.* UK: Elsevier Science, 1989.

[59] S. L. Delp, J. P. Loan, M. G. Hoy, F. E. Zajac, E. L. Topp, and J. M. Rosen, “An interactive graphics-based model of the lower extremity to study orthopaedic surgical procedures,” *IEEE Trans. Biomed. Eng.*, vol. 37, no. 8, pp. 757–767, 1990.

[60] F. C. Anderson and M. G. Pandy, “A Dynamic Optimization Solution for Vertical Jumping in Three Dimensions.,” *Comput. Methods Biomech. Biomed. Engin.*, vol. 2, no. 3, pp. 201–231, Jan. 1999.

[61] R. O. Ambrose *et al.*, “Robonaut: NASA’s space humanoid,” *IEEE Intell. Syst.*, vol. 15, no. 4, pp. 57–63, Jul. 2000.

[62] S. Kizir and Z. Bingul, “Position Control and Trajectory Tracking of the Stewart Platform,” *InTech, Chapters Publ. under CC BY 3.0 Licens.*, pp. 179–202, 2012.

[63] C. M. Gosselin, “The optimum design of robotic manipulators using dexterity indices,” *Rob. Auton. Syst.*, vol. 9, no. 4, pp. 213–226, Jan. 1992.

[64] C. M. Gosselin and E. Lavoie, “On the Kinematic Design of Spherical Three-Degree-of- Freedom Parallel Manipulators,” *Int. J. Rob. Res.*, vol. 12, no. 4, pp. 394–402, Aug. 1993.

[65] C. M. Gosselin and J.-F. Hamel, “The agile eye: a high-performance three-

degree-of-freedom camera-orienting device," in *Proceedings of the 1994 IEEE International Conference on Robotics and Automation*, 1994, pp. 781–786.

[66] C. M. Gosselin and E. St-Pierre, "Development and Experimentation of a Fast 3-DOF Camera-Orienting Device," *Int. J. Rob. Res.*, vol. 16, no. 5, pp. 619–630, Oct. 1997.

[67] T. Yoshikawa, "Manipulability of Robotic Mechanisms," *Int. J. Rob. Res.*, vol. 4, no. 2, pp. 3–9, Jun. 1985.

[68] S. Kucuk and Z. Bingul, "Comparative study of performance indices for fundamental robot manipulators," *Rob. Auton. Syst.*, vol. 54, no. 7, pp. 567–573, Jul. 2006.

[69] A. Valiente, "Design of a Quasi-Passive Parallel Leg Exoskeleton to Augment Load Carrying for Walking," Massachusetts Institute of Technology, 2005.

[70] S. K. Banala, S. K. Agrawal, and J. P. Scholz, "Active Leg Exoskeleton (ALEX) for Gait Rehabilitation of Motor-Impaired Patients," in *2007 IEEE 10th International Conference on Rehabilitation Robotics*, 2007, pp. 401–407.

[71] J. L. Pons, *Wearable Robots: Biomechatronic Exoskeletons*, First. UK: John Wiley & Sons, 2008.

[72] H. P. Crowell, "Human Engineering Design Guidelines for a Powered," 1995.

[73] H. P. Crowell, A. C. Boynton, and M. Mungiole, "Exoskeleton Power and Torque Requirements Based on Human Biomechanics."

[74] C. James Walsh, K. Endo, and H. Herr, "a Quasi-Passive Leg Exoskeleton for Load-Carrying Augmentation," *Int. J. Humanoid Robot.*, vol. 4, no. 3, pp. 487–506, 2007.

[75] C. J. Walsh, "Biomimetic design for an under-actuated leg exoskeleton for load-carrying augmentation," Massachusetts Institute of Technology, 2006.

[76] K. H. Low, "Development and preliminary study of the NTU lower extremity exoskeleton," *IEEE Conf. Cybern. Intell. Syst.*, vol. 2, pp. 1243–1247, 2004.

[77] G. Colombo, M. Joerg, R. Schreier, and V. Dietz, "Treadmill training of paraplegic patients using a robotic orthosis," *J. Rehabil. Res. Dev*, vol. 37, no. 6, pp. 693–700.

[78] G. Colombo, M. Wirz, and V. Dietz, "Driven gait orthosis for improvement of locomotor training in paraplegic patients," *Spinal Cord*, vol. 39, no. 5, pp. 252–255, 2001.

[79] H. van der Kooij, J. Veneman, and R. Ekkelenkamp, “Design of a compliantly actuated exo-skeleton for an impedance controlled gait trainer robot,” *Annu. Int. Conf. IEEE Eng. Med. Biol. Soc.*, vol. 1, pp. 189–193, 2006.

[80] R. J. F. Veneman, R. Ekkelenkamp, F. C. Kruidhof, T. van der Helm, and H. van der Kooij, “Series Elastic- and Bowden-Cable-Based Actuation System for Use as Torque Actuator in Exoskeleton-Type Robots,” *Int. J. Robot. Res. Sage*, 2006.

[81] J. F. Veneman, R. Kruidhof, R. Hekman, E. H. Ekkelenkamp, F. Van Asseldonk, and H. van der Kooij, “esign and Evaluation of the LOPES Exoskeleton Robot for Interactive Gait Rehabilitation,” *IEEE Trans. Neural Syst. Rehabil. Eng.*, vol. 15, no. 3, pp. 379–386, 2007.

[82] S. Kizir and Z. Bingul, “Position Control and Trajectory Tracking of the Stewart Platform,” in *Serial and Parallel Robot Manipulators - Kinematics, Dynamics, Control and Optimization*, S. Kucuk, Ed. InTech, Chapters published under CC BY 3.0 license, 2012, pp. 179–202.

[83] C. Gosselin and J. Angeles, “The Optimum Kinematic Design of a Spherical Three-Degree-of-Freedom Parallel Manipulator,” *J. Mech. Transm. Autom. Des.*, vol. 111, no. 2, p. 202, Jun. 1989.

[84] S. Bai, M. R. Hansen, and J. Angeles, “A robust forward-displacement analysis of spherical parallel robots,” *Mech. Mach. Theory*, vol. 44, no. 12, pp. 2204–2216, 2009.

[85] R. S. Mosher, “Force reflecting electrohydraulic servo manipulator,” *Electro-Tech.*, no. 138, 1960.

[86] T. J. Snyder and H. Kazerooni, “A novel material handling system,” in *Proc. IEEE Int. Conf. Robotics and Automation*, pp. 1147–1152.

[87] J. Rosen, M. B. Fuchs, and M. Arcan, “Performances of hill-type and neural network muscle modelsToward a myosignal based exoskeleton,” *Comput. Biomed. Res.*, vol. 32, no. 5, pp. 415–439.

[88] E. E. Cavallaro, J. Rosen, J. C. Perry, and S. Burns, “Real-time myoprocessors for a neural controlled powered exoskeleton arm,” *IEEE Trans. Biomed. Eng.*, vol. 53, no. 11, pp. 2387–96.

[89] D. Nishikawa, W. Yu, H. Yokoi, and Y. Kakazu, “EMG prosthetic hand controller using real-time learning method,” in *Proc. IEEE Int. Conf. Systems, Man, and Cybernetics*, 1999, pp. 153–158.

[90] I. Mansouri and M. Ouali, “The power manipulability – A new homogeneous performance index of robot manipulators,” *Robot. Comput. Integr. Manuf.*, vol. 27, no. 2, pp. 434–449, Apr. 2011.

[91] I. Mansouri and M. Ouali, “A new homogeneous manipulability measure of robot manipulators, based on power concept,” *Mechatronics*, vol. 19, no. 6, pp. 927–944, Sep. 2009.

[92] J. Angeles and C. S. Lopez-Cajun, “Kinematic Isotropy and the Conditioning Index of Serial Robotic Manipulators,” *Int. J. Rob. Res.*, vol. 11, no. 6, pp. 560–571, Dec. 1992.

[93] R. S. Stoughton and T. Arai, “A modified Stewart platform manipulator with improved dexterity,” *IEEE Trans. Robot. Autom.*, vol. 9, no. 2, pp. 166–173, Apr. 1993.

[94] K. H. Pittens and R. P. Podhorodeski, “A family of stewart platforms with optimal dexterity,” *J. Robot. Syst.*, vol. 10, no. 4, pp. 463–479, Jun. 1993.

[95] A. B. K. Rao, P. V. M. Rao, and S. K. Saha, “Workspace and dexterity analyses of hexaslide machine tools,” in *2003 IEEE International Conference on Robotics and Automation (Cat. No.03CH37422)*, 2003, vol. 3, pp. 4104–4109.

[96] P. Cardou, S. Bouchard, and C. Gosselin, “Kinematic-Sensitivity Indices for Dimensionally Nonhomogeneous Jacobian Matrices,” *IEEE Trans. Robot.*, vol. 26, no. 1, pp. 166–173, Feb. 2010.

[97] W. Dempster, “Space requirements of the seated operator,” Ohio, 1955.

[98] H. Goldstein, *Computer-Aided Kinematics and Dynamics of Mechanical Systems*, 2nd ed. MA: Addison-Wesley, 1980.

[99] I. A. Bonev, D. Chablat, and P. Wenger, “Working and assembly modes of the agile eye,” in *Proceedings 2006 IEEE International Conference on Robotics and Automation, 2006. ICRA 2006.*, pp. 2317–2322.

[100] J. Angeles and Y. Jian, “Kinematics simulation and control design of the Agile Wrist in a Dual-arm robotic mechanical systems,” *2012 IEEE Int. Conf. Comput. Sci. Autom. Eng.*, vol. 3, pp. 39–42, 2012.

Appendix A.

Performance Indices

The following subsections provide a brief overview of the indices to be considered in this study.

Manipulability

Articular forces in parallel robots can reach large magnitudes near singular configurations [36]. Therefore, the ability to measure proximity to a singular configuration is useful for analyzing parallel manipulator design. Manipulability is a performance index used to achieve this quantification. As given in Eq. A1, this index is calculated as the absolute value of the Jacobian determinant [58]:

$$\mu = \sqrt{\left|\mathrm{J}^T \mathrm{J}\right|}\,\frac{\partial^2 \Omega}{\partial v^2} \tag{A.1}$$

Physically, manipulability is an indicator of a manipulator's ability to transmit a desired velocity to its end-effector [90]. The isotropy index for manipulability is an indication of how uniformly velocity can be transferred to the end-effector across all directions of motion [91]. The isotropy index for manipulability is defined as:

$$\mu_{iso} = \sigma_{min} / \sigma_{max} \tag{A.2}$$

where σ_{max} and σ_{min} are respectively the maximum and minimum singular values of the Jacobian matrix, and μ_{iso} therefore ranges in value from 0 to 1. An isotropy index of one indicates that the manipulator is oriented such that it is able to transmit velocity uniformly from its actuators to its end-effector along all directions. Contrarily, when the isotropy index is equal to zero, the manipulator is oriented in a singular configuration and is therefore unable to transmit velocity to the end-effector.

Dexterity

Because a parallel manipulator is generally controlled using the position coordinates of its joints, any errors in these coordinates will cause error in the moving platform position and/or orientation [36]. This end-effector error is obtained as the product of the errors in the articular coordinates and an amplification factor, called the condition number, k [92]. Consequentially, the accuracy of a parallel manipulator is dependent on its condition number, which is defined in terms of the Jacobian matrix as follows[13–15]:

$$k\left(\mathrm{J}\right) = \| \mathrm{J} \| \| \mathrm{J}^{-1} \| \tag{A.3}$$

where J is the Jacobian matrix and ||J|| denotes its Euclidean norm:

$$||\mathrm{J}|| = \sqrt{tr\left(\frac{1}{n}\mathrm{J}\mathrm{J}^{T}\right)} \tag{A.4}$$

It follows that Gosselin [63] has defined the local dexterity, v, as the inverse of the condition number and characterized it as a criterion for measuring the kinematic accuracy of a manipulator. Local dexterity is the second performance index considered in this study:

$$\nu = \frac{1}{||\mathrm{J}||||\mathrm{J}^{-1}||} \tag{A.5}$$

Again, values for v are limited to the range $[0, 1]$. A value of zero indicates that the Jacobian matrix is singular, whereas higher values indicate more accurate motion generation for a given device configuration.

Rotational Sensitivity

Rotational sensitivity is a measure of how severe actuator displacements affect the orientation of a parallel manipulator's end-effector. Cardou *et al.* define τ_r as the index for rotational sensitivity in [96]; technically, it is the maximum-magnitude rotation of the end-effector under a unit-norm actuator displacement. Therefore, the sensitivity index is mathematically represented as:

$$\tau_r = ||\mathrm{J}|| \tag{A.6}$$

for which it is recommended that either a 2–norm or ∞–norm is used to normalize the Jacobian.

Singularity Conditions

A parallel manipulator is said to be at a singular configuration when either J_x or J_q or both are singular. Two different types of singularities can be identified

Inverse Kinematic Singularities

Inverse kinematic singularity occurs when the determinant of J_q goes to zero. When J_q is singular, infinitesimal motion of the moving platform along certain directions cannot be accomplished. Hence the manipulator loses one or more degrees of freedom.

Direct Kinematic Singularities

Direct kinematic singularity happens when the determinate of J_x is equal to zero. At this condition, the moving platform can possess infinitesimal motion is some directions while the actuators are completely locked. Hence the moving platform gains one or more DOF. In other words, at this configuration, the manipulator cannot resist forces or moments in some directions.

Appendix B.

Verification of Simulated Dynamics results in SIMECHANICS/MATLAB with an Analytical Approach

Parameters and Initialization of Coordinates

In order to validate the simulated results obtained from SIMMECHANICS/MATLAB, an analytical study on the dynamics of human body has been introduced and the results of this study will be compared with the ones from simulation.

The calculation for kinetics of human locomotion necessitates us to have knowledge to the anthropometric parameters of human body. Since the inertial parameters such as the segmental mass, segment dimensional characteristics lengths, and segmental mass moment of inertia are difficult to determine for a living person, it can be calculated with the help of values from Dempster's body segment parameter table [97] . With the assistance of the approximate proportion values given in Dempster's table, inertial values for a subject with a total weight of 75kg was estimated and shown in Table B1.

Table B1. Inertial values used for the analytic study

Segment	m (kg)	I (kg.m^2)	a (m)
Foot	1.2	0.011	0.195
Leg	2.4	0.064	0.335
Thigh	6.0	0.130	0.300

It needs to be mentioned that in the multiple segment analysis of lower limb kinetic model the joints have been assumed to be completely frictionless and the body segments are treated as rigid bar. Figure B1 illustrates a 3-DOF planar lower limb structure constructed with three revolute joints located at O_0, O_1 and O_2 respectively. A coordinate system is subsequently attached to each link. The (x_0,y_0,z_0) coordinate system is attached to the base with its origin located at the first joint pivot at the $x-$ axis pointing to the right.

Table B2. D-H parameters for the 3-DOF planar lower limb model

i	a_i	α_i	d_i	θ_i	[$\theta_i(T=0)$]
1	a_1	0	0	θ^*_{1T}	[270°]
2	a_2	0	0	θ^*_{2T}	[0°]
3	a_3	0	0	θ^*_{3T}	[90°]

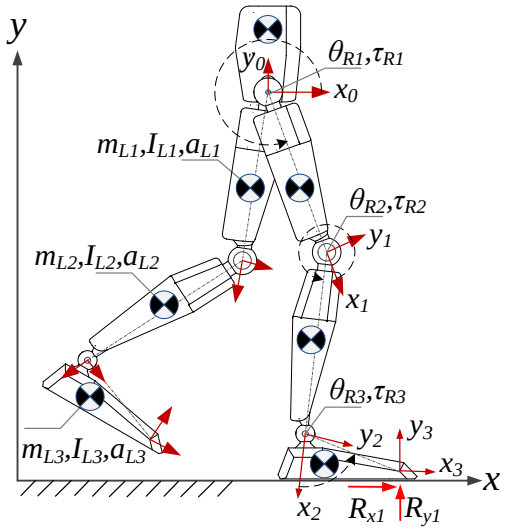

Figure B1. Planar 3-DOF model of human lower limb

Since the joint axes are all parallel to each other, all the twist angles α_i and translational distances d_i are set to be zero. For the coordinate systems chosen, the link parameters are given in The D-H transformation matrices are obtained by substituting the D-H link parameters into:

$$A_{0,1}=\begin{bmatrix} S\theta_1 & C\theta_1 & 0 & a_1S\theta_1 \\ -C\theta_1 & S\theta_1 & 0 & -a_1C\theta_1 \\ 0 & 0 & 1 & 0 \\ 0 & 0 & 0 & 1 \end{bmatrix} \quad A_{1,2}=\begin{bmatrix} C\theta_2 & -S\theta_2 & 0 & a_2C\theta_2 \\ S\theta_2 & C\theta_2 & 0 & a_2S\theta_2 \\ 0 & 0 & 1 & 0 \\ 0 & 0 & 0 & 1 \end{bmatrix} \quad A_{2,3}=\begin{bmatrix} -S\theta_3 & -C\theta_3 & 0 & -a_3S\theta_3 \\ C\theta_3 & -S\theta_3 & 0 & -a_3C\theta_3 \\ 0 & 0 & 1 & 0 \\ 0 & 0 & 0 & 1 \end{bmatrix} \tag{B.1}$$

There are two types of dynamical problems: direct dynamics and inverse dynamics. The direct dynamics problem is to find the response of a manipulator arm corresponding to some applied torques and/or forces. That is, given a vector of joint torques or forces, we wish to compute the resulting motion of the manipulator as a function of time. The inverse dynamics problem is to find the actuator torques and/or forces required to generate a desired trajectory of the manipulator.

Derivation of the Inverse Dynamics

In this work the Lagrange's equations of motion is applied to solve for the dynamical equations of the manipulator. The Lagrangian method, formulates the dynamic equations of motion by using a set of generalized coordinates. The Lagrangian function is defined as the difference between the kinetic and potential energy of a mechanical system.

$$L = K - U \tag{B.2}$$

Lagrange's equations of motion are formulated in terms of the Lagrangian function as [98]:

$$\frac{d}{dt}\left(\frac{\partial L}{\partial \dot{q}_i}\right)-\frac{\partial L}{\partial q_i}=Q_i \tag{B.3}$$

Where Q_i represents the generalized forces acting on the robotic structure. In what follows we will briefly discuss the derivation of each one of the Lagrangian components in detail.

Kinetic Energy

The kinetic energy of a rigid link is equal to the kinetic energy of a point mass of mass m located at the center of mass, plus the kinetic energy of rotation about the center of mass as follows [39]:

$$K_i=\frac{1}{2}V_{ci}^T m_i V_{ci}+\frac{1}{2}I_i\omega_i \tag{B.4}$$

where V_{ci} is the linear velolcity of the center of mass and ω_i is the angular velocity of the moving link. It should also be noted that the velocity vectors and the inertia matrix in Eq. B4 are expressed in the base frame. Let I_i be the inertia matrix of link i about its center of mass and expressed in the base frame, and ${}^{i}I_i$ be the inertia matrix of link i about its center of mass and expressed in the link frame i. Then in order to express the inertia matrix in the base frame we have:

$$I_i=R_{0,i}^{i}I_i\left(R_{0,i}\right)^T \tag{B.5}$$

We note that ${}^{i}I_i$ is time invariant. However, I_i depends on the links posture, because it is expressed in the base frame and the orientation of link i with respect to the base frame is a function of joint variables. Assuming that the moving links are homogenous with a relatively small cross section, the inertia matrix of the links about their respective centres of mass and expressed in the base frame are obtained by using Eq. B5, and for the links involved in the lower limb model is as follows:

$$I_1=\frac{m_1a_1^2}{12}\begin{bmatrix} S^2\theta_1 & -S\theta_1C\theta_1 & 0\\ -S\theta_1c\theta_1 & C^2\theta_1 & 0\\ 0 & 0 & 1\end{bmatrix}$$

$$I_2=\frac{m_2a_2^2}{12}\begin{bmatrix} S^2\theta_{12} & -S\theta_{12}C\theta_{12} & 0\\ -S\theta_{12}C\theta_{12} & C^2\theta_{12} & 0\\ 0 & 0 & 1\end{bmatrix} \tag{B.6}$$

$$I_3=\frac{m_3a_3^2}{12}\begin{bmatrix} S^2\theta_{123} & -S\theta_{123}C\theta_{123} & 0\\ -S\theta_{123}C\theta_{123} & C^2\theta_{123} & 0\\ 0 & 0 & 1\end{bmatrix}$$

The velocity of the center of mass and the angular velocity of link i can be expressed in matrix form as

$$\dot{\mathrm{X}}_{ci} = \mathrm{J}_i \dot{\mathrm{q}} \tag{B.7}$$

where

$$\dot{\mathrm{X}}_{ci} = \begin{bmatrix} V_{ci} \\ \omega_{ci} \end{bmatrix}, \quad \mathrm{J}_i = \begin{bmatrix} J_{vi} \\ J_{\omega i} \end{bmatrix} \tag{B.8}$$

Here J_i is called the link jacobian matrix which is a $6 \times n$ matrix that maps the instantaneous joint rates into the instantaneous velocity of the center of mass and the angular velocity of link i. Let J_{vi}^{j} and $J_{\omega i}^{j}$ be the jth column vectors of J_{vi} and $J_{\omega i}$ respectively. Then applying the theory of instantaneous screw motion for $j \leq i$, for a structure only having revolute joints we obtain:

$$\begin{aligned} J_{vi}^{j} &= Z_{j-1} \times {}^{j-1}\mathbf{P}_{ci}^{*} \\ J_{\omega i}^{j} &= Z_{j-1} \end{aligned} \tag{B.9}$$

where $\mathrm{Z}_{j-1}$is a unit vector along the ith joint axis, and ${}^{j-1}\mathrm{P}_{ci}^{*}$ is a vector defined from the origin of the $(j-1)$th link frame,O_{i-1}, to the origin of the center of mass of link i and expressed in fixed coordinate frame (x_0, y_0, z_0), as shown in Figure B2.

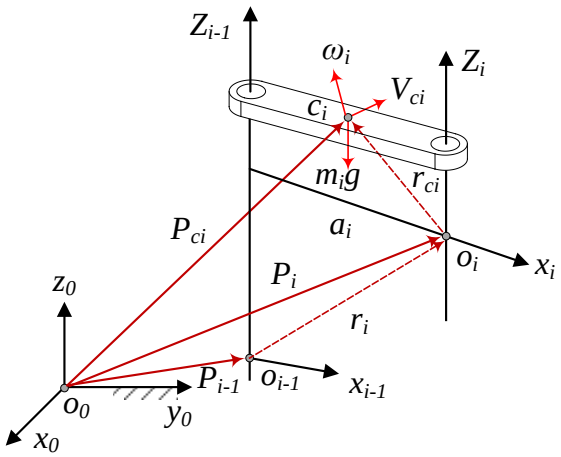

Figure B2. Forces and moments exerted on link *i*.

The direction and location of each joint axis should be determined first. This can be accomplished by the following matrix operations:

$$\begin{aligned} Z_{i-1} &= R_{0,i-1} \begin{bmatrix} 0 \\ 0 \\ 1 \end{bmatrix} \\ {}^{i-1}\mathbf{P}_n^{*} &= R_{0,i-1} r_{i-1,i} + {}^{i}\mathbf{P}_n^{*} \end{aligned} \tag{B.10}$$

where

$$r_{i-1,i} = \begin{bmatrix} a_i C\theta_i \\ a_i S\theta_i \\ d_i \end{bmatrix} \tag{B.11}$$

Denotes the vector $\overline{O_{i-1}O_i}$ expressed in the $(i-1)$th link frame. It is also worth mentioning that J_{vi}^{j} and $J_{\omega i}^{j}$ represent the partial rate of change of the velocity of the center of mass and the angular velocity of link i with respect to the jth joint motion. Since the motion of link i depends only on joints 1 through i, the two column vectors above are set to zero for $j > i$. Using the notations above J_{vi} and $J_{\omega i}$ can be written as

$$\begin{aligned} J_{vi} &= \begin{bmatrix} J_{vi}^{1} & J_{vi}^{2} & \dots & J_{vi}^{i} & 0 & \dots & 0 \end{bmatrix} \\ J_{\omega i} &= \begin{bmatrix} J_{\omega i}^{1} & J_{\omega i}^{2} & \dots & J_{\omega i}^{i} & 0 & \dots & 0 \end{bmatrix} \end{aligned} \tag{B.12}$$

The position vectors of the centers of mass of links with respect to their preceding link frames and expressed in the base frame are summarized in Table B3.

Table B3. Position vectors of the centers of mass with respect to various link frames and expressed in the base frame

Link 1	Link 2	Link 3
$^{0}\mathbf{P}_{c1}^{*} = \begin{bmatrix} \frac{a_1 C\theta_1}{2} \\ \frac{a_1 S\theta_1}{2} \\ 0 \end{bmatrix}$	$^{1}\mathbf{P}_{c2}^{*} = \begin{bmatrix} \frac{a_2 C\theta_{12}}{2} \\ \frac{a_2 S\theta_{12}}{2} \\ 0 \end{bmatrix}$	$^{2}\mathbf{P}_{c3}^{*} = \begin{bmatrix} \frac{a_3 C\theta_{123}}{2} \\ \frac{a_3 S\theta_{123}}{2} \\ 0 \end{bmatrix}$
	$^{0}\mathbf{P}_{c2}^{*} = \begin{bmatrix} a_1 C\theta_1 + \frac{a_2 C\theta_{12}}{2} \\ a_1 S\theta_1 + \frac{a_2 S\theta_{12}}{2} \\ 0 \end{bmatrix}$	$^{1}\mathbf{P}_{c3}^{*} = \begin{bmatrix} a_2 C\theta_{12} + \frac{a_3 C\theta_{123}}{2} \\ a_2 S\theta_{12} + \frac{a_3 S\theta_{123}}{2} \\ 0 \end{bmatrix}$
		$^{0}\mathbf{P}_{c3}^{*} = \begin{bmatrix} a_1 C\theta_1 + a_2 C\theta_{12} + \frac{a_3 C\theta_{123}}{2} \\ a_1 S\theta_1 + a_2 S\theta_{12} + \frac{a_3 S\theta_{123}}{2} \\ 0 \end{bmatrix}$

The link jacobian submatrices, J_v and J_ω are obtained by substituting the expressions defined in Table B3. Into Eq. B12. This would result in:

$$J_{v1} = \begin{bmatrix} -\frac{a_1 S\theta_1}{2} & 0 & 0 \\ a_1 C\theta_1 & 0 & 0 \\ 0 & 0 & 0 \end{bmatrix} \tag{B.13a}$$

$$J_{v2} = \begin{bmatrix} -a_1 S\theta_1 - \frac{a_2 S\theta_{12}}{2} & -\frac{a_2 S\theta_{12}}{2} & 0 \\ a_1 C\theta_1 + \frac{a_2 C\theta_{12}}{2} & -\frac{a_2 C\theta_{12}}{2} & 0 \\ 0 & 0 & 0 \end{bmatrix} \tag{B.13b}$$

$$J_{v3} = \begin{bmatrix} -a_1 S\theta_1 - \frac{a_2 S\theta_{12}}{2} - \frac{a_3 S\theta_{123}}{2} & -\frac{a_2 S\theta_{12}}{2} - \frac{a_3 S\theta_{123}}{2} & -\frac{a_3 S\theta_{123}}{2} \\ a_1 C\theta_1 + \frac{a_2 C\theta_{12}}{2} + \frac{a_3 C\theta_{123}}{2} & -\frac{a_2 C\theta_{12}}{2} - \frac{a_3 C\theta_{123}}{2} & -\frac{a_3 C\theta_{123}}{2} \\ 0 & 0 & 0 \end{bmatrix} \tag{B.13c}$$

and subsequently,

$$J_{\omega 1} = J_{\omega 2} = J_{\omega 3} = \begin{bmatrix} 0 & 0 & 0 \\ 0 & 0 & 0 \\ 1 & 0 & 0 \end{bmatrix} \tag{B.14}$$

For an 3 –link manipulator, the kinetic energy can be derived by summing up all links. Substituting Eq. B7 back into Eq. B4 we have,

$$K = \frac{1}{2}\dot{q}^T \left[\sum_{i=1}^{3} \left(J_{vi}^T m_i J_{vi} + J_{\omega i}^T I_i J_{\omega i} \right) \right] \dot{q} = \frac{1}{2}\dot{q}^T M \dot{q} \tag{B.15}$$

where M is an 3×3 manipulator inertia matrix. For the lower limb body under study, the inertia matrix would be defined as follows,

$$M = \begin{bmatrix} M_{1,1} & M_{1,2} & M_{1,3} \\ M_{2,1} & M_{2,2} & M_{2,3} \\ M_{3,1} & M_{3,2} & M_{3,3} \end{bmatrix} \tag{B.16}$$

and the elements of the inertia matrix are summarized as:

$$M_{1,1} = a_2 a_3 m_3 C\theta_3 + a_1 a_3 m_3 C\theta_{23} + a_2 a_1 \left(m_2 + 2m_3\right) C\theta_2 + \cdots \left(\frac{m_1}{3} + m_3 + m_2\right) a_1^2 + \left(m_3 + \frac{m_2}{3}\right) a_2^2 + \frac{m_3 a_3^2}{3} \quad \text{(B.17a)}$$

$$M_{1,2} = a_2 a_3 m_3 C\theta_3 + \frac{a_1 a_3 m_3 C\theta_{23}}{2} + \left(m_3 + \frac{m_2}{3}\right) C\theta_2 a_2 a_1 + \cdots + \left(m_3 + \frac{m_2}{3}\right) a_2^2 + \frac{m_3 a_3^2}{3} \quad \text{(B.17b)}$$

$$M_{1,3} = \frac{m_3 a_3^2}{3} + \frac{a_2 a_3 m_3 C\theta_3}{2} + \frac{a_1 a_3 m_3 C\theta_{23}}{2} \quad \text{(B.17c)}$$

$$M_{2,1} = a_2 a_3 m_3 C\theta_3 + \frac{a_1 a_3 m_3 C\theta_{23}}{2} + \frac{m_3 a_3^2}{3} + \left(m_3 + \frac{m_2}{3}\right) C\theta_2 a_2 a_1 + \left(m_3 + \frac{m_2}{3}\right) a_2^2 \quad \text{(B.17d)}$$

$$M_{2,2} = a_2 a_3 m_3 C\theta_3 + \left(m_3 + \frac{m_2}{3}\right) a_2^2 \quad \text{(B.17e)}$$

$$M_{2,3} = \frac{a_2 a_3 m_3 C\theta_3}{2} + \frac{m_3 a_3^2}{3} \quad \text{(B.17f)}$$

$$M_{3,1} = \frac{a_2 a_3 m_3 C\theta_3}{2} + \frac{m_3 a_3^2}{3} + \frac{a_1 a_3 m_3 C\theta_{23}}{2} \quad \text{(B.17g)}$$

$$M_{3,2} = \frac{a_2 a_3 m_3 C\theta_3}{2} + \frac{m_3 a_3^2}{3} \quad \text{(B.17h)}$$

$$M_{3,3} = \frac{m_3 a_3^2}{3} \quad \text{(B.17i)}$$

Potential Energy

The potential energy of link i of a manipulator can be expressed as the work required to raise the center of mass of link i from a horizontal reference plane to its current position under the influence of gravity. Hence the total energy stored in a manipulator can be defined as:

$$U = -\sum_{i=1}^{n} m_i g^T p_{ci} \quad \text{(B.18)}$$

Generalized Forces

The generalized forces includes all forces acting on the manipulator. These forces are consistent with the constraints; this accounts for forces and torques exerted on the joints and also external force and moment applied at the end effector and is defined as [39]:

$$Q = \tau + J^T F_e \quad \text{(B.19)}$$

where *J* is the Jacobian matrix of the manipulator.

General Form of Dynamical Equation

By substituting Eq. B18 and Eq. B15 back into Eq. B2, an expression for the Lagrangian function can be derived:

$$L = \frac{1}{2}\dot{q}^T M \dot{q} + \sum_{i=1}^{n} m_i g^T p_{ci} \tag{B.20}$$

where the inertia matrix defined as M is configuration dependent since it consists the link jacobian submatrices J_{vi}^{j} and $J_{\omega i}^{j}$. Next, the Lagrangian function will be differentiated with respect to q_i, $\dot{q}_i$, and t in order to formulate the dynamic equations of motion. This would result in n number of scalar equation as follows:

$$\sum_{i=1}^{n} m_{ij}\ddot{q}_j + V_i + G_i = Q_i \tag{B.21}$$

where

$$V_i = \sum_{j=1}^{n}\sum_{k=1}^{n}\left(\frac{\partial M_{ij}}{\partial q_k} - \frac{1}{2}\frac{\partial M_{jk}}{\partial q_i}\right)\dot{q}_j\dot{q}_k \tag{B.22}$$

and G_i is defined as,

$$G_i = -\sum_{j=1}^{n} m_j g^T J_{vj}^{i} \tag{B.33}$$

The general form of dynamical equation can then be summarized in matrix format as,

$$M\ddot{q} + V + G - J^T F_e = \tau \tag{B.34}$$

The first term in Eq. B34 which is the manipulator inertia matrix M which defines the inertia forces, the second term V, is called the velocity coupling vector and represents the Coriolis and centrifugal forces, and the third term defines the gravitational forces acting on the manipulator. The fourth term represents any external force acting on the end effector. Now by taking the partial derivatives of the manipulator inertia matrix, the velocity coupling vector for the lower limb can be found as:

$$\begin{aligned}
V_1 = \quad & \left(-m_3 a_1 a_2 S\theta_2 - \frac{m_2 a_2 a_1 S\theta_2}{2} - \frac{m_3 a_3 a_1 S\theta_{23}}{2}\right)\dot{\theta}_2^2 + \left(-\frac{m_3 a_2 a_3 S\theta_3}{2} - \frac{m_3 a_3 a_1 S\theta_{23}}{2}\right)\dot{\theta}_3^2 + \cdots \\
& \left(-2m_3 a_1 a_2 S\theta_2 - m_2 a_1 a_2 S\theta_2 - m_3 a_1 a_3 S\theta_{23}\right)\dot{\theta}_1\dot{\theta}_2 + \cdots \\
& \left(-m_3 a_2 a_3 S\theta_3 - m_3 a_1 a_3 S\theta_{23}\right)\dot{\theta}_1\dot{\theta}_2 + \left(-m_3 a_2 a_3 S\theta_3 - m_3 a_1 a_3 S\theta_{23}\right)\dot{\theta}_2\dot{\theta}_3 \\
V_2 = \quad & \left(m_3 a_1 a_2 S\theta_2 + \frac{m_2 a_2 a_1 S\theta_2}{2} - \frac{m_3 a_3 a_1 S\theta_{23}}{2}\right)\dot{\theta}_2^2 - \frac{m_3 a_2 a_3 S\theta_3}{2}\dot{\theta}_3^2 - \cdots \\
& m_3 a_2 a_3 S\theta_3 \dot{\theta}_1\dot{\theta}_2 - m_3 a_2 a_3 S\theta_3 \dot{\theta}_2\dot{\theta}_3 \\
V_3 = \quad & \frac{m_3 a_3 \left(S\theta_{23} + a_2 S\theta_3\right)\dot{\theta}_1^2}{2} + m_3 a_2 a_3 S\theta_3 \dot{\theta}_1\dot{\theta}_2 + \frac{m_3 a_2 a_3 S\theta_3}{2}\dot{\theta}_3^2
\end{aligned} \tag{B.35}$$

The velocity-squared terms are related to the centrifugal forces and the velocity product terms define the Coriolis forces.

The gravitational forces are subsequently obtained by substituting Eq. B13 into Eq. B33,

$$\begin{aligned} G_1 &= \frac{m_1 a_1 g C\theta_1}{2} + \frac{m_2 a_2 g C\theta_{12}}{2} + m_2 a_1 g C\theta_1 + \frac{m_3 a_3 g C\theta_{123}}{2} + m_3 a_2 g C\theta_{12} + m_3 a_1 g C\theta_1 \\ G_2 &= \left(m_3 a_2 g + \frac{m_2 a_2 g}{2} \right) C\theta_{12} + \frac{m_3 a_3 g C\theta_{123}}{2} \\ G_3 &= \frac{m_3 a_3 g C\theta_{123}}{2} \end{aligned} \tag{B.36}$$

and finally, the fourth term in Eq. B34 which corresponds to the generalized forces acting on the foot would result in:

$$J^T F_e = \begin{bmatrix} \left(-a_3 S\theta_{123} - a_2 S\theta_{12} - a_1 S\theta_1\right) F_x + \left(a_3 C\theta_{123} + a_2 C\theta_{12} + a_1 C\theta_1\right) F_y \\ \left(-a_3 S\theta_{123} - a_2 S\theta_{12}\right) F_x + \left(a_3 C\theta_{123} + a_2 C\theta_{12}\right) F_y \\ -a_3 S\theta_{123} F_x + a_3 C\theta_{123} F_y \end{bmatrix} \tag{B.37}$$

It should be noted that for this study, the generalized forces acting on the foot was set to zero in order to simplify the comparison study between the simulated and analytical results

Comparison of Dynamic Analytical and Simulation Results

Figure B3 shows signals corresponding to the hip, knee and ankle joint's orientation during normal gait cycles; these gait signals are provided by Stanford University's OpenSim software [29, 30]. The signals were used for both simulation and analytical study in order to compare the results obtained from these two methods. The software used to complete this task was a synthesis of SolidWorks, Simulink, and SimMechanics second generation.

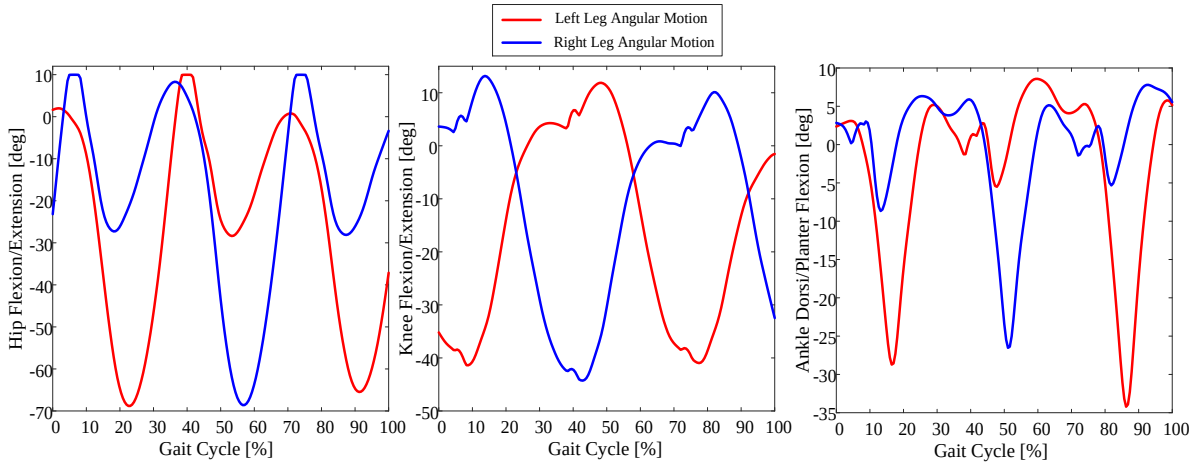

Figure B3. Planar orientation signals during normal gait cycle of human lower limb

Figure B4 shows simulated torque, velocity, and power curves for the 3-RUS/S mechanism actuators during normal gait cycle motions [59]. These plots were obtained by subjecting a Matlab/SimMechanics simulation model of a planar 3-DOF lower limb of a 75 kg human with a predefined mass and moment of inertia to the walking gait cycle

provided by the OpenSim software [60], and monitoring joint torques using virtual sensors.

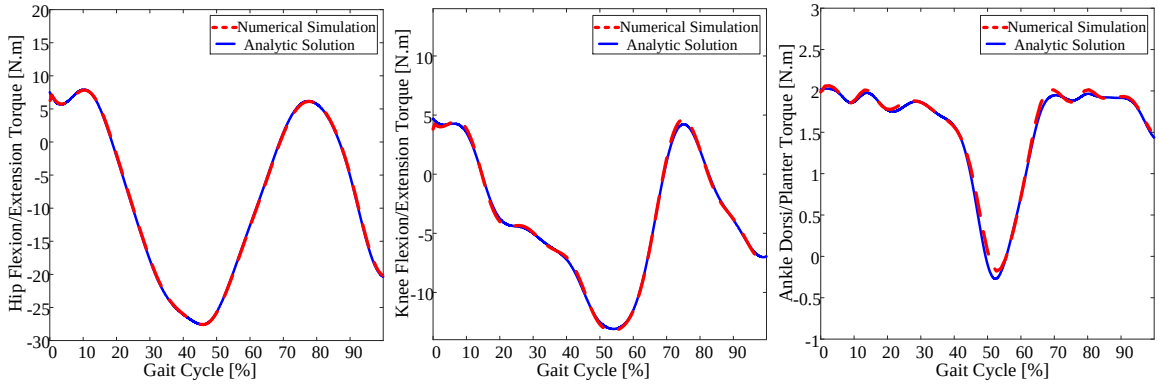

Figure B4. Joint torques of the planar lower limb model

Figure B4 shows overlaid plots of the simulated signal and analytical results for each joint during the normal gait tracking. These plots clearly suggest that the SimMechanics simulation package is able to accurately predict and define the joint torques exerted on the joints of the lower limb model and one can rely on the results obtained from the simulation studies.

Appendix C.

Working and Assembly Modes of the 3-RRR Spherical Manipulator in the 3-SRRP/S and 3-SPRR/S Hybrid Mechanisms

Kinematic Model of the 3-RRR Spherical Parallel Manipulator

For this study, a base reference frame is defined in a way that its x axis is collinear with the axis of the first base joint, its y axis is collinear with the axis of the second base joint and subsequently its z axis is collinear with the axis of the third base joint as shown in Figure C1. As a result, the axes of the base joints expressed in the base reference frame are defined by the following unit vectors [99]:

$$\mathrm{u}_1 = \begin{bmatrix} 1 \\ 0 \\ 0 \end{bmatrix}, \quad \mathrm{u}_2 = \begin{bmatrix} 0 \\ 1 \\ 0 \end{bmatrix}, \quad \mathrm{u}_3 = \begin{bmatrix} 0 \\ 0 \\ 1 \end{bmatrix} \tag{C.1}$$

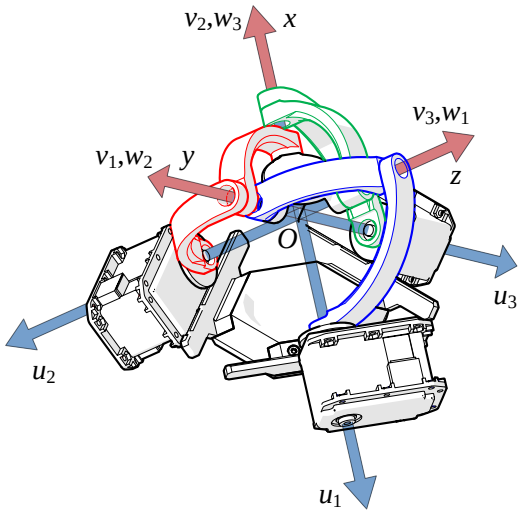

Figure C1. Agile eye in reference orientation

Moreover, expressed in the mobile platform reference frame, the axis of the moving platform joints can be defined by the following unit vectors:

$$\mathrm{v}_1' = \begin{bmatrix} 0 \\ -1 \\ 0 \end{bmatrix}, \quad \mathrm{v}_2' = \begin{bmatrix} 0 \\ 0 \\ -1 \end{bmatrix}, \quad \mathrm{v}_3' = \begin{bmatrix} -1 \\ 0 \\ 0 \end{bmatrix} \tag{C.2}$$

Rotation matrix **R** which defines the orientation of the mobile platform with respect to base frame and an Euler-angle convention is used to express the rotation. The axes of the platform joints in the base frame are as follows,

$$\mathrm{v}_i = \mathbf{R}\mathrm{v}_i^{'} = \mathbf{R}_z(\phi)\mathbf{R}_y(\phi)\mathbf{R}_x(\phi)\mathrm{v}_i^{'}, \tag{C.3}$$

Finally, expressed in the base frame, the axes of the intermediate joints can be evaluated by the following unit vectors:

$$\mathrm{w}_1 = \begin{bmatrix} 0 \\ -S\theta_1 \\ C\theta_1 \end{bmatrix}, \quad \mathrm{w}_1 = \begin{bmatrix} C\theta_2 \\ 0 \\ -S\theta_2 \end{bmatrix}, \quad \mathrm{w}_3 = \begin{bmatrix} -S\theta_3 \\ -C\theta_3 \\ 0 \end{bmatrix} \tag{C.4}$$

Inverse Kinematic and Working Modes

For any given orientation of the moving platform, each leg of the Agile Eye can admit two solutions for θ_i obtained from:

$$\tan\theta_1 = \frac{C\theta S\psi}{C\phi C\psi + S\phi S\theta S\psi}, \tag{C.5}$$

$$\tan\theta_2 = \frac{S\phi S\psi + C\phi S\theta C\psi}{C\theta C\psi}, \tag{C.6}$$

$$\tan\theta_3 = \tan\phi \tag{C.7}$$

Thus the inverse kinematic problem can admit eight real solution or in other words, working modes for any non-singular orientation of the moving platform [63], [99].

Direct Kinematics and Assembly Modes

The Agile Eye has been optimized to possess maximum performance [63], [64]. It has been shown that if such properties are chosen it would result in great simplification in deriving the direct kinematic problem because the eight solutions will reduce to four trivial and non trivial ones. The direct kinematics of the agile Eye is reformulated in the following.

The constraint equations are written [65]:

$$\mathrm{w}_i^T \mathrm{v}_i = 0, \tag{C.8}$$

as a result

$$S\psi(S\theta_1 S\theta S\phi - C\theta C\theta_1) + C\psi S\theta_1 C\phi = 0, \tag{C.9}$$

$$C\psi(C\theta_2 S\theta C\phi - C\theta S\theta_2) + S\psi C\theta_2 S\phi = 0, \tag{C.10}$$

$$S(\theta_3 - \phi)C\theta = 0 \tag{C.11}$$

From Eq. C11, one can conclude that the direct kinematic problem would admit two sets of solutions that is defined by:

$$C\theta = 0 \text{, and} \tag{C.12}$$

$$S(\theta_3 - \phi) = 0 \text{,} \tag{C.13}$$

First Set of Solutions – Trivial Solutions

Eq. C.12 would provide two solutions for the angle θ,

$$\theta = \pi / 2 \text{ and } \theta = -\pi / 2 \tag{C.14}$$

Both of which correspond to a singularity in the Euler angles. From the first solution and after simplification of Eq. C.9, the following condition is found:

$$C(\phi - \psi) = 0 \text{,} \tag{C.15}$$

and from Eq. C.10 after simplification:

$$C(\phi + \psi) = 0 \tag{C.16}$$

In both of these cases, each of the equations would result in two solutions. Thus because of the representation singularity, only four rotation matrices would define the orientations of the mobile platform [99]:

$$\begin{aligned} \mathbf{R}_{TO1} &= \begin{bmatrix} 0 & -1 & 0 \\ 0 & 0 & 1 \\ -1 & 0 & 0 \end{bmatrix}, \qquad \mathbf{R}_{TO2} = \begin{bmatrix} 0 & 1 & 0 \\ 0 & 0 & -1 \\ -1 & 0 & 0 \end{bmatrix}, \\ \mathbf{R}_{TO3} &= \begin{bmatrix} 0 & -1 & 0 \\ 0 & 0 & -1 \\ -1 & 0 & 0 \end{bmatrix}, \qquad \mathbf{R}_{TO4} = \begin{bmatrix} 0 & 1 & 0 \\ 0 & 0 & 1 \\ -1 & 0 & 0 \end{bmatrix}. \end{aligned} \tag{C.17}$$

Figure C2 clearly depicts the four trivial solutions to the direct kinematic problem of the Agile Eye. It can be seen geometrically that if the moving platform of the Agile Eye is positioned at one of these four orientations, all three legs are at a singularity (i.e. fully extended or folded) and can freely rotate about their base joint axes. Figure C2, shows the Agile Eye in these four orientations when assembled on to the SRRP/S and SPRR/S exoskeleton mechanisms. As it may be seen, none of these exoskeletons are mechanically capable to reach to those orientations and cause singularity on the actuating section of the exoskeleton mechanism and these four orientations are outside the allowable workspace of the human hip and the exoskeleton devices.

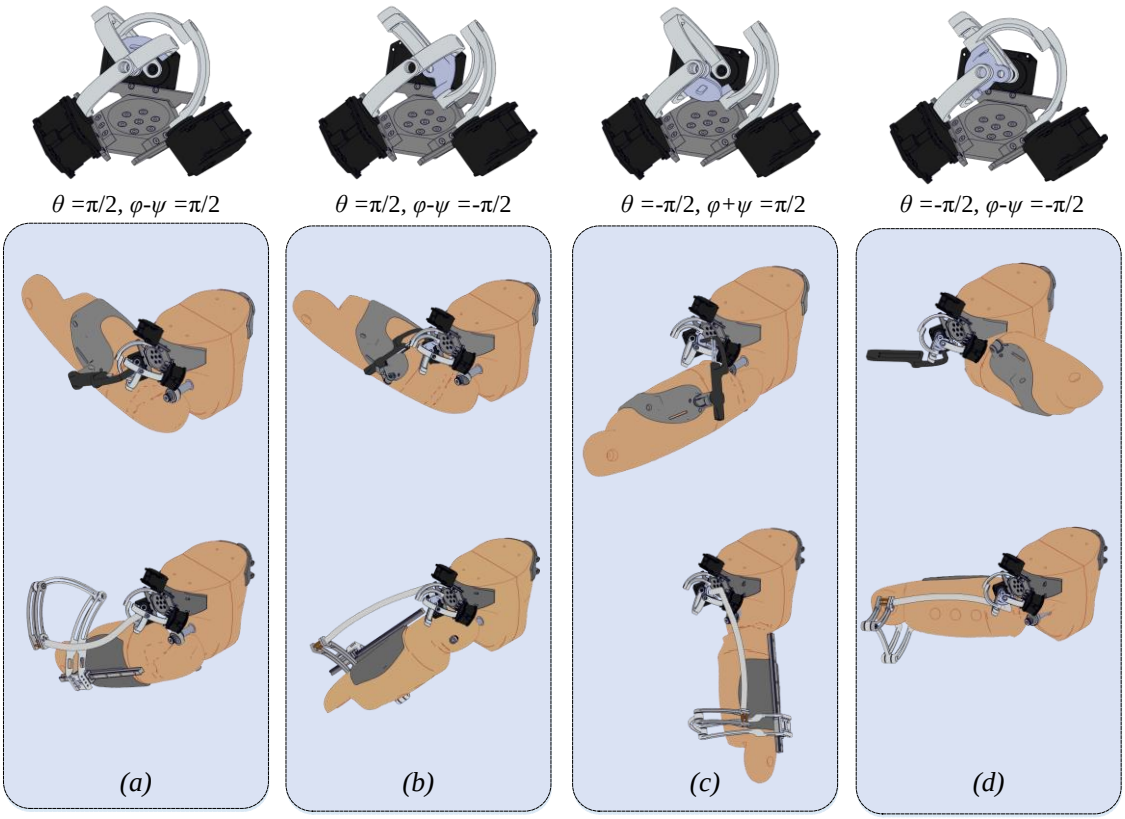

Figure C2. The four trivial solutions to the direct kinematic problem valid for any set of active-joint variables shown with θ_1=0, θ_2=0 and θ_3=0.

Second Set of Solutions – Nontrivial Solutions

Eq. C13 gives two solutions for the angle ϕ:

$$\phi = \theta_3 \text{ and } \phi = \theta_3 \pm \pi \tag{C.18}$$

In the Euler-angle convention, $\{\phi, \theta, \psi\}$ and $\{\phi\pm\pi, \theta\pm\pi, \psi\pm\pi\}$ relate to one orientation. This means that the two solutions lead to the same orientation of the moving platform. Substituting $\phi = \theta_3$ in Eq. C9-11, a new system of equations is generated [99]:

$$p_1 C\psi + p_2 S\psi = 0\,, \tag{C.19}$$

$$p_3 C\psi + p_4 S\psi = 0\,, \tag{C.20}$$

where

$$p_1 = S\theta_1 C\theta_3\,, \tag{C.21}$$

$$p_2 = S\theta_1 S\theta S\theta_3 - C\theta C\theta_1\,, \tag{C.22}$$

$$p_3 = C\theta_2 S\theta C\theta_3 - C\theta S\theta_2\,, \tag{C.23}$$

$$p_4 = C\theta_2 S\theta_3\,. \tag{C.24}$$

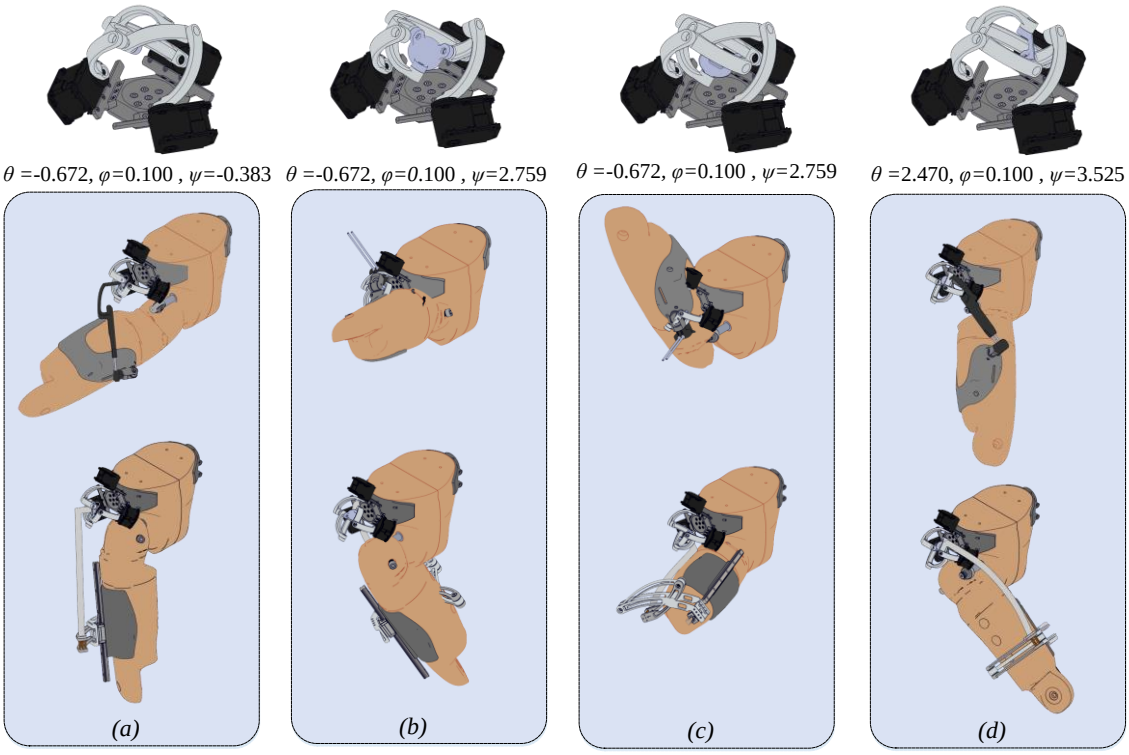

Figure C3. The four nontrivial solutions to the direct kinematic problem of the Agile eye for θ_1=-0.3, θ_2=-0.7 and θ_3=0.1.

The equations above would yield to:

$$p_1 p_4 - p_2 p_3 = 0 \tag{C.25}$$

substituting Eqs. C19-22 into Eq. C.25 would result in:

$$C\theta(q_1 C\theta + q_2 S\theta) = 0\,, \tag{C.26}$$

where

$$q_1 = S\theta_1 C\theta_2 C\theta_3 S\theta_3 - C\theta_1 S\theta_2\,, \tag{C.27}$$

$$q_2 = S\theta_1 S\theta_2 S\theta_3 + C\theta_1 C\theta_2 C\theta_3\,. \tag{C.28}$$

Hence, Eq. C26 would result in:

$$q_1 C\theta + q_2 S\theta = 0\,, \tag{C.29}$$

this gives two solutions as follows:

$$\psi = \tan^{-1}\left(-q_1 / q_2\right) + k\pi \;\text{ for }\; k = 0,1 \tag{C.30}$$

Eqs. C.21-21 is used to find ψ:

$$\psi = \tan^{-1}\left(-p_i / p_{2i}\right) + k\pi \;\text{ for }\; i = 1,2 \tag{C.31}$$

An example of four nontrivial solutions to the direct kinematic problem of the Agile eye is given in Figure C3.

Degenerate Cases

Another set of solutions is obtainable when Eq. C29 is degenerated and q_1=q_2=0. This state only happens if and only if one of the following conditions is true [99]:

$$S\theta_2 = 0 \text{ and } C\theta_3 = 0 \text{, or} \tag{C.32}$$

$$S\theta_3 = 0 \text{ and } C\theta_1 = 0 \text{, or} \tag{C.33}$$

$$S\theta_1 = 0 \text{ and } C\theta_2 = 0 \tag{C.34}$$

In this specific case, θ can gain any value, which is a result of one of the self-motions of the moving platform. If q_2=0 but $q_1 \neq 0$, then Eq. C29 becomes identical with Eq. C12, which states $\theta = \pm\pi/2$. Substituting these values back into Eqs. C19-20:

$$S\theta_1 C(\phi \pm \psi) = 0 \text{ and } C\theta_2 C(\phi \pm \psi) = 0 \tag{C.35}$$

($\phi \pm \psi$) can have any arbitrary value, If $\sin\theta_1$ and $\cos\theta_1$ are set to zero, meaning that the moving platform would have a self-motion. Thus, in summary, the agile Eye will have only the four trivial solutions to its direct kinematic problem if and only if

$$q_2 = S\theta_1 S\theta_2 S\theta_3 + C\theta_1 C\theta_2 C\theta_3 = 0 \text{ ,} \tag{C.36}$$

but neither of Eqs. C32-34 is true.

It can be concluded that Eqs. C32-34 corresponds to six self motions that can be represented by the following rotation matrices [99]:

$$\mathbf{R}_{SM1a} = \begin{bmatrix} 0 & -1 & 0 \\ C\theta & 0 & S\theta \\ -S\theta & 0 & C\theta \end{bmatrix}, \qquad \mathbf{R}_{SM1b} = \begin{bmatrix} 0 & 1 & 0 \\ C\theta & 0 & -S\theta \\ -S\theta & 0 & -C\theta \end{bmatrix}, \tag{C.37}$$

$$\mathbf{R}_{SM2a} = \begin{bmatrix} C\theta & S\theta & 0 \\ 0 & 0 & -1 \\ -S\theta & C\theta & 0 \end{bmatrix}, \qquad \mathbf{R}_{SM2b} = \begin{bmatrix} C\theta & -S\theta & 0 \\ 0 & 0 & 1 \\ -S\theta & -C\theta & 0 \end{bmatrix} \tag{C.38}$$

$$\mathbf{R}_{SM3a} = \begin{bmatrix} 0 & -S(\phi-\psi) & C(\phi-\psi) \\ 0 & C(\phi-\psi) & S(\phi-\psi) \\ -1 & 0 & 0 \end{bmatrix} \quad \mathbf{R}_{SM3b} = \begin{bmatrix} 0 & -S(\phi+\psi) & C(\phi+\psi) \\ 0 & C(\phi+\psi) & S(\phi+\psi) \\ -1 & 0 & 0 \end{bmatrix} \tag{C.39}$$

Each of the pairs of conditions forces a constraint on two of the active joint variables, while the third one is free to obtain any value, without influencing the orientation of the mobile platform. This in other words means, that in the above self-motions there is a leg in singularity. The above self-motions are divided into pairs, where in each pair, one of the motions correspond to a fully extended leg (i.e. b index), while the other to a fully folded one (i.e. a index). Figure C4 shows the two self-motions (SM3a and SM3b) in which leg 3 is in singular configuration. This corresponds to the pair of conditions of Eq. C34 [99]. Figure C4, shows the assembled Agile Eye in this self motion state, assembled

on to the SRRP/S and SPRR/S exoskeleton mechanisms. As it may be seen, none of these exoskeletons are mechanically capable to reach to these two orientations to cause singularity on leg 3 or any of the other two legs. And these orientations are all outside the allowable workspace of the human hip and the exoskeleton devices.

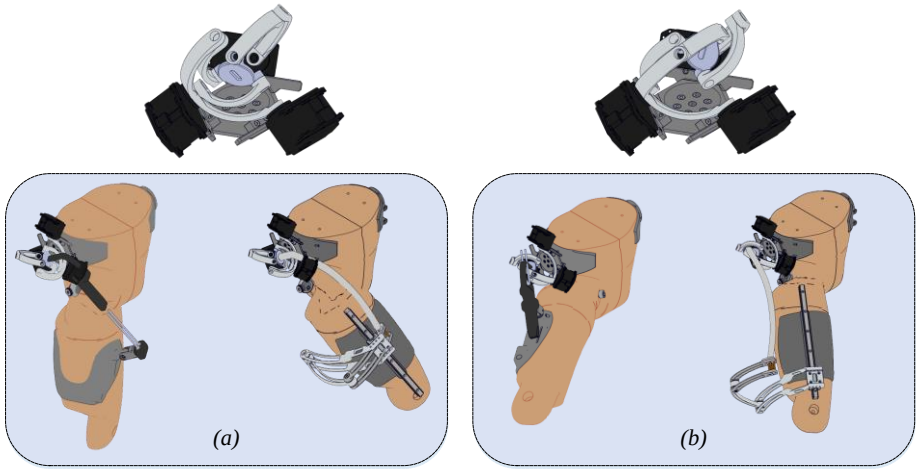

Figure C4. The two self-motions of the mobile platform where leg 3 is singular

Singularity Analysis

The relation between the active-joint rates and the angular velocity of the moving platform can be written as:

$$\mathbf{A}\omega + \mathbf{B}\dot{\theta} = 0\,, \tag{C.40}$$

where $\mathbf{A}$ and $\mathbf{B}$, are Jacobian matrices that are defined as [100]:

$$\mathbf{A} = \begin{bmatrix} (\mathbf{w_1} \times \mathbf{v_1})^T \\ (\mathbf{w_2} \times \mathbf{v_2})^T \\ (\mathbf{w_3} \times \mathbf{v_3})^T \end{bmatrix} \tag{C.41}$$

$$\mathbf{B} = \begin{bmatrix} (\mathbf{w_1} \times \mathbf{v_1})^T \mathbf{u}_1 & 0 & 0 \\ 0 & (\mathbf{w_2} \times \mathbf{v_2})^T \mathbf{u}_1 & 0 \\ 0 & 0 & (\mathbf{w_3} \times \mathbf{v_3})^T \mathbf{u}_3 \end{bmatrix} \tag{C.42}$$

Type 2 singularities can be analyzed by studying matrix $\mathbf{A}$ and can only happen when the three vectors of the matrix are either coplanar or collinear. For the Agile Eye, this would never happen since the vectors can never be collinear therefore, when these vectors are coplanar, the platform can rotate about the axis passing the center O and normal to the plane of vectors. By substituting the nontrivial solution of the Agile Eye into the determinant of $\mathbf{A}$, the expression for the type 2 singularities is obtained:

$$\det(\mathbf{A}) = S\theta_1 S\theta_2 S\theta_3 + C\theta_1 C\theta_2 C\theta_3 = 0\,, \tag{C.43}$$

On the other hand, type 1 singularities are attainable by studying matrix **B** an can happen when a leg is either fully extended or folded. In the Agile Eye when a leg is in singular state, the axes of the base and moving platform joints coincide and the mobile platform would obtain a single degree freedom, moreover; the leg can freely rotate without affecting the orientation of the mobile platform. As a result, type 1 singularities of the Agile Eye are only six curves in orientation space [99]. Substituting the nontrivial solution for the direct kinematics of the Agile Eye into matrix **B** and simplifying results to the following expressions corresponding to type 1 singularities occurring in leg 1, 2 and 3 respectively [99]:

$$B_{11} = \pm \frac{S\theta_1 S\theta_2 S\theta_3 + C\theta_1 C\theta_2 C\theta_3}{\sqrt{1 - C^2\theta_2 S^2\theta_1}\sqrt{1 - C^2\theta_1 S^2\theta_2}} = 0\,, \tag{C.44}$$

$$B_{22} = \pm \frac{S\theta_1 S\theta_2 S\theta_3 + C\theta_1 C\theta_2 C\theta_3}{\sqrt{1 - C^2\theta_2 S^2\theta_3}\sqrt{1 - C^2\theta_1 S^2\theta_2}} = 0\,, \tag{C.45}$$

$$B_{33} = \pm \frac{S\theta_1 S\theta_2 S\theta_3 + C\theta_1 C\theta_2 C\theta_3}{\sqrt{1 - C^2\theta_2 S^2\theta_3}\sqrt{1 - C^2\theta_3 S^2\theta_1}} = 0\,, \tag{C.46}$$

sbstituting the trivial solution for the direct kinematics into B yields:

$$B_{11} = B_{22} = B_{33} = 0 \tag{C.47}$$

Studying the four orientations shown in Figure C2 shows that the legs can be oriented in a way that the vectors normal to the last two joint axes in each leg would not be coplanar. This configuration is called lockup, since the moving platform is constrained even if the actuators are to be removed. Lastly, the denominators of the expressions in Eqs. C44-46 is zeroed when from the reference configuration, a leg is turned at 90 degrees and another leg is turned at 180 degrees. It can be seen that at such a configuration a type 1 singularity occurs yet none of these situations can occur within the physical workspace of the exoskeletons under study.